GEANT4 SIMULATION AND EVALUATION OF A TIME-OF-FLIGHT SPECTROMETER FOR NUCLEAR CROSS SECTION MEASUREMENTS IN PARTICLE THERAPY

Von der Fakultät für Mathematik, Informatik und Naturwissenschaften der RWTH Aachen University zur Erlangung des akademischen Grades einer Doktorin der Naturwissenschaften genehmigte Dissertation vorgelegt von

Dipl.-Ing. (FH), M.Sc.

Oxana Grünwald

aus Fabritschny (Kasachstan)

Berichter:
Univ.-Prof. Dr. Achim Stahl
Univ.-Prof. Dr. med. Michael J. Eble

Tag der mündlichen Prüfung: 08.06.2011

Abstract

In 2007 a new project has been launched in a cooperation between the RWTH Aachen Physics Department, the University Hospital Aachen and the Philips Research Laboratories. The project aim is to validate and improve GEANT4 nuclear interaction models for use in proton and ion therapy.

The method chosen here is the measurement of nuclear reaction cross sections which will not only provide a comparison to the simulation but will also allow to improve some of the parameters in the nuclear models. In the first phase of the project 200 MeV protons are used as a projectile in combination with a thin graphite target. For use in particle therapy the excitation functions of the most frequently produced isotopes need to be measured with an accuracy of 10% or less. For this purpose a dedicated detector system has been designed and implemented in GEANT4.

The detection of target fragments produced by protons in graphite is achieved via time-of-flight spectrometry. In the setup presented here the primary beam first hits the Start detector and initiates the time-of-flight measurement before it passes through the apertures of two Veto detectors and impinges on the target. Successively, the secondary particles emanating from the target travel a short distance of 70 / 80 cm through vacuum (0.1 mbar) before they hit one of the 20 Stop detectors which end the time-of-flight measurement and record the energy deposited by the particle.

The dissertation at hand describes the underlying detector concept and presents a detailed GEANT4 simulation of the setup which allows to evaluate the detector performance with respect to target fragment identification at a projectile energy of 200 MeV. At first, correlations of time-of-flight and energy deposition are built from simulated data and are subsequently used to reconstruct mass spectra of the detected fragments. Such influences on the detection performance as the target thickness, the residual pressure within the detector chamber, the Veto system, and the range of the fragments within the scintillator material are investigated. The results are presented along with indications for improvement, whenever possible.

The simulation results show that the target fragments reach the Stop scintillators and are available for detection. Provided a vacuum of 0.1 mbar and a target thickness of no more than a few micrometers relatively accurate mass spectra can be reconstructed. However, the energy resolution of the setup is strongly compromised by the small range of the fragments within the scintillator material. Along with saturation effects of common plastic scintillators an adequate reconstruction of measured data cannot be achieved.

Currently, alternative hardware and experimental setups are under investigation. For one, pure Caesium Iodide (CsI) is being tested under laboratory conditions for its scintillating properties with a special focus on quenching effects. In addition, development has started for a new spectrometer setup which will make use of inverse kinematics and, rather than aiming to identify target fragments, will detect projectile fragments, e.g. from reactions induced by a carbon beam in a hydrogen target.

Zusammenfassung

Im Jahr 2007 wurde am 3. physikalischen Institut der RWTH Aachen in Kooperation mit der Uniklinik Aachen und den Philips Forschungslaboratorien ein neues Forschungsprojekt gestartet. Das Ziel des Projektes ist die Validierung und Verbesserung der im Monte Carlo Toolkit GEANT4 implementierten Kernmodelle für den Einsatz im Bereich der Protonen- und Ionentherapie.

Um die Genauigkeit der Simulation von Kernwechselwirkungen im Detail zu untersuchen, werden Wirkungsquerschnitte experimentell bestimmt. Die Messdaten dienen dann nicht nur der Validierung, sondern können auch als Grundlage für eine genauere Abschätzung der intrinsischen Parameter hinzugezogen werden. In der ersten Projektphase werden 200 MeV Protonen als Projektil benutzt, in Kombination mit einem dünnen Graphittarget. Um die Anforderungen im Bereich der Teilchentherapie zu erfüllen, müssen die Anregungsfunktionen der am häufigsten erzeugten Isotope mit einer Genauigkeit von 10% oder besser gemessen werden. Zu diesem Zweck wurde ein eigener Detektor entwickelt und in GEANT4 implementiert.

Mit Hilfe eines Flugzeitspektrometers sollen Targetfragmente, welche von Protonen in Graphit erzeugt werden, identifiziert werden. Im hier vorgestellten Aufbau trifft das primäre Proton zunächst auf den Start Detektor und löst die Flugzeitmessung aus, bevor es die Aperturen der beiden Veto Detektoren passiert und auf das Target trifft. Die im Target erzeugten Sekundärteilchen legen eine kurze Flugstrecke von 70 / 80 cm im Vakuum (0.1 mbar) zurück, bevor sie auf einen der 20 Stopp Szintillatoren treffen. Diese beenden die Flugzeitmessung und registrieren zusätzlich die Energie, welche das Teilchen im Szintillatormaterial deponiert.

Die vorliegende Dissertation beschreibt im einzelnen das Detektorkonzept und stellt die entsprechende GEANT4 Simulation vor, welche eine Evaluierung der Detektorperformance in Bezug auf die Identifikation der Targetfragmente bei einer Projektilenergie von 200 MeV erlaubt. Zunächst werden Korrelationen der Flugzeit und der Energiedeposition aus den Simulationsdaten gebildet, um anschliessend Massenverteilungen der Fragmente zu rekonstruieren. Die Auswirkungen solcher Größen auf die Performance des Detektors wie die Targetdicke, der Restdruck in der Detektorkammer, das Veto System und die Reichweite der Fragmente innerhalb des Szintillatormaterials werden untersucht. Die Ergebnisse werden vorgestellt und, wo es möglich ist, werden Richtwerte für eine optimale Datenaufnahme genannt.

Die Ergebnisse der Simulation zeigen, dass die Targetfragmente die Stopp Szintillatoren erreichen und dort detektiert werden können. Vorausgesetzt, dass der Restdruck in der Detektorkammer 0.1 mbar oder weniger beträgt und das Target nicht dicker als

einige Mikrometer ist, kann eine vergleichsweise genaue Rekonstruktion der Massenspektren erreicht werden. Allerdings wird die Energieauflösung des Experiments sehr stark durch die geringe Reichweite der Targetfragmente innerhalb des Plastikszintillators verschlechtert. Unter Berücksichtigung der Sättigungseffekte, die schwerere Teilchen im Szintillatormaterial hervorrufen, kann eine adequate Rekonstruktion der Messdaten nicht erreicht werden.

Zurzeit werden einige alternative Konzepte zum experimentellen Aufbau näher untersucht. Zum einen wird reines Cäsiumjodid (CsI) als mögliches Szintillatormaterial unter Laborbedingungen getestet, mit besonderem Augenmerk auf Quenching. Zusätzlich entsteht gerade ein neues Spektrometer-Konzept, welches die inverse Kinematik ausnutzen wird und, statt Target-Fragmente nachzuweisen, Projektil-Fragmente detektieren wird, z.B. aus Reaktionen eines Kohlenstoff-Strahls mit einem Wasserstoff-Target.

Contents

1. Introduction

After cardiovascular diseases, cancer is the second prevalent cause of death in Germany. According to Cancer Research UK [Can]

> *there are 24.6 million people alive who have received a diagnosis of cancer in the last five years. Around half of these people live in Europe and North America.*

After radiotherapy had started out in the 1960 as a field mainly based on empiricism and associated with severe side effects it is now, after surgery, the most successfully and most frequently used treatment modality for cancer and is applied in more than 50% of all cancer patients [SBG06]. This development was mainly due to innovations in the fields of physics, mathematics, computer science and radiation biology as well as electrical and mechanical engineering making radiotherapy one of the most interdisciplinary fields in clinical practice.

The primary aim of radiotherapy is the delivery of a lethal dose to the tumor cells. In combination with the additional task of sparing healthy tissue from radiation damage, radiotherapy becomes a technical challenge. Tumors often grow close to radiosensitive organs such as the eyes, the optic nerves, the brain stem, spinal cord, bowels or lung tissue. Also, some tumors are radioresistant so that a very high dose must be delivered in order to reach a therapeutic effect [SBG06].

Especially in such difficult cases the new modalities of proton and ion therapy offer great advantages over conventional radiotherapy. The characteristic physical dose distribution of these charged particles allows for a higher conformity of the beam to the target volume. In addition, with ions like ^{12}C, less physical dose needs to be delivered compared to gamma irradiation in order to reach the desired therapeutic effect.

As a consequence of these and other benefits [1], particle therapy became a matter of intensive research over the last 20 years and many new proton and ion therapy centres have been built and started operation all over the world. Most of these centres are located in the USA and Japan (seven each). In Germany proton therapy is provided by the HMI in Berlin and the RPTC in Munich. The newly built HIT in Heidelberg will provide therapy with protons and carbon ions. The horizontal proton and ^{12}C-ion beam lines have started operation in 2009 followed by the unique ^{12}C-ion gantry in 2010. The horizontal beam lines as well as the carbon ion gantry employ the beam scanning technique as opposed to passive scattering techniques. New centres for proton

[1] All advantages are described in detail in section 2.1.

therapy are planned in Cologne and Essen. Protons and carbon ions will be employed in facilities planned in Marburg and Kiel.

Currently, there are plans and ongoing negotiations for a particle therapy centre to be built in the industrial zone Avantis located between Aachen and Maastricht. In connection with this a new research project has been launched in 2007 in a cooperation between the RWTH Aachen Physics Department, the University Hospital Aachen and the Philips Research Laboratories. The primary aim of this project is to validate the GEANT4 Monte Carlo toolkit for proton and ion therapy and make it fit for the multitude of predictive tasks in particle therapy which are increasingly fulfilled by Monte Carlo methods.

GEANT4 is an object oriented library for the simulation of particle transport through matter which can be an accelerator, a patient, a phantom, a detector, or a combination of these. The main advantages of using the GEANT4 toolkit are its capability to simulate very complex geometries and the fact that it allows the user to compile an optimal set of physics for the application at hand by choosing from a wide variety of possibilities. The primary goal of the collaboration is not only to identify the optimal set of models but also to provide a new accurate set of measured data which will help to improve the accuracy of the simulation.

The main focus of the validation is on the nuclear interaction models. Here, previous validation studies have shown some incapabilities which not only apply to GEANT4 but also to all other codes emphasising the overall need for new measurements. For this purpose a dedicated time-of-flight spectrometer has been designed, built and also implemented in GEANT4. The design is aimed at accurate cross section measurements in the low energy range typical for particle therapy. The measurements are expected to provide GEANT4 with the high predictive power which is needed for precise dose calculations and high accuracy predictions for in vivo quality control imaging.

In the time-of-flight spectrometer, the reaction channels will be identified via the detection of heavier target fragments. Since other methods found in literature are based on the detection of one or more light fragments this experiment is a novel approach. Hence, the detector needs to be simulated in order to evaluate the feasibility of the measurements. Through the use of thin targets the count rate of the detector is relatively low and the allotted beam time at the synchrotron must be used efficiently. Therefore it is crucial to the experiment that the detector performance is evaluated via Monte Carlo simulation and that limitations of the setup are identified and possible improvement solutions are tested and compared. This task is the central part of this thesis.

First, a theoretical basis of the nuclear physics processes and models relevant to the simulation is presented in chapter 2. Chapter 3 provides an overview of the previous approaches to validate the GEANT4 nuclear models found in literature. The GEANT4 simulation of the time-of-flight spectrometer is presented in chapter 4. Here, the implementation of the nuclear reaction process is described in more detail with reference to the models presented in chapter 2.

The results of the detector simulation form the central part of this dissertation and are presented in chapter 5. A dedicated readout software for the experimental data acquisition is introduced in chapter 6 and first experimental tests in the lab and at the COoler SYnchrotron (COSY) in Jülich are shown, as well.

2. Theoretical background

This chapter covers several important aspects of the physics background relevant to this work as a whole and to some parts of it in particular. In section 2.1 particle therapy is introduced as an alternative to conventional therapy with photons and electrons. The main benefits of proton and ion modalities are listed, as well.

A rather detailed account on the physical processes which occur during nuclear reactions is given in section 2.3. The theoretical models of the nucleus are described in section 2.4 and will be relevant to the implementation of physics simulation introduced further in chapter 4.

Section 2.5 introduces the main principles of Monte Carlo simulation. It provides a detailed description of the GEANT4 toolkit followed by an overview of other transport codes employed in particle therapy.

2.1. Advantages of particle therapy

Physical dose

The main benefit of irradiation with high linear energy transfer modalities, like protons and light and heavy ions lies in their physical dose distribution. These particles loose energy through atomic or nuclear interactions. With decreased energy the ionisation process rapidly becomes more pronounced before the maximal energy transfer occurs at the end of the range forming the characteristic Bragg peak. As the range can be adapted through the initial kinetic energy of the beam, the Bragg peak falls inside the tumor. Compared to the conventional gamma modality protons and ions deliver considerably less dose to healthy tissue as is shown by a simple Monte Carlo simulation with a water phantom.

Here, the patient is approximated by a box-shaped water phantom which is placed into the geometry of the simulation. A smaller but equally box-shaped and water filled target volume is placed concentrically inside the water phantom and shall represent the tumor. Subsequently, the target box is irradiated with 15 MeV gamma photons and protons.

The proton Spread Out Bragg Peak (SOBP) was generated by a simple algorithm. The target volume was divided into several thin slices each with its corresponding range and kinetic energy calculated from the NIST PSTAR database. The simulation started by irradiating the slice with the highest range then iteratively administering protons to slices of decreasing range until their energy deposition approximately equaled the energy deposited in the slice with the highest range. [1]

[1] This algorithm serves illustratory purposes only and the slight overdose in the last slice of the proton SOBP in figure 2.1 shall not be discussed in the scope of this introduction.

The depth dose curves of the two modalities are compared in figure 2.1. Figure 2.2 shows the projection of the dose onto the yz-plane of the phantom. Here, protons show a much better conformity of the dose delivery to the target volume.

In particular, such cases are suited for proton and ion modalities where the tumor is located close to serially organised tissues like the spinal cord (i.e. the loss of a part of this organ has a severe functional impact) or where irregular shaped lesions lie close to radio-sensitive organs. In these circumstances the dose needs to be administered with an accuracy of 1-2 mm or less.

Since the dose is more localised and the integral dose to healthy organs is reduced with protons and ions, the risk of secondary cancer and the severity of side effects of the treatment can be lowered considerably. Patient tolerance is increased.

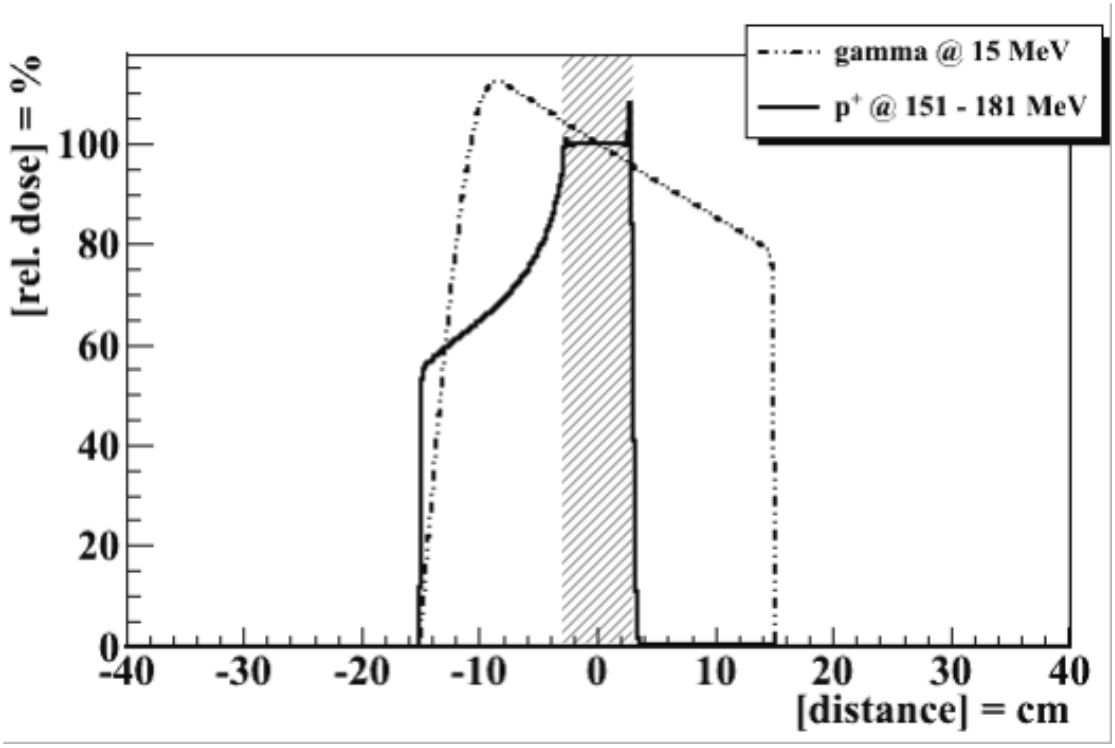

Figure 2.1.: Depth dose curve of 15 MeV γ-radiation vs. protons inside the water phantom. The curves have been normalised to have the same relative dose at the centre of the target region. The latter is represented by the shaded band around the centre of the horizontal axis.

Relative biological effectiveness

With densely ionising radiation, in particular ions like ^{12}C, less dose is usually needed in order to achieve the desired therapeutic effect [WDW06]. This is due to the increased Radio Biological Effectiveness (RBE) which is defined as the ratio of the dose under study relative to a reference dose (usually 250 kV x-ray or ^{60}Co) which causes the same biological effect called isoeffect.

$$RBE = (\frac{D_{ref}}{D_{test}})_{isoeffect} \tag{2.1}$$

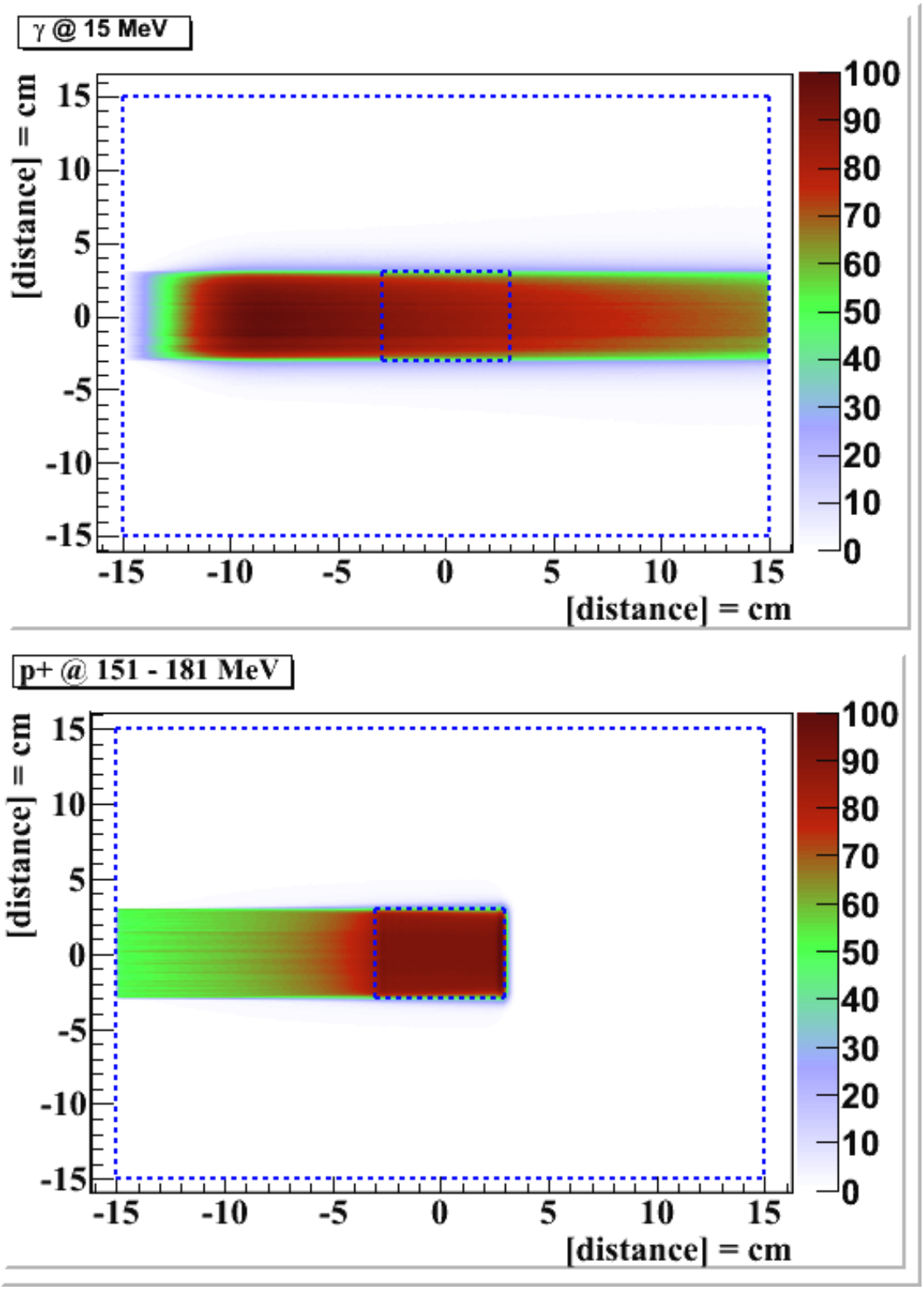

Figure 2.2.: Dose distribution inside the water phantom. The beam direction is from left to right and the dose deposition has been integrated along the axis normal to the image. Both spectra have been normalised to their respective maximum values. The water phantom and the target region are depicted by dashed lines.

In vivo quality control

Since protons and ions also interact with nuclei along their path they provide secondary radiation which escapes the body of the patient and can be registered by an imaging system thus providing a useful source for in vivo treatment verification. A matter of particular interest and subject of undergoing research is the verification of ion range with help of Positron Emission Tomography (PET). Other modalities like prompt gamma imaging which uses the deexcitation photons emitted by excited nuclei during nuclear reactions are under investigation [FBH08], [DBMT09], [KPT08] .

The spectra of secondary photons can also be observed in the simple water phantom simulation mentioned above. Placing a planar 60 x 60 cm air filled dummy detector 30 cm above the phantom provides a means to record the energy of the photons when they reach the detector surface. The energy spectrum of gamma radiation produced in the water phantom during the irradiation with protons and photons is shown in figure 2.3. Here, the 511 keV peak and some characteristic nuclear deexcitation peaks can be seen for protons. The 511 keV peak from gamma irradiation can be attributed to pair production $\gamma \rightarrow e^- + e^+$.

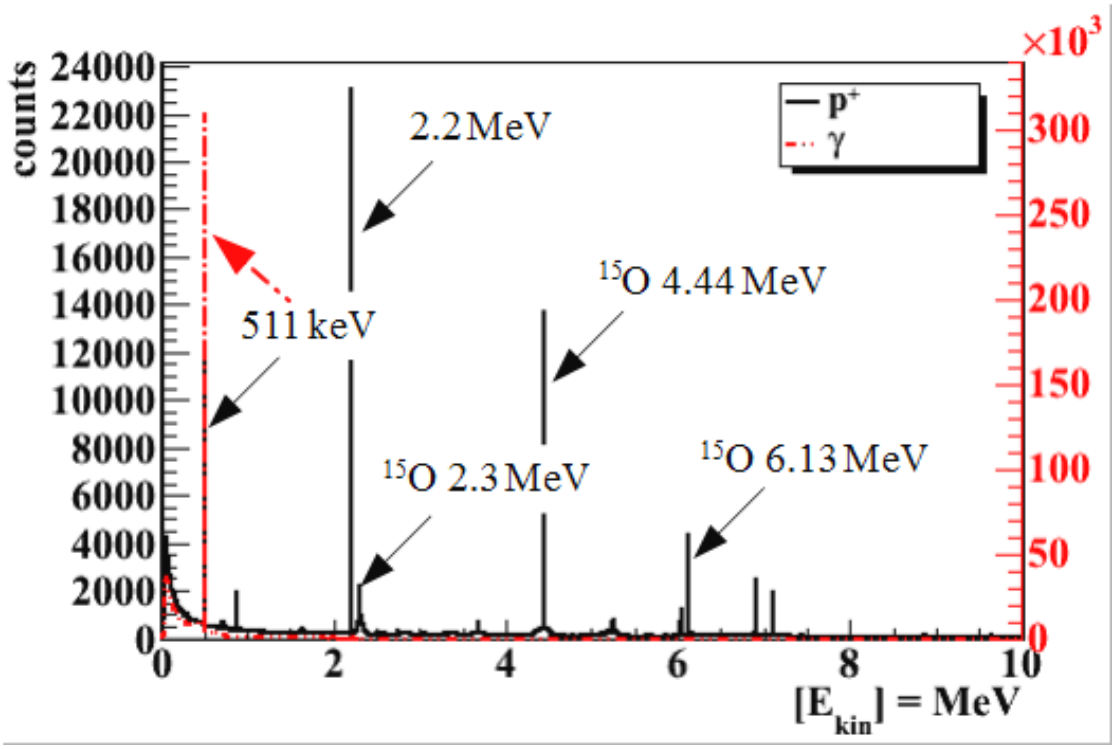

Figure 2.3.: Energy spectrum of γ photons hitting the flat surface detector positioned 30 cm above the water phantom. Most of the peaks above 511 keV stem from the oxygen bound in water. Proton induced peaks depicted by arrows are in agreement with measured spectra from reference [Kac07]. Note, the spectra are not normalised with respect to dose deposition. The peak at 2.2 MeV does not appear in measured data in [Kac07] and is in fact a superposition of many closely spaced contributions from different excited nuclei.

Hypoxic tumours

The irradiation of hypoxic tumours has proven more effective with densely ionising radiation. It means that the partial loss of therapeutic effect which occurs in absence of oxygen with conventional x-ray or gamma modalities is much less pronounced with protons and ions.

2.2. Nuclear reactions in ion therapy

Nuclear reactions play several important roles in ion therapy:

- Nuclear reactions contribute a considerable amount to the total energy deposition in the entry or buildup region of the Bragg curve (see appendix A).
- Elastic and inelastic nuclear interactions are responsible for the loss of primary particles as the the beam penetrates matter. As much as 20% of all primary particles may undergo nuclear reactions along their range.
- Projectile fragmentation of heavier ions like the ^{12}C leads to the occurrence of a dose tail posterior to the Bragg peak.
- These processes represent the sole source of secondary radiation which can leave the body of the patient (or phantom). This type of radiation can be used for in vivo quality assurance because an explicit relationship exists between the secondary radiation distribution and the dose deposition and range of the primary beam.

2.3. Types of nuclear interactions

Nuclei interact via the strong force when their distance to each other decreases below a few fm. They can also interact in Coulomb processes which occur at much greater distances compared to the nuclear potential. Coulomb and strong interactions superpose in experiments and can only be separated from each other in special cases. In quantum mechanics a comprehensive treatment of all processes is achieved by superposing the scattering amplitude for the individual processes. When determining cross sections, coupling effects between some of the processes have to be taken into account by squaring the sum of scattering amplitudes. Most of the physics described in this section can be studied in detail in [MK79] and [BWW08].

Cross sections

A cross section is a probability measure for a (nuclear) interaction to occur between two given particles. In order to gain statistically significant results, usually a current of particles j ($[j] = s^{-1}$) is directed at a target with a certain number of particles per surface area n ($[n] = m^{-2}$). This fixed target setup is more commonly found in low energy nuclear physics as a contrast to collider experiments conducted at high energies.

The total cross section is defined via

$$\sigma = \frac{N}{nj} \qquad with\ [\sigma] = 1\ barn = 10^{-24}\ cm \tag{2.2}$$

where N ($[N] = s^{-1}$) is the production rate. The unit of 1 barn approximately equals the surface area of a nucleus and stems from the definition of the geometrical cross section. Here, the target nuclei are modelled by hard spheres with their hit probability given by their surface area. When two macroscopic spheres collide it is apparent that their collision probability is given by $\pi(R_1 + R_2)^2$, R_1 and R_2 being the radii of the two spheres.

In quantum theory, the particles can be described by a wave function. The dimension of the impinging particle relative to the target nucleus mainly depends on its momentum which defines the associated de Broglie wave length:

$$\lambda\!\!\!^{-} = \frac{\hbar}{p} \tag{2.3}$$

with the cross section now given by $\pi(\lambda\!\!\!^{-} + R_t)^2$ where R_t is the radius of the target. Thus, when $\lambda\!\!\!^{-} \gg R_t$ the cross section approaches $\pi\lambda\!\!\!^{-2}$ and, accordingly, the cross section becomes πR_t^2 in case $\lambda\!\!\!^{-} \ll R_t$. When the de Broglie wave length of the projectile becomes much smaller than the size of a nucleon, i.e. at higher energies, the particle can "see" the nucleons in the target. Here, processes between individual nucleons become possible and the reactions mostly take place via direct mechanisms described further in this section.

The total cross section also includes Coulomb interactions and is therefore higher than its geometrical part. In most cases the total inclusive cross section cannot be measured because the detectors cover only a part $\Delta\Omega$ of the total solid angle Ω. Here, the cross section is integrated from the angular distribution, the differential cross section:

$$\frac{d\sigma}{d\Omega} = \frac{1}{nj}\frac{dN}{d\Omega} \tag{2.4}$$

which describes the probability of a secondary particle to be produced and emitted within the solid angle $\Delta\Omega$. The differential cross section is usually measured for the lighter of the products of the reaction. Such a cross section still represents an integration over all possible reaction channels. A separation thereof yields the partial differential cross section.

Furthermore, the cross section depends on the energy of the impinging particle[2]. This dependency is taken into consideration by excitation functions acquired from double differential cross sections:

$$\frac{\partial^2\sigma}{\partial T\partial\Omega} = \frac{1}{nj}\frac{\partial^2 N}{\partial T\partial\Omega}. \tag{2.5}$$

[2] In general, the double differential cross section can be a function of projectile energy, ejectile energy, or the difference of the two, i.e. the transferred energy. However, according to literature [BWW08], projectile energy is used more widely for the definition.

Elastic and inelastic scattering

In collisions where solely the direction of the projectile momentum is modified, the reaction mechanism falls into the category of elastic scattering. If energy is exchanged as well so that one of the collision partners is left in an excited state, the scattering is called inelastic. The inelastic process implies an inner structure inherent in at least one of the collision partners, also inferring that, for example, in a reaction of protons with plastic scintillator material the nuclear processes with hydrogen will always be elastic.

With protons and other charged projectiles, scattering on the Coulomb potential must be taken into account. Coulomb scattering can be elastic or it can lead to an excitation of one or both collision partners, where part of the kinetic energy is transferred to an inner degree of freedom of the nuclei. Whenever the distance between the collision partners is big as compared to their Compton wave length, a semiclassical approach can be used to describe the Coulomb excitation: the transportation of the particles is modelled via Rutherford scattering and the excitation process is introduced as a perturbation of first or, in complex cases, higher orders. The most common kind of Coulomb excitation are quadrupole transitions.

There are two mechanisms of elastic scattering due to the nuclear potential. Shape elastic scattering preferably occurs in proximity of the surface of the nucleus. In contrast, compound elastic scattering occurs when the particle enters the target nucleus to form a compound system which subsequently disintegrates into its input channel constituents. In theory, the compound elastic part of the reaction could be distinguished from the shape elastic part through their respective decay times of 10^{-16} s and 10^{-22} s.

Inelastic scattering has occurred when one or both collision partners are left in an excited state. Here, energy as well as momentum are exchanged during the process. There are single-particle and collective excitation mechanisms, the latter associated with a deformation of the potential well. The scattering on a nuclear potential is usually approximated by a plane wave hitting a scatter center. The scattered wave is spherical and carries the information of the angular scattering distribution in its amplitude. The wave function for the scattering process is composed of the plane wave e^{ikz} and the spherical wave $e^{i\vec{k}\vec{r}}/|\vec{r}|$:

$$\psi(\vec{r}) = A[e^{ikz} + f(\theta)\frac{e^{i\vec{k}\vec{r}}}{|\vec{r}|}] \tag{2.6}$$

The factor A takes normalisation and boundary conditions into account and the amplitude factor $f(\theta)$ is the scattering amplitude. The latter has the dimension of length and its squared absolute value yields the differential cross section:

$$\frac{d\sigma}{d\Omega} = |f(\theta)|^2 \tag{2.7}$$

Using this stationary description, elastic scattering can be associated with the case where the total fluxes of the incoming and outgoing waves are equal and only their phases differ. Inelastic processes alter the flux of the wave as well. Figure 2.4 schematically shows single-particle and collective excitations of the target nucleus.

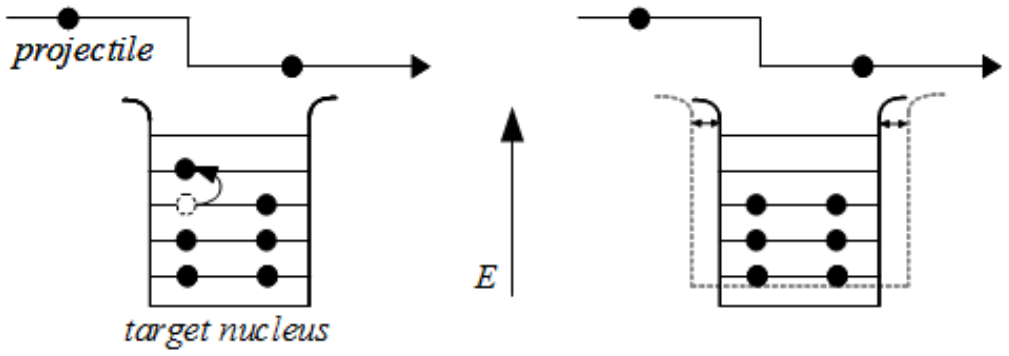

Figure 2.4.: Left: single-particle excitation; right: collective excitation via deformation of the potential well

Nuclear reactions

While in elastic and inelastic scattering only the direction, momentum, and energy of the particles may change, in nuclear reactions they collide to produce entirely different particles from those in the input channel. In contrast to the spontaneous mechanism of radioactive decay, this process must be initiated by one of the collision partners.

The sum of kinetic energies is not conserved in a nuclear reaction because the initial and final particles have different binding energies. In order to assess the amount of energy which is lost to or gained from the difference in binding energies, the Q value is defined as the difference of summed kinetic energies of the initial and final states:

$$Q = E_{final} - E_{initial} \tag{2.8}$$

Still, overall energy is conserved, meaning that the Q value is also the difference between the rest masses of the initial and final state:

$$Q = \Delta m c^2 \qquad \Delta m: \text{ mass defect} \tag{2.9}$$

When $Q > 0$ the reaction is called exothermal. It is called endothermal in case $Q < 0$. Here, due to conservation of momentum, the projectile must have a kinetic energy higher than a certain threshold E_{thr} which depends on the Q value itself and the scattering angle ϑ:

$$E_{thr} = -Q\frac{m_b + m_B}{m_b + m_B - m_a} \qquad for\ \vartheta = 0° \tag{2.10}$$

where subscripts b and B denote the ejectile and the remaining nucleus, respectively, and the mass of the projectile particle is indicated by the subscript a. The energy threshold is lowest for $\vartheta = 0°$.

Direct reactions

In analogy to elastic scattering there are mechanisms of varying time duration representing nuclear reactions. In direct reactions the wave functions of initial and final states

are fairly similar, i.e. the number of transition steps inside the nucleus is small. Basically, only few degrees of freedom of the system play any role in a direct process. These reactions are fast and take about as much time as a particle of ≥ 10 MeV energy takes to pass through a nucleus: 10^{-23}-10^{-22} s. Direct reactions will rarely occur below 10 MeV projectile energy, possibly between some of the excited compound states which are introduced further in this section.

The angular distributions of secondary particles are not symmetrical in a direct reaction - they show a strong intensity gradient in the forward direction due to the small momentum transfer from the projectile to the target. Since these reactions preferably take place near the surface of the nucleus, a diffraction pattern can be observed as in the case of scattering on a potential well. Mostly, the reaction regimes involved are so-called transfer reactions where one or several nucleons are exchanged between the collision partners. Possible direct reaction mechanisms are:

Stripping A nucleon of the flying by projectile is captured by the target, e.g. (d,p).

Pick up A nucleon is unhinged from the target nucleus by the projectile, e.g. (p,d).

Knock on The nucleon captured by the projectile is in an unbound state as opposed to pick up, e.g. (p,pn) as opposed to (p,d).

Cluster transfer Several nucleons are exchanged between projectile and target, e.g. (^{7}Li,t).

Kick off The projectile remains captured inside the target and another nucleon leaves in its stead.

Charge exchange The projectile and ejectile are different particles, e.g. (p,n). This is a special case of a kick off reaction.

The kick off process can only be distinguished from compound inelastic scattering if the types of projectile and ejectile particles differ. Especially at large scattering angles the direct and compound processes superpose strongly and can rarely be separated. Figures 2.5(a) to 2.5(d) show some of the above processes schematically.

Resonances

The cross sections show their strongest gradients with respect to energy in so-called resonance reactions. This type of reaction occurs when a particle within a nucleus accumulates more energy than its binding energy and enters the continuum of unbound states. Here, the wave function does not disappear outside of the potential well, as is the case with bound states. This means that the particle can pass the potential well in both directions (capture and emission). The likelihood with which the nucleon will move across the margin is linked to the gradient of the wave function amplitude at this point. The best gradient for a particle to move in or out of the potential well is zero, i.e. when the amplitudes just inside and outside of the margin are equal.

The width of the resonance depends on how much this gradient varies when the energy of the projectile particle is changed. If its dependence on energy is high then the resonance width $\Gamma_{resonance}$ will be small. The total width of the resonance reaction, Γ_{total}, is additionally broadened when the particle loses energy inside the nucleus by bouncing out other nucleons and by gamma transition between states. These processes lead to an attenuation of the wave. Thus, the total width is a sum of the "particle width" $\Gamma_{resonance}$ and the "reaction width" $\Gamma_{reaction}$:

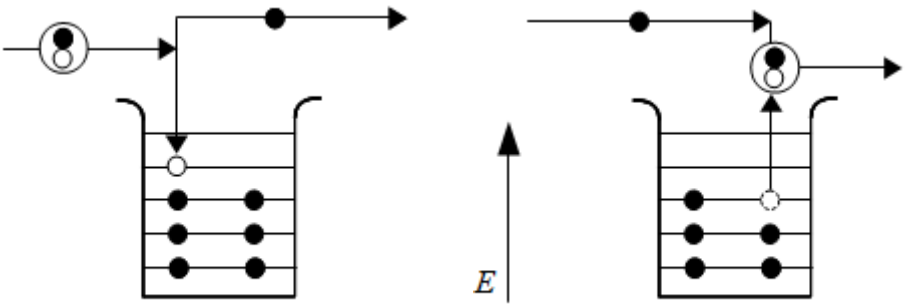

(a) stripping (b) pick up

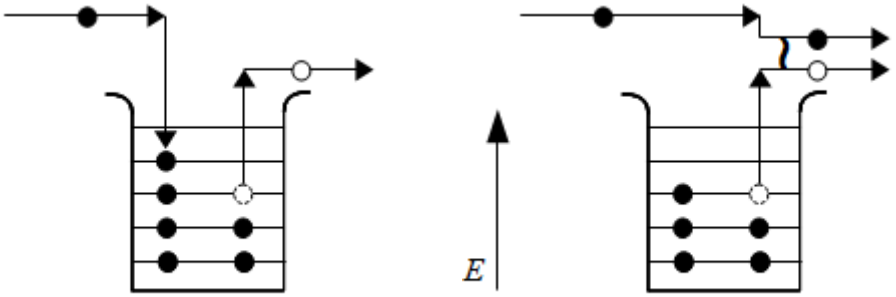

(c) kick off (d) knock on

Figure 2.5.: Direct nuclear reaction mechanisms. The full black circles represent nucleons inside the potential well and protons inside the deuterium nucleus. The full white circle with solid border represents a neutron in the deuterium nucleus. The full white circles with dashed border represent holes.

$$\Gamma_{total} = \Gamma_{resonance} + \Gamma_{reaction} \tag{2.11}$$

In order to assess the resonance cross section quantitatively, a logarithmic derivative of the wave function at the well margin is introduced. A resonance then occurs when the derivative is zero, as stated above. The total cross section for the resonance process is then [MK79]:

$$\sigma_{resonance} = \frac{\pi}{k^2} \frac{\Gamma^2_{resonance}}{(E - E_{resonance})^2 + \frac{1}{4}\Gamma^2_{total}} \tag{2.12}$$

where k is the wave number. Expression 2.12 is also known as the Breit-Wigner formula. This formula can only be applied when there is essentially just one resonance level involved in the capture of the projectile. This is normally the case when the resonance width Γ is small as compared to the average level separation D, i.e. when the excitation energy, and, accordingly, the projectile energy is small.

Compound processes

At low energies the effect may occur that neither the projectile nor the target nucleons possess enough energy to leave the nucleus. In this case a so-called compound nucleus is formed which is excited by the kinetic energy of the incident particle minus the kinetic energy of the centre of mass system plus its binding energy. This excitation energy is dissipated among all nucleons until one of them receives enough energy to leave the compound. This type of mechanism can last about 10^{-16} s and is thus much slower than a direct reaction. Through the repeated statistical process of energy redistribution the system does not retain the memory of the input channel. It means, the course of decay of the compound nucleus does not depend on the particles by which it was created but only on its nucleus type and excitation energy.

Since the half-life τ and the energy width Γ of the system are interconnected via

$$\tau = \frac{\hbar}{\Gamma} \tag{2.13}$$

one can expect the cross sections of direct reactions to change slowly with respect to projectile energy, while compound processes show a very high dependence on it. Strong resonances in cross sections can therefore often be observed for reactions which proceed through an intermediate compound nuclear state.

As stated in equation 2.7, the cross section of a nuclear reaction equals the squared transfer amplitude between the input channel and the final state. This "reaction amplitude" can only be properly described by existing nuclear models for the cases of direct reactions. With compound reactions the statistical process is so complicated and the temporal states are so various that only average values can be predicted.

As already stated above, the input and output channels of the compound reaction can be seen as independent from each other due to the relatively long life time of the process. This circumstance can be explained in more detail if it is viewed as a set of resonances. The transfer amplitude between the initial and final states is combined from a complicated sum of individual amplitudes which superpose with different phases. Since the system has so many degrees of freedom the assumption can be made that these individual phase shifts stem from a stochastic distribution and are not correlated to each other. This so-called random phase approximation is the basis of the so-called statistical model. The latter can be applied safely in the energy range between 10 and 20 MeV.

Basically, when a nucleus is excited by a projectile with the energy E there are many ways to dissipate this energy between the particles of the compound nucleus of mass A_c. Accordingly, there are many ways in which one particle might leave the compound system bearing an energy $0 < \epsilon < \epsilon_{max}$ and leave the remaining nucleus excited by an energy $E - \epsilon$. When a particle is emitted with an energy ϵ_{max} the nucleus is left in its ground state. In other words, the cross section for the decay is directly related to the number of possibilities to dissipate the energy $E - \epsilon$ between the $A - 1$ remaining nucleons with respect to the number of possibilities to dissipate E among all A particles. Each of these configurations corresponds to an excitation level or state.

When the width of these energy levels becomes greater than their distance, interference effects might be expected to occur between the individual resonances. In the statistical model these states also have randomly distributed phase shifts so that the in-

terference terms disappear when the cross section is averaged over an interval $\Delta E < \Gamma$. In accordance with the statistical model all configurations are considered to be equally likely. A direct measure for the number of configurations is the level density defined as the number of excitation levels per energy step. In practice, the Fermi gas model described further in this section is employed to obtain a realistic result for the level density.

Looking at the energy spectrum of emitted particles a few separate resonances can be observed near the maximum emission energy ϵ_{max}. These lines represent discrete excited states of the remaining nucleus. At lower ejectile energies the original excitation levels are closer together and have a higher width so that the spectrum becomes continuous and broad. Here, it corresponds to a Maxwell-Boltzmann distribution. Because the process of particle emission by a compound nucleus resembles the evaporation of molecules from the surface of a hot liquid, the process is often referred to as evaporation and its characteristic energy spectrum is called the evaporation spectrum. During evaporation the compound nucleus will rarely emit other particles than neutrons, protons, α, and γ.

Due to the independence of the initial and final states the cross section for the compound reaction can be factorised into a creation and a decay part:

$$\sigma_{\alpha\beta} = \sigma_{\alpha c} G_{c\beta} \tag{2.14}$$

where the subscript c denotes the compound nucleus, and α and β represent the input and output channels, respectively. G_β is the probability of decay into output channel β.

In order to obtain the total cross section for the emission of a particle at a certain energy, the transmission factor, i.e. the probability to cross the potential well margin, must be taken into account. In order to achieve this the inverse approach is used, i.e. the probability for a particle with energy ϵ to form a compound nucleus is determined.

The absolute cross section for the transition from initial state α to final state β with an emission energy ϵ_β can be determined via the Weisskopf-Ewing formula:

$$\sigma_{\alpha\beta}(\epsilon_\beta) = \sigma_{\alpha c} \frac{W_{c\beta}(\epsilon_\beta)}{\sum\limits_{\beta} \int W_{c\beta}(\epsilon)\, d\epsilon} \tag{2.15}$$

where W denotes the decay probability derived from the corresponding level density taking into account the transmission factors and the angular momentum. In fact, since the latter is conserved in nuclear reactions, the angular momentum of the final state is coupled with the angular momentum of the input channel. Therefore, the factorisation of the cross sections has to be carried out separately for each angular momentum state. In fact, angular momentum values up to $l_{max} = R/\lambda\!\!\!^{-}$ are of interest.

The energy spectra observed in experiments often show an excess of particles with relatively high energies as compared to the expected evaporation spectrum. This contribution is created just before the statistical equilibrium is reached, i.e. the compound nucleus is created. Accordingly, the underlying processes are categorised as pre-compound.

Figure 2.6 shows a schematic overview of the nuclear processes described in this section with their branching mechanisms.

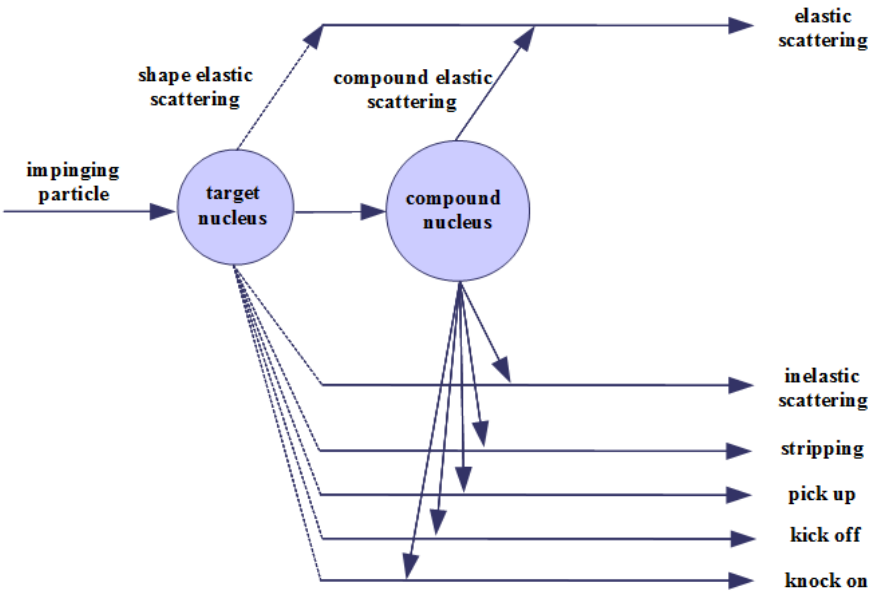

Figure 2.6.: Overview of nuclear processes in the intermediate energy range. Direct reaction mechanisms are indicated by dashed lines.

2.4. Models of nuclear interactions

Fermi gas model

The Fermi gas model describes light nuclei with proton and neutron numbers smaller than 20 as a statistical ensemble. With nucleons being fermions and obeying the Fermi-Dirac statistics the condition can be imposed that all Pauli allowed states within the nucleus are occupied in its ground state. Thus, despite the strong force, there is no possibility for a constituent to collide with another and change its state of motion, or any of its quantum numbers, so long as no external energy is fed into the system.

In order to determine the states of the nucleons, a piecewise constant nuclear potential is assumed, usually a simple rectangular potential, to which the effect of all other nucleons is averaged. Then the state of each particle can be determined by solving the time-independent Schrödinger equation for one particle inside this rectangular potential. As a result, the number of possible states in a momentum interval dp can be described for a particle moving inside a box with an edge length of a:

$$dn = \frac{a^3 p^2}{2\pi^2 \hbar^3} dp \tag{2.16}$$

Integral values of n correspond to lattice points within the phase space and denominate allowed energy eigenvalues. Provided that the volume of the phase space equals $4\pi p^2 dp$ and is defined in common by the volumes of the position space (a^3) and the momentum space, the content of equation 2.16 is often formulated as "inside a phase space

volume of size h^3 there is one possible state". Taking the Pauli exclusion principle into account, two nucleons with opposite spins can be assigned to each one of these states. Also, since the nucleus contains neutrons and protons, of which only the latter are subject to Coulomb force, the system has to be treated as a compound of two independent Fermi gases with unequal energy ratios.

In the ground state of the nucleus with its temperature $T = 0\ K$, the highest energy state which can be occupied by a nucleon represents a limit called Fermi energy associated with a corresponding Fermi momentum. The total kinetic energy $E_0(N')$ of a nucleon species N' (proton or neutron) can then be approximated in ground state by:

$$E_0(N') = \frac{3}{5} N' E_F \tag{2.17}$$

where E_F is the Fermi energy which itself can be approximated from the density of states by:

$$E_F = \frac{1}{2m} 3^{\frac{2}{3}} \pi^{\frac{4}{3}} \hbar^2 \left(\frac{n}{a^3}\right)^{\frac{2}{3}} \tag{2.18}$$

Optical model

The optical model is preferably applied in such nuclear reactions where averaged potentials can be assumed and global effects play a greater role than individual interactions between nucleons. The model has proven successful in explaining nuclear reactions in which the incident particles have energies of about 1 MeV-1 GeV. Here, the coupling of elastic and inelastic processes is based on a complex potential with its real part describing the scattering and its imaginary part associated with absorption effects. The potential has the form:

$$U(r) = V(r) + iW(r) \tag{2.19}$$

In order to accurately reproduce measured cross sections the optical potential is chosen empirically. A plausible form is selected and its parameters are determined by fitting the potential to measured scattering cross section data. Once the potential and its parameters are determined, differential cross sections can be calculated and compared to measured angular distributions. The total cross section can then be defined as a sum:

$$\sigma_{tot} = \sigma_{shape\ el.} + \sigma_{abs} \tag{2.20}$$

where $\sigma_{shape\ el}$ denotes the shape elastic cross section of projectiles scattered elastically on a potential which can be deformed. The absorption part of the equation is denoted by σ_{abs} and combines the cross sections of nuclear reactions and compound elastic scattering:

$$\sigma_{abs} = \sigma_{compound\ el} + \sigma_r \tag{2.21}$$

The optical potential does not take the inner structure of the nucleus into account. All inelastic processes including inelastic scattering and resonances are treated as absorption. Thus, only averaged cross sections can be obtained with this model and resonances

cannot be predicted. However, in many cases it is exactly the averaged cross section that is of interest, and in these cases the optical model finds its application.

Shell model

In contrast to the Fermi model where the nucleus is viewed as a statistic ensemble the shell model treats the nuclear matter as a configuration of independent particles. The primary benefit of such a single particle model is the possibility of calculation of individual nuclear properties like the excitation energy and the magnetic momentum.

The nucleus is described by the Shrödinger equation using an averaged potential as a function of distance, i.e. radius inside the nucleus. There are two basic potentials which can be solved analytically - the rectangular potential V_{rect} and the harmonic oscillator potential V_{ho}:

$$V_{rect}(r) = \begin{cases} -V_0 & \text{for } r \leq R \\ 0 & \text{for } r > R \end{cases} \tag{2.22}$$

$$V_{ho}(r) = \begin{cases} -V_0[1-(r/R)^2] & \text{for } r \leq R \\ 0 & \text{for } r > R \end{cases} \tag{2.23}$$

A more realistic intermediate form is represented by the Woods-Saxon potential:

$$V_{WS}(r) = -V_0\left[1+e^{\frac{r-R}{a}}\right]^{-1} \tag{2.24}$$

with parameter a accounting for the uncertainty at the nucleus surface. The corresponding solution to the Schrödinger equation has to be found numerically.

2.5. Monte Carlo simulation in particle therapy

Monte Carlo simulation (MC) plays a great role in the various research fields of particle therapy and its relevance to clinical applications is steadily increasing. Being the method of choice for the detector evaluation presented in this thesis Monte Carlo simulation is introduced in a nutshell in section 2.5.1. The various uses of MC in particle therapy are outlined in section 2.5.2. Section 2.5.3 provides a detailed account of the Monte Carlo toolkit GEANT4 used in this thesis. An overview of other Monte Carlo transport codes employed in proton and ion therapy is presented in section 2.5.4.

2.5.1. The basic principles of Monte Carlo simulation

Generally speaking, a Monte Carlo (MC) simulation is a method which uses random numbers. Monte Carlo methods are used widely, from economics to nuclear physics to regulating the flow of traffic.

As in the case of particle transport, the method of Monte Carlo simulation can describe statistical processes in a numeric way whenever they cannot be solved analytically. This especially applies to cases where a high number of particles interact with each other in many different and, partially, competing ways.

In a simplified illustration, the first step in a Monte Carlo simulation procedure involves the definition of some inputs. In the water phantom simulation described in section 2.1 such inputs are the material, geometry, and position of the phantom, the target region and surrounding space. Additional inputs are the beam parameters like the primary particle type and the beam's initial energy along with a specific distribution of its creation vertex. The cross sections for the various interaction mechanisms of the primary and secondary particles with matter are also input in the form of probability distributions.

The algorithm of particle transport will simulate each primary particle as a one-particle experiment by first sampling randomly from the given distribution of creation vertices and then continue transport and simulation of collisions by sampling from available probability distributions. The latter can be based on some theoretical model, actual experimental data, or a parametrisation of a theoretical distribution based on measured data.

The amount of all possible configurations of the simulated system is represented by its phase space. Therefore, the simulation procedure can be defined as a process of randomly sampling the phase space. Each configuration (or point in phase space) is then weighted using the input probability distributions.

In order to find an approximate solution within a certain statistical limit a great number of such one-particle experiments also called histories need to be simulated. This means that the phase space needs to be sampled many times until an accurate description of the system's properties can be obtained. Putting limited accuracy of numbers and rounding errors aside, the accuracy of the simulation result also depends on the quality of the random number generator. The latter creates a chain of preferably unrelated pseudo-random numbers based on a seed (e.g. the computer clock).

In the task of detector evaluation Monte Carlo simulation can help to create a more thorough understanding of detector performance by enabling complete control of the "experimental" conditions (inputs) in this "computer experiment", as Landau and Binder call it in their book "A guide to Monte Carlo simulations in statistical physics" [LB09].

2.5.2. Uses of MC simulation in particle therapy

There is a wide range of applications of Monte Carlo simulation in particle therapy:

- Patient dose calculations: MC is currently the most accurate method which takes into account tissue inhomogeneities. If nuclear reactions are considered by the transport code, the unwanted neutron dose to the patient can be calculated serving as an estimate for the risk of secondary cancer.

- Monte Carlo simulations can provide the most accurate prediction of the biological dose. Especially in the case of ^{12}C-ions up to 20% [PMG07] of the energy is deposited by secondary fragments, mostly boron and helium. Since the biological effectiveness essentially depends on particle type and energy, the biological dose contributed by these fragments can be taken into account via Monte Carlo.

- In treatment head (nozzle) design Monte Carlo can help to choose the configuration which will optimally fulfill the required specifications. This applies in

particular where complex beam scattering and energy modulation systems are involved.

- Dosimetric properties of new accelerator technologies and alternative particle types can be investigated.
- Also, adequate shielding of particle therapy facilities can be designed. This capability helps to optimise the shielding of manned space crafts, as well.
- In vivo quality assurance can be aided by comparison of PET images acquired right after the irradiation to equivalent images generated from the MC simulation of the prescribed radiation fields.
- Accurate corrections can be calculated for dosimetry with air filled ionisation chambers using Monte Carlo methods.

2.5.3. The GEANT4 toolkit

GEometry ANd Tracking (GEANT4) is a free open source toolkit for Monte Carlo simulation [AAA+03]. So far, it is the only successful object-oriented environment for Monte Carlo simulation written in C++. It involves advanced software-engineering techniques providing a clear hierarchical structure of domains each with their own dedicated working group of experts.

Initially, the development of version 4 was proposed by a collaboration of CERN and KEK in 1994. The new object-oriented and more powerful version of the old Fortran Geant3 code was aimed to provide the functionality and flexibility necessary for the next generation of high energy physics experiments. Soon after the first release in 1998 it became apparent that other communities like nuclear, space, accelerator, and medical physics would benefit from such a toolkit. Hence, the collaboration has grown and new developments and validation are contributed by many groups from a diversity of application fields. At present, the GEANT4 toolkit can be seen as a repository which contains a large part of all existing knowledge on particle interactions.

The Physics Reference Manual [Phy08] spans more than 500 pages and contains models for electromagnetic interactions of leptons, photons, hadrons and ions, and hadron interactions. Any particle can be simulated at any energy, from a few eV to several TeV. The physics capability also includes scintillation and optical photon propagation.

The definition of particles and their interactions must be carried out by the user. There are three mandatory user action classes one of which is the Physics List. In this class the application developer first defines all particles which are created during the simulation. To each of these particles one or more processes can be registered represented by C++ classes which describe how and when a certain interaction takes place along the particle trajectory. One or more models can in turn be registered to a process. According to the Physics Reference Manual, a model is a C++ class which implements the details of an interaction, such as its kinematics.

The abundant set of physics is the heart of the toolkit. The separation of cross section computation from the ways in which cross sections are accessed and used allows the user to add new or variant physics models by overloading the corresponding classes.

With other procedural codes this poses a great difficulty because of the size of the implementation, its complexity and interdependency.

Other mandatory user action classes are the Primary Generator Action and the Detector Construction. In order to describe the space in which the particles will be propagated GEANT4 offers many solid geometry types which can be combined via Boolean operations and allows the user to import geometry descriptions from computer-aided design tools. Detector Construction also includes the definition of materials and their properties (e.g. density, optical properties). The capability to model time-dependent geometries makes the toolkit suited for intensity-modulated radiation therapy and organ motion studies [PV05]. The Primary Generator Action includes the definition of the primary particle source, its energy and creation vertex.

Additional user action classes, like Run Action, Event Action, Tracking Action, and Stepping Action allow to access and manipulate the simulation data at increasing levels of refinement and detail. While a G4Event class represents the creation of one primary particle and its transport as well as the transport of its secondaries through the volumes implemented in the Detector Construction, the G4Run class holds any number of such events, executed one after another. G4Track corresponds to a single particle and its trajectory and G4Step contains information on a certain trajectory segment.

Since a great volume of data can be produced during the simulation, GEANT4 includes interfaces to an armada of intelligent visualisation and analysis tools (e.g. the HepRApp geometry viewer and the ROOT toolkit). The system also has an interface to the DICOM toolkit (dcmtk) which is of great importance to the particle therapy community.

2.5.4. Other Monte Carlo toolkits

SHIELD-HIT

SHIELD-HIT is the "medical" version of the SHIELD code - a hadron transport code developed by the Joint Institute for Nuclear Research (JINR, Dubna) [GSA+04] in collaboration with the Karolinska Institutet (KI, Stockholm) and the German Cancer Research Center (DKFZ, Heidelberg). The transport of protons and heavier ions in the energy range of 1 MeV to 1 TeV and down to thermal energies for neutrons is included in SHIELD-HIT.

Just as most of the other codes it uses the Bethe-Bloch equation to calculate the stopping power values including effective charge corrections at lower energies. Multiple scattering is modelled according to Moliere and inelastic nuclear reactions are simulated by the multi-stage dynamical model (MSDM). Developed at the JINR and the Institute for Nuclear Research of the Russian Academy of Science (INR RAS, Moscow) the MSDM includes a fast cascading stage carried out via binary collisions between the target and projectile nucleons followed by pre-equilibrium emission and several models for equilibrium deexcitation such as Fermi breakup, evaporation/fission and multifragmentation.

In [HSJP09] the MSDM has been found to be inferior to the binary cascade model of GEANT4 in reproducing experimental proton data measured as a charge deposition

inside a layered Faraday cup spanning the whole Bragg curve range at energies of 100 and 200 MeV.

FLUKA

FLUKA is another general purpose Monte Carlo code developed at CERN and Instituto Nationale di Fisica Nucleare (INFN, Italy) [FFR+03]. Like SHIELD-HIT, FLUKA is a so-called exclusive code, where conservation laws are enforced at each step of the simulation and results are checked against experimental data at the level of a single interaction.

The code can handle about 60 different particles including energies of up to thousands of TeV for photons and electrons and up to 20 TeV for hadrons. FLUKA can handle relatively complex geometries through the use of the Combinatorial Geometry (CG) package but does not consider nested and twisted geometries which can be used in GEANT4. For users who do not have a good experience in object oriented programming FLUKA offers an advantage since no programming is required from the user for most applications.

In the energy range relevant for radiotherapy inelastic nuclear reactions are modelled using the PEANUT package which includes a generalised intra-nuclear cascade and preequilibrium evaporation. Equilibrium deexcitation includes evaporation, fission, Fermi breakup and gamma deexcitation. Elastic and inelastic nucleon-nucleon cross sections are mainly generated from parametrised fits based on available experimental data. In addition tabulated data are used for nucleon-nucleus interactions.

Apart from GEANT4, FLUKA is the only code used in particle therapy which can handle scintillation processes and track optical photons. Compared to other MC codes it offers only few built-in viewers and is unable to accept a geometry from a CAD tool via the STEP format. The user community of FLUKA is about half the size of GEANT4 and MCNPX.

MCNPX

MCNPX stands for "Monte Carlo N-Particle eXtended" and is a general purpose transport code written in the Fortran90 language and developed by the Los Alamos National Laboratory (LANL, USA) [McK09]. It can track 34 particle types (nucleons and light ions of $Z \leq 2$) in addition to more than 2000 heavy ions produced during the simulation [Lab].

The size of the MCNPX user community is comparable to that of GEANT4 despite certain drawbacks such as not being able to simulate Cherenkov radiation or handle twisted geometries. For the simulation of nuclear reactions MCNPX offers a choice between the Bertini cascade, the FLUKA89 (for $E \geq 3$ GeV) and a few other models.

In 2006 Enger et al [EaRRL06] have compared the performance of MCNP and GEANT4 (version 6.0 patch 1) in neutron capture therapy. MCNP compared best with the experiments because it models thermal neutron scattering from chemically bound atoms as well as free atoms whereas GEANT4 only considers the free atom model. In the same year the simulation of the scattering from chemically bound atoms has been included in the GEANT4 toolkit as presented at the IEEE Nuclear Science Symposium [Koi06].

PHITS

The Particle and Heavy Ion Transport code System (PHITS) is written in the Fortran77 language and is mainly developed in Japan. Even though its user community is relatively small, PHITS is used for radiotherapy applications such as Boron Neutron Capture Therapy (BNCT) and carbon ion therapy.

Just as with FLUKA the geometry is simulated using the CG package. The energy loss of the particles is simulated according to the Bethe-Bloch mechanism and multiple scattering according to Moliere theory. For nuclear reactions at energies below 3 GeV PHITS offers the Bertini cascade model combined with the Generalised Evaporation Model for deexcitation. [INN02], [NNH$^+$05]

3. State of research

The first part of this chapter outlines the current stage of GEANT4 adaptation to particle therapy and summarises recent approaches to validate the GEANT4 nuclear models for proton and ion therapy, in sections 3.1 and 3.2, respectively.

In the second part, section 3.3 provides a detailed view on available experimental data. It is followed by an example GEANT4 simulation of a previously published experiment in section 3.5 showing rather unsatisfactory agreement with experimental data and indicating some of the issues which arise when simulating data produced by other groups.

3.1. Main uses of GEANT4 in particle therapy

The medical physics community has so far employed GEANT4 for the modelling of PET / SPECT / CT scanners and for various tasks within brachytherapy and external beam therapy with photons and light ions. Since it is rather unrealistic to develop a uniform physics model to cover a wide variety of particles and/or wide energy range, GEANT4 offers a mixture of theory-driven, parametrised, and empirical physics models, as stated in section 2.5.3. Here, with the aid of polymorphism cross-sections and models can be combined in arbitrary fashion to form one particular process.

As a consequence, the high number of physics choices might offer some difficulties to the unacquaintaned user. Therefore, in 2001 the medical imaging community started the development of a dedicated project: GEANT4 Application for Tomographic Emission (GATE) which enables the user to simulate advanced and complex scanner geometries without a profound knowledge of object oriented programming by providing an easy to learn scripting language [SST+07].

A GEANT4 based simulation framework for particle therapy has been developed in Japan. Primarily, it serves the purposes of validation of treatment planning, design of new beam irradiation systems according to facility specifications, and the discussion of best physics models across different therapy centres. A higher simplicity of use is achieved through introduction of interactive commands. Specifications of materials, geometry and others can be imported from ASCII and DICOM-RT files [AKK+07].

In 2004 Paganetti and colleagues were the first research group to use GEANT4 (version 4.5.2) for the simulation of the nozzle of an IBA [1] proton facility at the Massachusetts General Hospital (MGH). They found new ways to implement the complex shapes in the beam path and also made use of the 4D capability of GEANT4, i.e. simulation of moving geometries. Through exact geometry implementation the authors could

[1] Ion Beam Applications Group

reproduce measured dose distributions with an accuracy better than 1 mm [PJLK04].

In 2005 Pablo Cirrone et al presented an implementation of a proton therapy beam line for the treatment of ocular tumors with an energy of 62 MeV [CCG+05]. They also compared the simulated proton ranges to NIST data in water and PMMA and found the results to be in good agreement with each other. The lateral dose distribution simulated by GEANT4 also showed acceptable consistency with the measurement. The underlying simulation was included in the advanced example package of the GEANT4 distribution under the name "hadrontherapyexample".

In 2004, Jiang and Paganetti adapted GEANT4 to dose calculation based on Computer Tomography (CT) data sets [JP04]. The critical tasks primarily addressed in this paper were the handling of a voxel geometry, which can consume a lot of computation time and memory, and the conversion of Hounsfield units, which represent electron densities to material properties.

The authors achieved an efficient use of memory by defining the CT voxels in a parametrised volume - a volume which can have many daughter volumes with changing location, size, solid representation, and material properties. The parametrised volume is represented by a single object which dynamically changes its properties when representing different daughter volumes.

In order to provide the simulation with appropriate material compositions, the Hounsfield units were divided into 24 groups. Inside these groups, the element composition and the relative element weights remained the same while the mass density varied with the Hounsfield number. By assigning the mass density dynamically during the simulation through the application of a correction factor for the physics processes more computing time could be saved.

By 2007 they analysed the effects of this Hounsfield number conversion on proton dose calculations in more detail. It was found that small differences occurred between different approaches, mainly due to differences in element composition and mass density. These differences may play a significant role for organs at risk lying in the SOBP penumbra or distal regions [JSP07].

In summary, the application range of GEANT4 in particle therapy is very wide. This section provides a rough picture by marking a few corner stones of the issue. The overall coverage in literature is much more extensive as to be included in this thesis.

3.2. Previous validation of GEANT4 nuclear models in ion therapy

In the first part of this section two previous approaches to validate GEANT4 nuclear models for particle therapy are outlined including the relevant results and conclusions. The third paragraph deals with a theoretical discussion of epistemic uncertainties, i.e. uncertainties which are due to the lack of knowledge.

Faraday cup

In 2003 Paganetti and Gottschalk published a comparison of newly implemented nuclear reaction models in GEANT4 (version 4.5.0) to the older models of the GEANT3 FORTRAN77 code (version 3.2.1). Since the proton energy applied here was rather low at 160 MeV the choice of models in GEANT4 could be narrowed to the low energy model and the precompound model which is valid below 170 MeV. The models chosen in the GEANT3 code were GHEISHA and FLUKA [PG03].

A multilayer Faraday cup served as a detector for the charge produced by primary and secondary particles. Basically, an array of 65 0.3175 cm thick high density polyethylene (HDPE) sheets was used to stop the proton beam. Thin brass layers placed between the HDPE layers served as collectors for the charge.

As a result, a curve similar to the Bragg relationship could be observed with its build-up region entirely attributed to nuclear reactions while the Bragg peak was dominated by electromagnetic processes. By comparing the experiment to the according Monte Carlo simulations of the setup the authors inferred, that the GEANT4 precompound model and the GEANT3 FLUKA implementation showed a significantly better agreement with empirical data while FLUKA was still superior to GEANT4 in the prediction of the total charge. As a conclusion, Paganetti and Gottschalk state:

> *In all, one is left with the impression that the modernisation of GEANT was unfortunately not accompanied by an improvement in the nuclear model.*

A few years later the experiment was repeated with an updated version of GEANT4 (version 8.1.p01) where several nuclear reaction models were implemented their performance again being evaluated via comparison with Faraday cup measurements [JP08]. As a result, Jarlskog and Paganetti issued a recommendation for a list of physics choices to be used in proton therapy simulation. The recommended models are treated in more detail in connection with the setup of the detector simulation in chapter 4.

MCHIT

Igor Pshenichnov and colleagues developed a physics list for the simulation of light and heavy nuclei in tissue like media based on GEANT4. The model is called MCHIT and comprises the standard electromagnetic physics package for the simulation of energy loss, the binary cascade for inelastic nuclear interactions above 80 MeV, and the precompound model for energies below 80 MeV as well as data driven models below 20 MeV. Deexcitation of nuclei was accounted for by the Weisskopf-Ewing model below 3 MeV and by the Statistical Multifragmentation model above this energy. The latter also includes the Fermi breakup mechanism which will be described in detail in chapter 4.

In 2005 Pshenichnov et al compared Bragg curves and the production of secondary neutrons from beams of ^{12}C, and ^{18}O, and ^{20}Ne to data measured at the Gesellschaft für Schwerionenforschung (GSI, Darmstadt) [PMG05]. The authors found that the MCHIT reproduced the depth dose measurements well and that the dose contributed by secondary neutrons although varying with particle type and energy, did not exceed 1-2%.

In 2006 they investigated the distributions of positron emitting nuclei produced by proton and carbon-ion beams in polymethyl methacrylate (PMMA) phantoms [PMG06]. The β^+-activity predicted by the MCHIT model was in good agreement with experimental data. Only in the case of 110 MeV protons the measured distribution was considerably flatter than the one predicted by GEANT4. The total yields of most frequent β^+-emitters were predicted with good accuracy, as well.

In 2007 Pshenichnov et al showed the good agreement of their model with experimental data on depth dose distributions of ^{12}C-ion beams in water and PMMA [PMG07]. Similarly good results were obtained for the yields of β^+-emitters, the energy spectra of secondary neutrons, and the radial dose distributions.

In the same year the production and dose distribution of positron emitters produced by ^{3}He and ^{12}C beams were further analysed in [PLMG07]. Special attention was payed to the isotopes with half lives $T_{1/2} > 1$ s. This is due to the fact that image acquisition has to take place between beam spills for the scans not to be disturbed by the high amount of background radiation which is produced during a spill which takes about $1-3$ s time. Therefore, only those positron emitters are of interest, which can outlast the spill duration. From their simulations with the light ^{3}He-ion beam the authors found that in addition to the expected carbon fragments ^{10}C and ^{11}C, and oxygen fragments ^{14}O and ^{15}O, several nuclear pickup reactions contributed to the PET signal: ^{12}C(^{3}He,X)^{13}N, ^{12}C(^{3}He,n)^{14}O, ^{16}O(^{3}He,X)^{17}F, ^{16}O(^{3}He,p)^{18}F. The last isotope ^{18}F has a half live of 109.77 min and could be used for offline PET monitoring, although of course depending on tissue type, the signal might be distorted by metabolic washout.

In 2008 they presented additional simulation results comparing depth dose relationships and the production of secondary ions in light beams like proton and ^{3}He to beams of ^{12}C, ^{20}Ne, and ^{58}Ni [PMG08]. At low energies corresponding to small penetration depths the authors didn't find any significant differences between the beam modalities. At higher penetration depths the peak-to-entrance dose ratio of light particles was higher and therefore more beneficial. However, the lateral spreadout of the beam due to multiple scattering was also higher for the light proton and ^{3}He-ion beams.

Epistemic uncertainties

One recent publication by the group in CATANA, Italy carries out a sensitivity analysis concerning epistemic uncertainties of the GEANT4 simulation of 65 MeV protons [PBl+10] mentioned above and published in [CCG+05]. The uncertainties included in this study are those which occur due to lack of knowledge, in particular: incomplete understanding of fundamental physics processes, practical inability to treat the physics thoroughly, non-existing or conflicting experimental data for a physical parameter or model, the application of a physics model beyond the energy range it was validated in or with different target materials. Also, with parametrisations of experimental data not only errors on the cross sections can contribute but also the criteria by which the data are selected for the fit and the parametrisation or fitting process itself. This sensitivity analysis was not aimed to provide a validation against experimental data but rather to evaluate the qualitative and quantitative effects which a systematic variation of certain parameters would have on the simulation result. The authors found that the main uncertainties in the simulation of hadronic processes are mainly due to their intrinsic

implementation and the differing empirical parameters they are based on. In addition, the validation of the models is yet limited and there is no clear statement in literature as to whether the data sets used for the calibration of the models and those used for the validation are different. The largest differences in the models concern the production of secondary particle spectra. Especially different deexcitation mechanisms seem to play a greater role in the energy range ≤ 100 MeV.

In conclusion, the validation experiments and the discussion on epistemic uncertainties show that there is dire need for detailed and accurate nuclear cross section measurements which would enable a more thorough validation of GEANT4 for the use in particle therapy.

3.3. Databases dedicated to nuclear reactions

Among data bases containing nuclear reaction data there are two which are most broadly used: the Evaluated Nuclear Data File (ENDF) [2] and the Cross Section Information Storage and Retrieval System (CSISRS, pronounced 'scissors')[3]. The latter is more often referred to as EXFOR, which is an acronym of Exchange Format. The ENDF/B library has been developed by the Brookhaven National Laboratory (BNL) and provides a complete reference set of evaluated nuclear data based on experiments and theoretical predictions for use in nuclear calculations. For protons, the cross sections are predicted only up to an energy of 150 MeV. As an example, the excitation functions are shown for the reaction $^{12}C(p,2p)^{11}B$ in figure 3.1.

GEANT4 employs the ENDF/B library among other evaluated libraries for the calculation of cross sections and final states of neutron reactions. The data sets are stored in a format similar to ENDF6.

EXFOR has been initiated by four existing nuclear data centres in 1969. It is a set of definitions and conventions primarily designed for the transmission of experimental nuclear data information between these centres. In order to accommodate their diverse needs EXFOR is optimised for flexibility rather than data processing. Early on it became a leader in the handling of very large databases. Now, after 40 years, EXFOR is still in use and comprises data from 18683 experiments. [Hol05]

3.4. EXFOR data in terms of relevant reaction channels

In this section the results found in the EXFOR database will be used in order to assess the need for new measurements. Carbon and Oxygen isotopes represent the most abundant elements in the human body and this survey will be constrained to these targets. Since the first experimental runs of the time-of-flight spectrometer introduced further in

[2] `http://www.nndc.bnl.gov/exfor/endf00.jsp`, as of 14th of November 2010
[3] `http://www-nds.iaea.org/exfor/exfor.htm`, as of 14th of November 2010

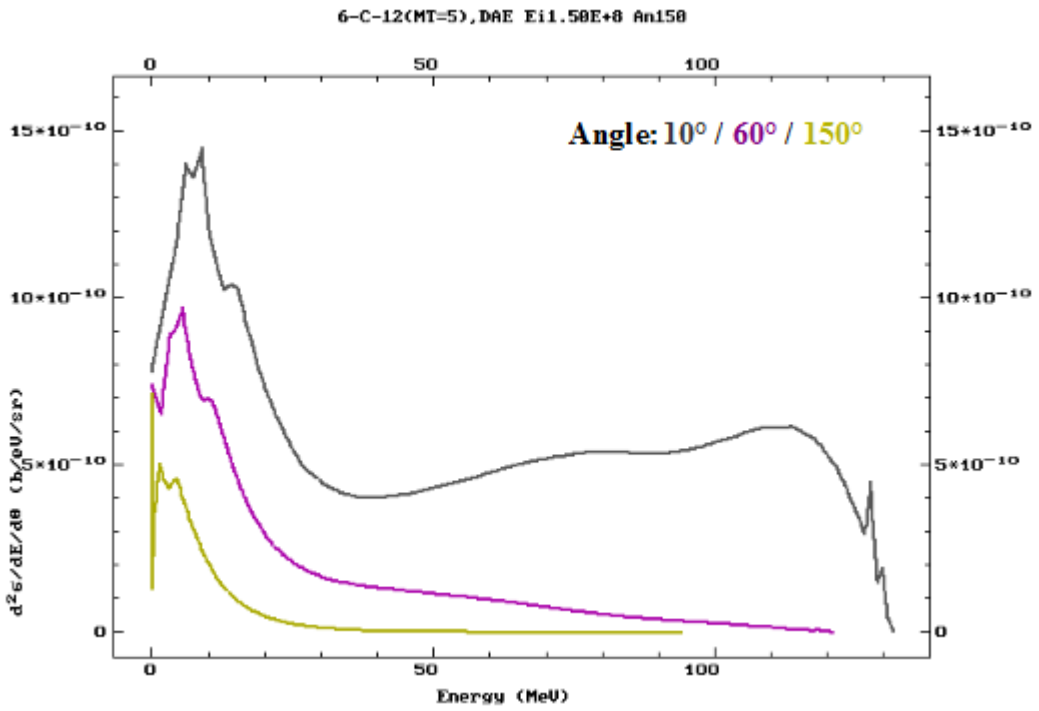

Figure 3.1.: ENDF data base: cross section of $^{12}C(p,2p)^{11}B$ reaction with respect to energy and angle.

chapter 4 were carried out with 200 MeV protons, this section and all following investigations within this work will focus on protons as projectile particles. Additionally, the experimental data of interest should cover the energy range relevant to proton therapy, namely ≤ 250 MeV.

3.4.1. Relevant reaction channels

For each target material the most frequent output channels were determined from a GEANT4 Monte Carlo simulation. Although, as pointed out in section 3.2, the simulation of nuclear processes in GEANT4 has not yet reached the desired accuracy for its application in therapy, it is clearly sufficient to provide an initial estimate of the most frequent reaction channels.

The simulation setup which served this task was a subset of the spectrometer simulation which will be described in detail in chapter 4. Here, the same Primary Generator has been used as well as the same Physics List. In terms of Detector Geometry, only the graphite target has been kept to determine the secondary particles produced in an inelastic proton process, i.e. a nuclear reaction. On a brief account, the simulation used here consisted of a 200 MeV proton beam, a graphite target, and a physics list which is currently considered optimal for the simulations in particle therapy, according to literature. The relevant output channels were determined by acquiring the secondary particle vectors from the Stepping Action and comparing their relative frequency.

Throughout this section, a commonly known notation from nuclear physics will be used to describe reactions: "target (projectile , emitted particles) residual nucleus".

Carbon

The naturally found isotope composition of carbon is ^{12}C : 98.89% and ^{13}C : 1.11%. The most frequent reaction channels found in the GEANT4 simulation are summarised in table 3.1.

Table 3.1.: Most frequent reaction channels of protons with graphite. The notation ^{xx}C is used for the purpose of completeness and includes the output produced by both carbon isotopes. However, due to the small concentration of ^{13}C, ^{xx}C corresponds to ^{12}C most of the time. Since some reaction channels can include one or more gamma photons otherwise remaining unchanged the notation γ' is used to include these cases.

$p^+ + {}^{xx}C \rightarrow$	$^{11}C + \gamma' + n + p^+$
	$^{11}B + \gamma' + 2p^+$
	$^{10}B + \gamma' + n + 2p^+$
	$2\alpha + 2n + 3p^+$
	$2\alpha + d + n + 2p^+$
	$3\alpha + p^+$
	$^{6}Li + \alpha + n + 2p^+$

As already mentioned, positron emitters play an important role in the field of in vivo quality assurance and Monte Carlo simulations are employed to predict PET images. Therefore, the following positron emitters have to be taken into account in addition to ^{11}C: ^{7}Be, ^{8}B, ^{10}C, and ^{13}N of which ^{8}B and ^{13}N are rarely produced and need not be considered. The channels through which ^{7}Be and ^{10}C fragments are produced by protons in a graphite target are listed in table 3.2.

Table 3.2.: Most frequent production channels of positron emitters created by 200 MeV protons in graphite. Notation ^{xx}C as in table 3.1.

$p^+ + {}^{xx}C \rightarrow$	$^{7}Be + {}^{3}He + 2n + p^+$
	$^{7}Be + \alpha + \gamma + n + p^+$
	$^{7}Be + \alpha + n + p^+$
	$^{7}Be + n + 2p^+ + t$
	$^{10}C + \gamma + 2n + p^+$

Oxygen

The naturally abundant isotope composition of oxygen is ^{16}O : 99.763%, ^{17}O : 0.0375%, and ^{18}O : 0.1995%. In order to identify the relevant output channels created by 200 MeV protons in oxygen, the target material of the GEANT4 simulation described above had been replaced by this element composition. The density of the material has been increased by a factor of 1000 thus increasing the inelastic event rate and saving computation time. The channels which were found most frequently are summarised in table 3.3.

Table 3.3.: Most frequent output channels in the GEANT4 simulation with 200 MeV protons hitting an oxygen target. As with carbon, the notation ^{xx}O is used for the purpose of completeness and will almost always turn out to be ^{16}O. Again, some reaction channels can include one or more gamma photons otherwise remaining unchanged and the notation γ' includes these cases.

$p^+ + {}^{xx}O \rightarrow$	$^{16}O + \gamma' + p$
	$^{15}O + \gamma' + n + p$
	$^{15}N + \gamma' + 2p$
	$^{14}N + \gamma' + n + 2p$
	$^{13}C + \gamma' + n + 3p$
	$^{12}C + \alpha + \gamma' + p$
	$^{12}C + \gamma' + 2n + 3p$
	$^{10}B + \alpha + \gamma' + n + 2p$
	$3\alpha + 2n + 3p$

Taking into consideration positron emitters, the cross sections of the isotopes ^{14}O, ^{13}N, and ^{11}C must be considered in addition to ^{15}O which is already included in table 3.3. The most common reaction channels for the three remaining isotopes are listed in table 3.4.

Table 3.4.: Most frequent positron emitter channels in the GEANT4 simulation. Notation ^{xx}C and γ' as in table 3.3.

$p^+ + {}^{xx}O \rightarrow$	$^{14}O + \gamma + 2n + p$
	$^{13}N + \gamma' + 2n + 2p$
	$^{11}C + \gamma + n + 2p + t$
	$^{11}C + \alpha + \gamma' + n + p$
	$^{11}C + \gamma + 3n + 3p$

3.4.2. EXFOR data

The data base search and its results presented in this section did not focus on certain channels explicitly, but rather on the production cross sections of the corresponding residual isotopes. Using the EXFOR search mask, the target material has been entered along with the projectile proton, the residual isotope of interest, and the relevant energy range of 0-250 MeV. Then, the result format was the excitation function for the production cross section of the isotope in question.

Carbon

As can be concluded from tables 3.1 and 3.2, the residual nuclei of interest are ^{11}C, ^{10}C, ^{11}B, ^{10}B, ^{7}Be, and ^{6}Li. The corresponding excitation functions output by EXFOR are shown in figures 3.2 to 3.7.

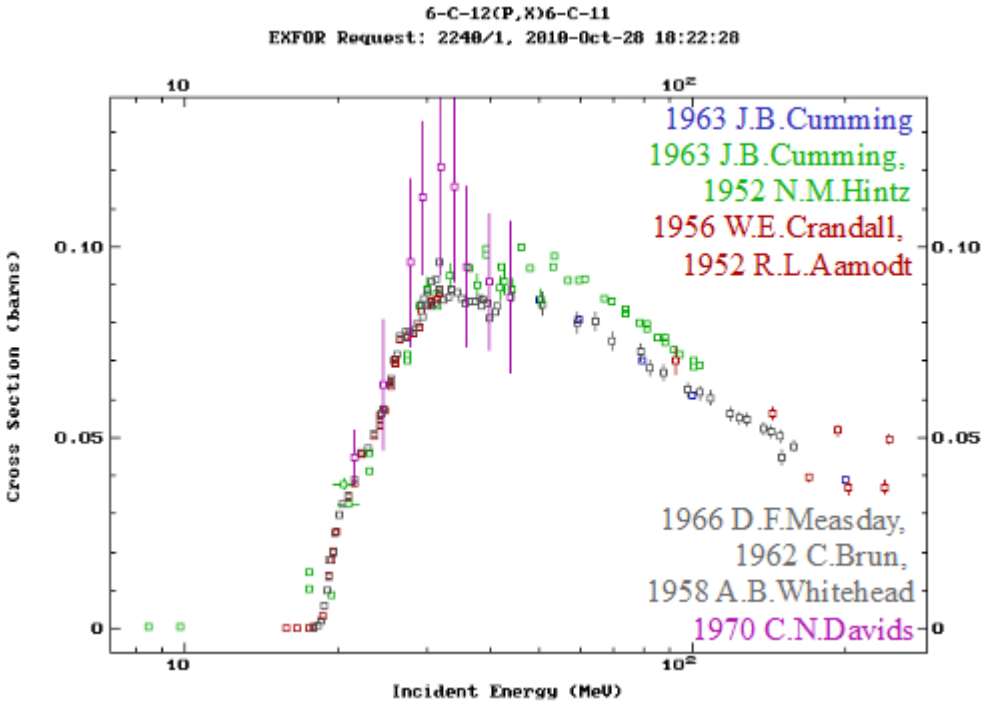

Figure 3.2.: Excitation function for the reaction ^{xx}C(p,X)^{11}C. Here and in the following EXFOR plots different colors encode data sets published by different authors. Some data sets are presented in combination with others.

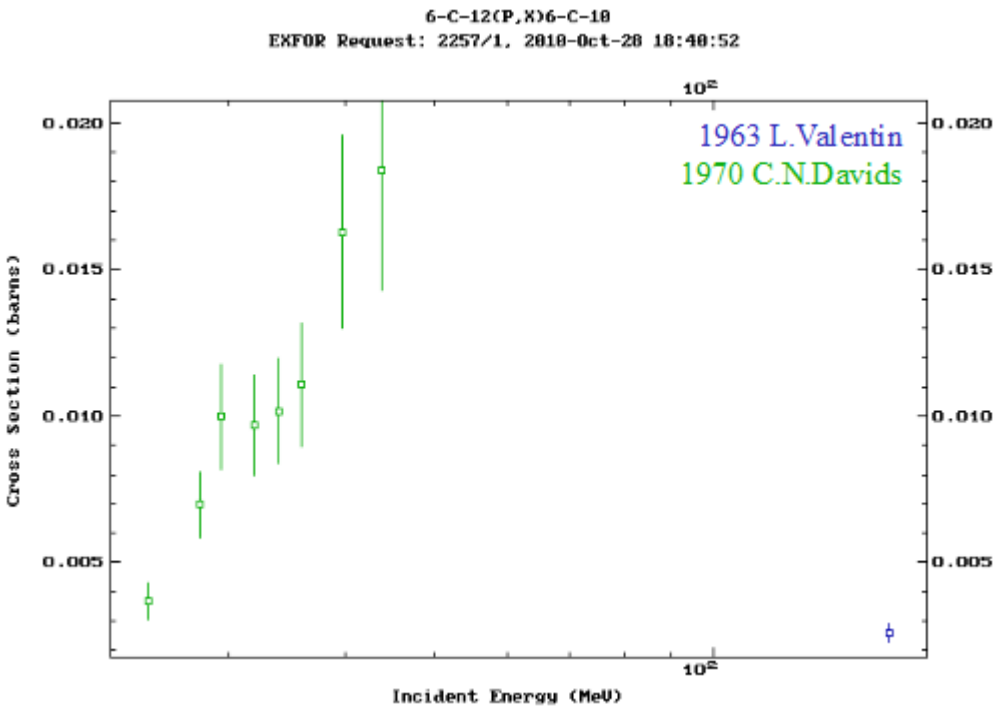

Figure 3.3.: Production cross section of ^{10}C with respect to the energy of the projectile proton.

The ^{12}C(p,X)^{11}C-reaction shown in figure 3.2 has often been investigated in the past as it allows for a convenient monitoring of the outgoing proton flux and the ^{11}C-isotope has a decay time suitable for γ-photon counting.

In figure 3.3 only part of the energy range is covered. With its half life of approx. 19 s the carbon isotope ^{10}C is another important positron emitter next to ^{11}C with a half life of approx. 20 min. For the prediction of PET images which serve in vivo quality control a better knowledge of the ^{10}C cross section is needed to provide sufficiently accurate calculations of activity inside the patient.

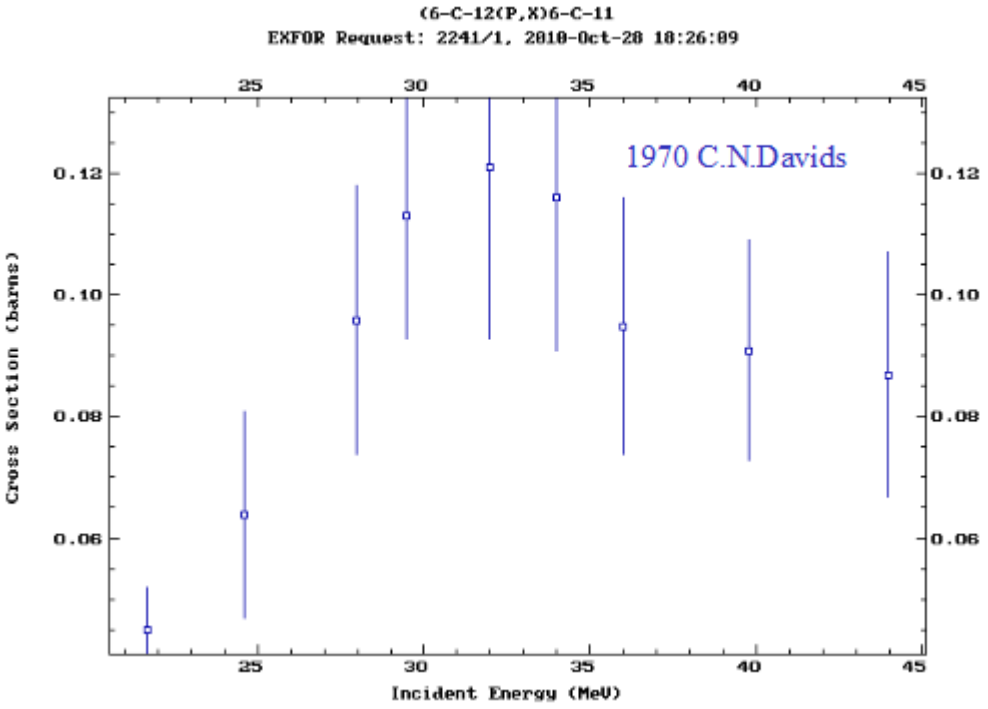

Figure 3.4.: Excitation function for ^{xx}C(p,X)^{11}B. Although the automatic reaction notation produced by EXFOR at the top of the figure indicates the production of ^{11}C, this is obviously a bug and the cross sections do indeed represent the ^{11}B isotope.

The measured data for ^{11}B and ^{10}B shown in figures 3.4 and 3.5, respectively, do not provide sufficient information to determine the excitation functions accurately. The relative errors are higher than the necessary 10% and only three data points are available for the isotope ^{10}B.

However, ^{11}B and ^{10}B are the second and third most frequently created isotopes in the simulation, respectively. And although they might not contribute significantly to the physical dose of proton therapy for their low residual energy, they will still have a significant impact on the reduction of the primary particle flux in the beam.

Moreover, the deexcitation gammas created in the reaction process can be used for prompt gamma imaging - a technique which is currently under investigation by several groups for in vivo verification of beam delivery [KMR02], [MKYK06], [PPC$^+$09]. As mentioned in section 2.5.2, the conformity of the delivered dose to the targeted volume can only be assessed by simulating the treatment and activity measurement via Monte Carlo and comparing the measurement to the prediction. This procedure requires a highly reliable physics simulation.

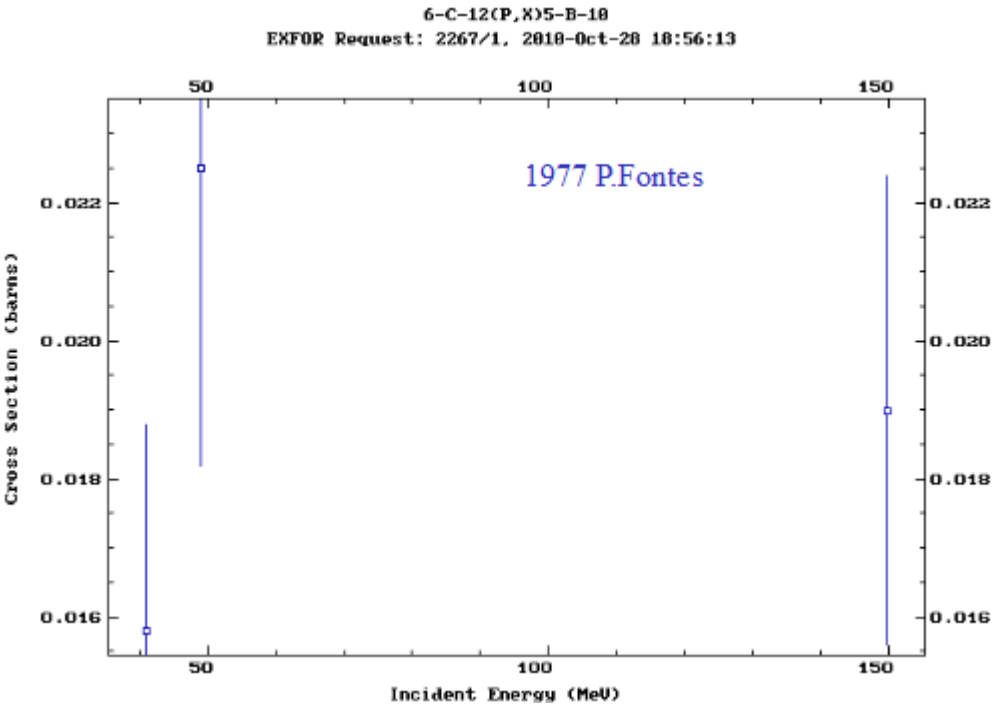

Figure 3.5.: Excitation function for the production of the boron isotope ^{10}B.

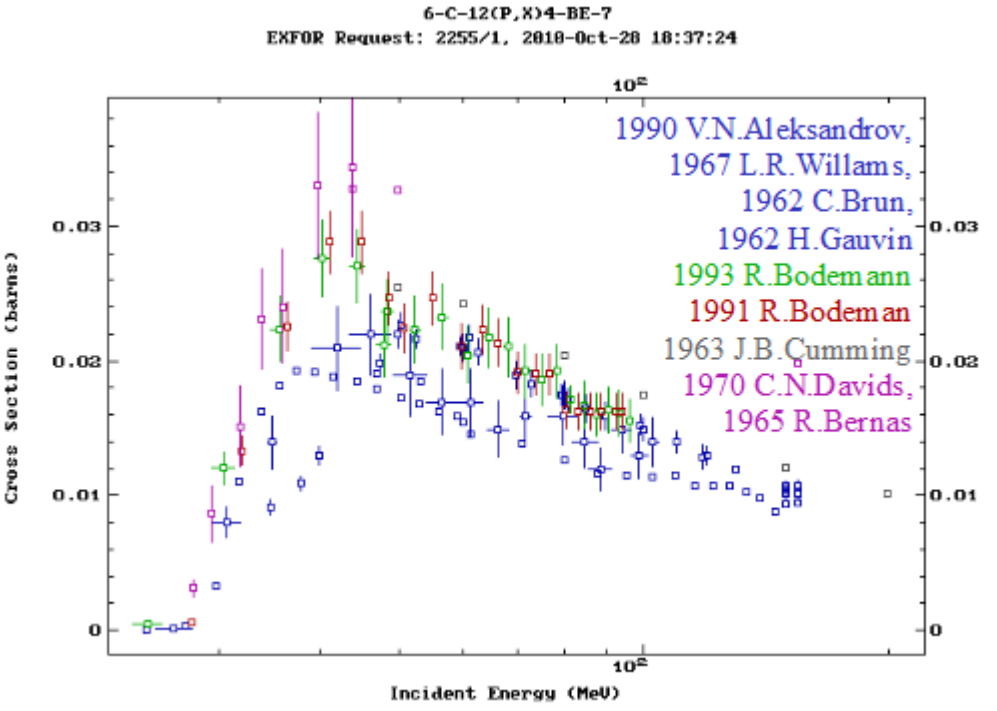

Figure 3.6.: Excitation function for the reaction ^{xx}C(p,X)^{7}Be.

The reaction ^{12}C(p,X)^{7}Be shown in figure 3.6 seems to have been studied as often as ^{12}C(p,X)^{11}C in figure 3.2. However, unlike the data in figure 3.2 the results of different experiments do not agree within 10% of each other for the production of ^{7}Be. With a half life of approx. 53 days this isotope might be used for in vivo treatment verification.

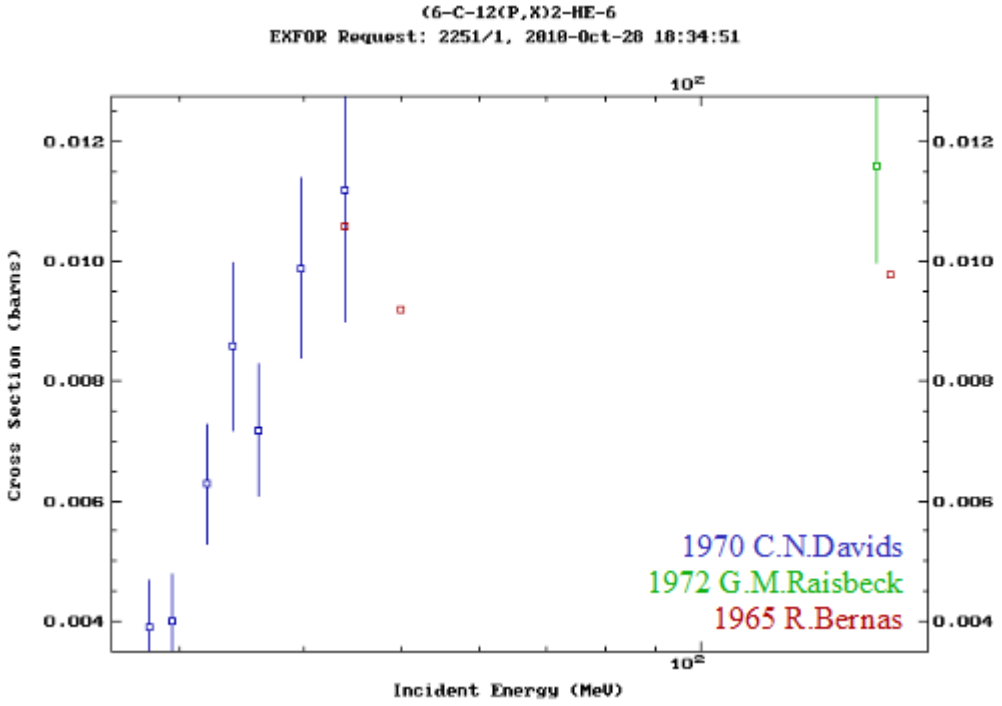

Figure 3.7.: Excitation function for ^{xx}C(p,X)^{6}Li. Although the automatic notation produced by EXFOR at the top of the figure indicates ^{6}He. However, the search has been conducted for ^{6}Li and the search for ^{6}He will produce slightly different results.

The lithium isotope ^{6}Li is a relatively light residual fragment and the reaction channel in which it is produced is the sixth most frequent (see table 3.1). In contrast to the heavy boron isotopes mentioned above, the additional physical dose which ^{6}Li deposits might be substantial. Since it has a relative biological effectiveness different from the one of protons, the contribution to the biological effect on tissue needs to be investigated.

One additional observation which can be made from figures 3.2 to 3.7 is that the majour part of the data has been acquired between 1952 and 1977. With the aid of new technologies, some of which will be described in chapter 4, it is possible to achieve measurements of greatly improved accuracy. Also, in order to provide a more thorough coverage of the relevant isotope production cross section, novel detector concepts need to be developed. The time-of-flight spectrometer introduced in this thesis is one such concept. Its evaluation via Monte Carlo simulation represents the main part of this work.

Oxygen

No data could be found in EXFOR for ^{16}O, ^{14}N, ^{13}C, and ^{10}B. As indicated in table 3.3, ^{16}O is the most frequent nuclear target fragment. The reaction mechanism is inelastic

scattering where the oxygen isotope is left in an excited state. The photon emission which characterises the transfer to the ground state might well be the main source of prompt gamma radiation used for imaging.

^{14}N, ^{13}C, and ^{10}B are also stable nuclear fragments which will contribute little to the physical dose but might have a significant effect on the primary proton flux in the beam and make a contribution to prompt gamma imaging.

The cross sections for ^{15}O, ^{14}O, ^{15}N, ^{13}N, ^{12}C, and ^{11}C are plotted in figures 3.8 to 3.13.

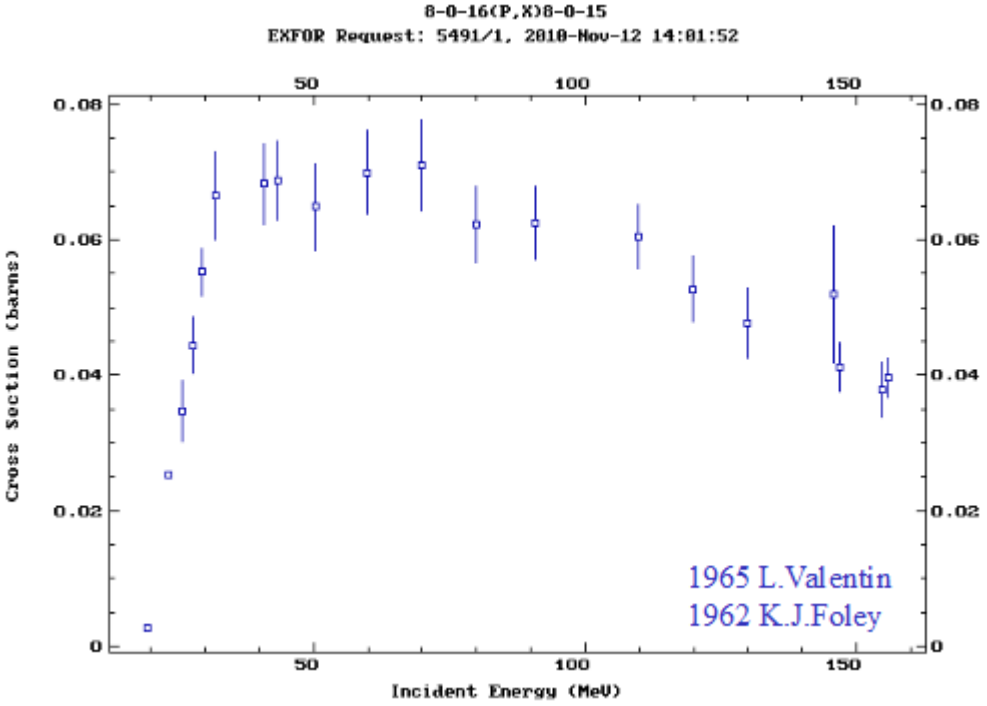

Figure 3.8.: Excitation data for the reaction ^{xx}O(p,X)^{15}O.

From figure 3.8 it is apparent that the production cross section for the isotope ^{15}O has been studied rather well in the 1960s. The energy range is covered sufficiently and most of the relative errors on cross sections are in the proximity of the desired 10% mark. This isotope has a half life of approximately 122 s and is frequently used for PET studies. Igor Pshenichnov [PMG06] has found that the production rate of ^{15}O in a PMMA phantom as predicted by GEANT4 lies within 20% of the measured rate published by Katia Parodi [Par04].

The ^{14}O isotope is another positron emitter with a half life of about 70 s. In figure 3.9 only one data point is provided for its production cross section.

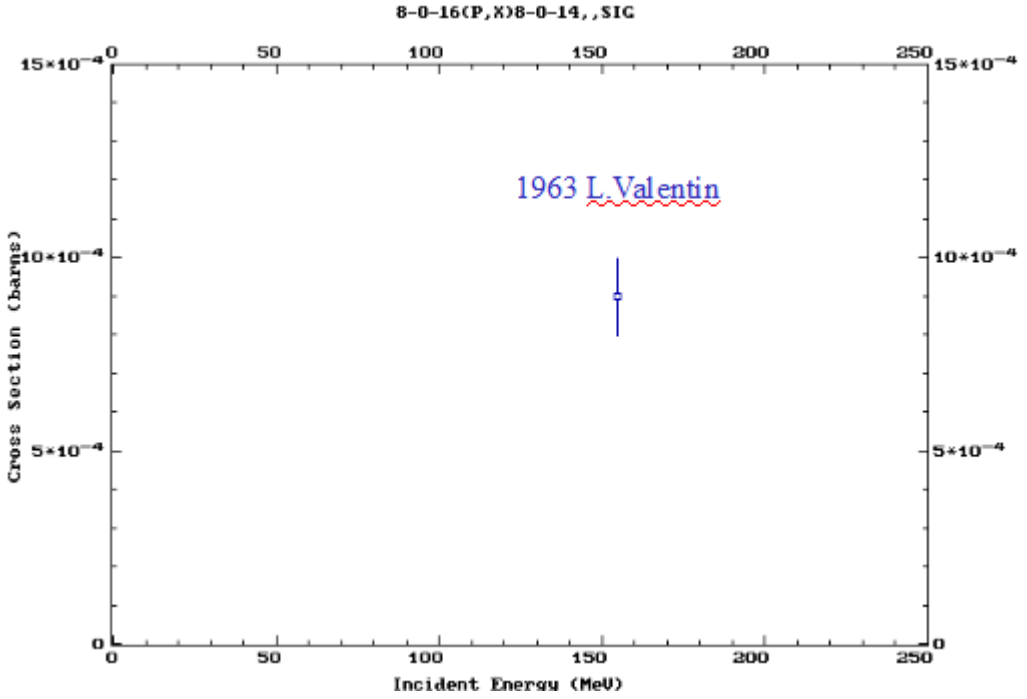

Figure 3.9.: Production cross section of ^{14}O versus projectile energy.

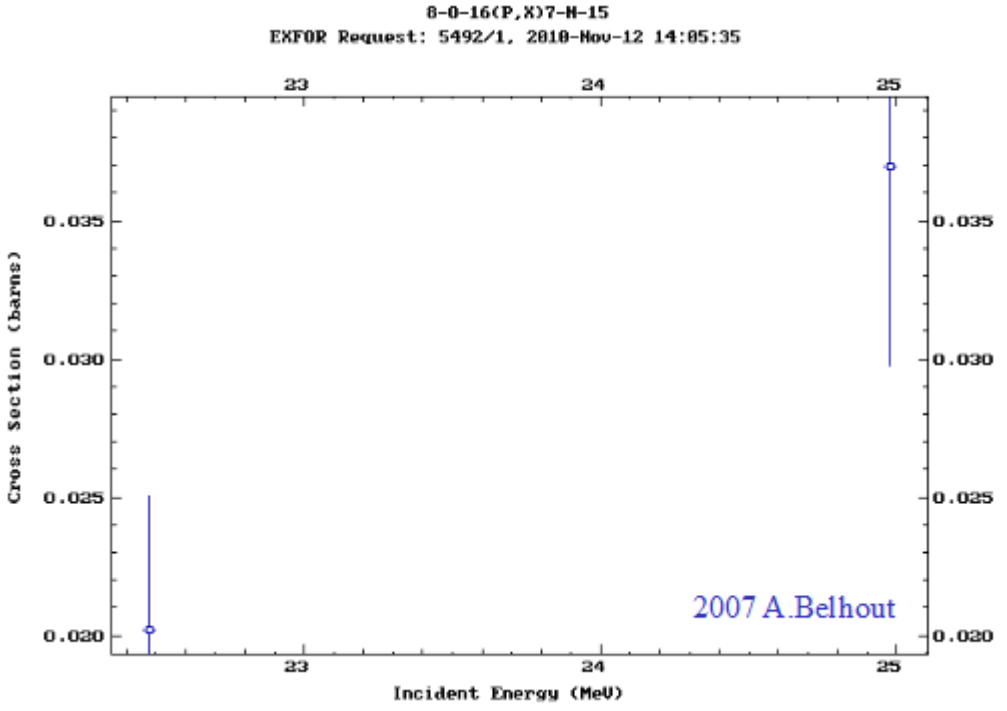

Figure 3.10.: Cross sections for the reaction ^{xx}O(p,X)^{15}N with respect to energy.

The nitrogen isotope ^{15}N is the third most frequent fragment produced by 200 MeV protons in oxygen as indicated in table 3.3. The deexcitation photons emitted in this reaction will therefore contribute significantly to the signal in prompt gamma imaging. Seeing that there are only two data points provided for its production cross section in figure 3.10, new measurements are needed in order to allow for accurate simulations of in vivo monitoring.

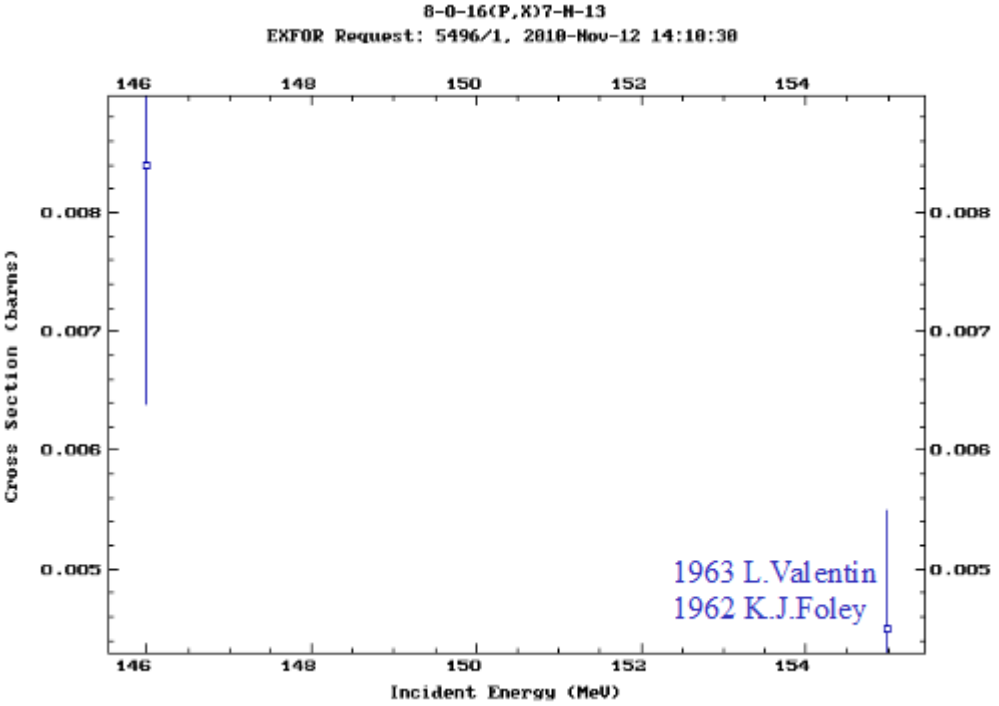

Figure 3.11.: Data for the reaction ^{xx}O(p,X)^{13}N.

^{13}N is another positron emitter commonly used for PET imaging. There are only two data points shown in figure 3.11 and their error bars are several times larger with respect to the limit of 10%.

The stable carbon isotope ^{12}C is also frequently produced in proton irradiations as stated in table 3.3. Accordingly, ^{12}C creation will contribute significantly to the prompt gamma radiation spectrum. Its cross section has been studied comparatively well, as shown in figure 3.12.

The data for the ^{11}C isotope shown in figure 3.13 are very sparse and no error bars are provided. Since this carbon isotope is a frequently produced positron emitter with a half life suitable for in vivo monitoring, its production cross section should be investigated in more detail.

In summary, while the production cross sections of the isotopes ^{15}O and ^{12}C are represented fairly well, the data on ^{14}O, ^{15}N, ^{13}N, and ^{11}C are almost nonexistent. Even though the fabrication of a thin oxygen target might be problematic, additional measurements are required in order to make accurate predictions of dose in the build-up region of the Bragg peak and the activation of positron emitters, the latter being crucial for the comparison with in vivo imaging (e.g. PET).

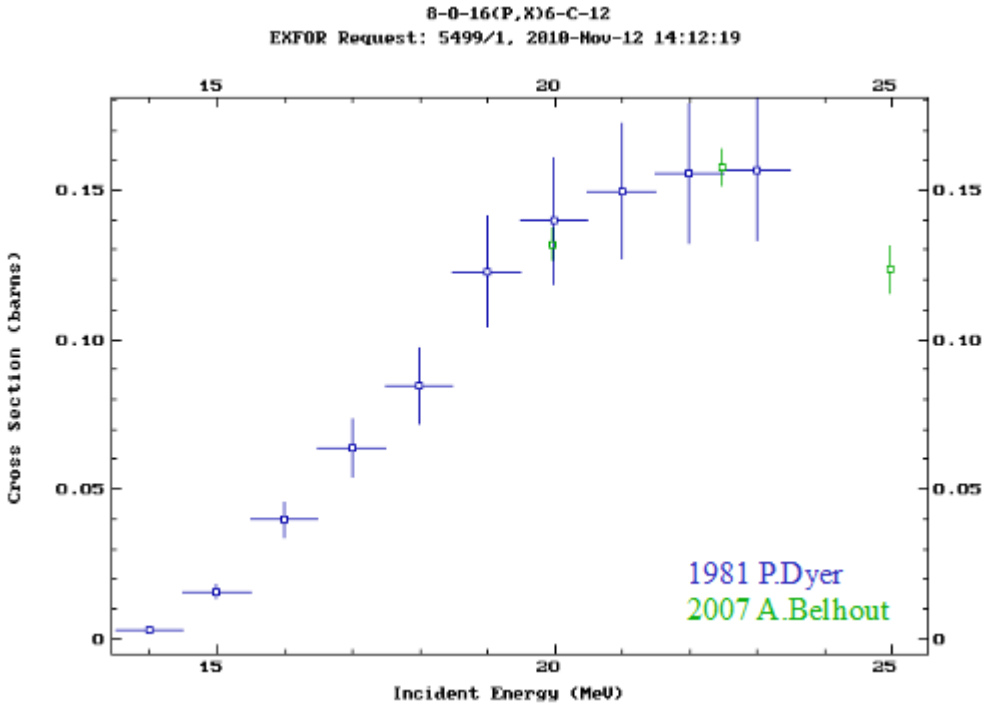

Figure 3.12.: Excitation function for the production of the stable isotope ^{12}C induced by protons in an oxygen target.

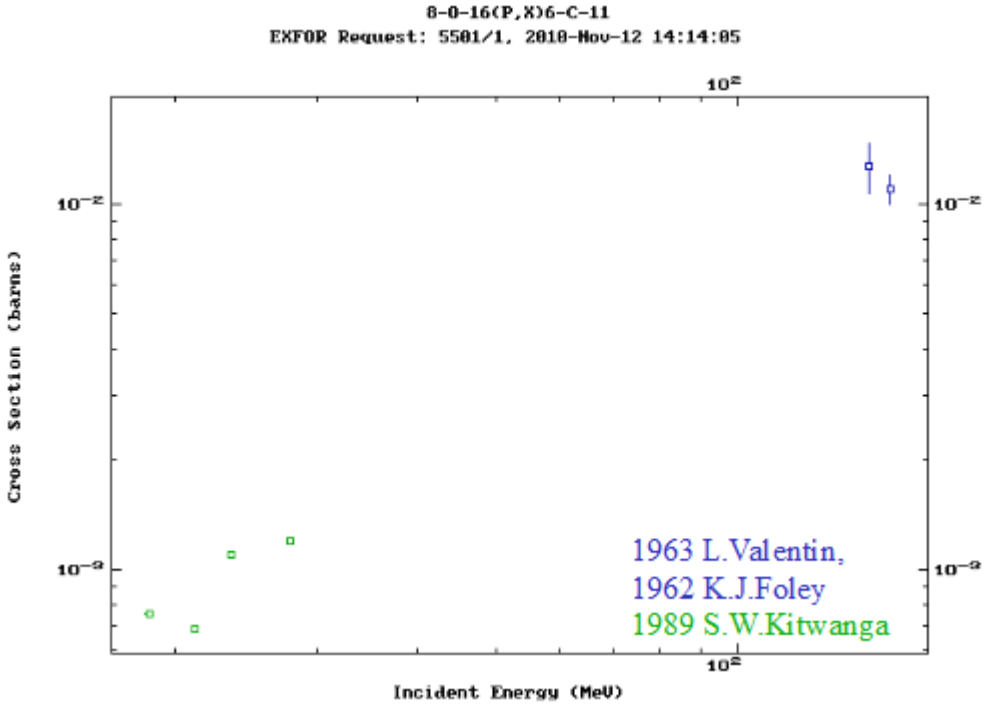

Figure 3.13.: Excitation data for the reaction ^{xx}O(p,X)^{11}C.

3.5. GEANT4 simulation of existing data

The method of validation of GEANT4 nuclear models introduced in this thesis is via the measurement of new accurate cross section data. Another approach is the Monte Carlo simulation of experiments conducted by other groups allowing a direct comparison of the simulation results to the published measurements.

During this study, several attempts at such simulations have been made in parallel to the detector simulation. Because of certain technical details inherent in the experiments it was not possible to carry out detailed simulations which would allow for a proper comparison and meaningful conclusions. As an example, one of these simulations is summarised in this section.

In 1960 T. J. Gooding and H. G. Pugh published experimental cross section results where they focused on the process where the primary proton knocks out a p-state proton from the ^{12}C nucleus [GP60]. The authors' objective was to find out the extent to which this reaction could be described via free scattering of the proton inside the nucleus, the latter seen as a Fermi gas. This paper was chosen for a simulation not only because the target type and beam energy are relevant to particle therapy, but also because it offers a detailed account on the hardware setup, the readout of data and the analysis. At first, the setup of the employed detectors is described below, followed by a summary of the simulation and comparison and discussion of the results.

Experimental setup

The original illustration of the experimental setup can be found in figure 2 of the paper [GP60]. Figure 3.14 shows a replica sketch for quick reference. An unpolarized beam of 153 MeV protons was extracted from the Harwell 2.8 m synchrocyclotron and was focused by magnetic quadrupoles to a 1.3 cm diameter spot at the centre of a vacuum scattering chamber where a thin graphite target was placed. An additional circular collimator with a 2 cm diameter was inserted into the chamber. The angle and direction of protons leaving the carbon target were registered by circular dE/dx-counters subtending solid angles of about 0.01 steradians. These counters were mounted on arms allowing them to be rotated about the target from 15° to 165° on either side of the beam. Thin Mylar windows were integrated into the vacuum chamber in order to minimise the interaction of the secondary fragments.

After the primary beam emerged from the vacuum chamber, it was monitored by being scattered from a 0.083 g/cm^2 polyethylene (PE) target with a second pair of dE/dx-counters placed at 44° on either side of the beam. The energy resolution of the experiment was accessed using the elastic scattering on hydrogen contained in the PE target and was found to be 7 MeV.

The energy balance for the (p,2p') reaction channel investigated in this study is described by:

$$E_0 = E_1 + E_2 + E_R + E_B \tag{3.1}$$

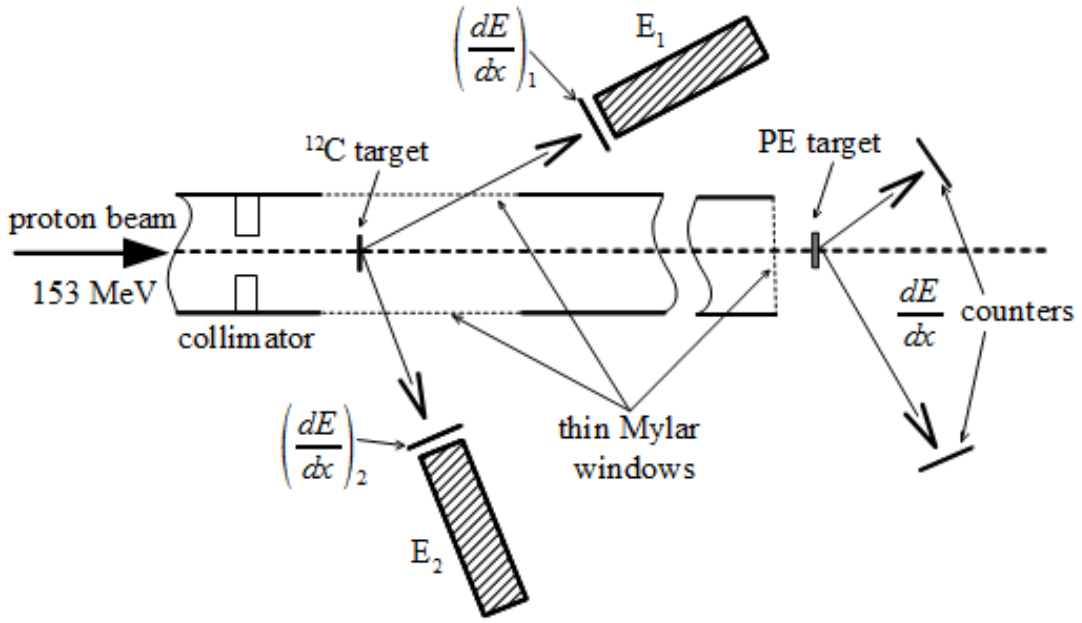

Figure 3.14.: Schematic drawing of the detector setup. The diagram is according to figure 2. in publication [GP60].

where E_0 is the energy of the incident proton, E_1 and E_2 are the kinetic energies of the secondary protons, E_R is the recoil energy of the ^{11}B nucleus and E_B is the binding energy. The binding energy itself can be split into two parts:

$$E_B = Q + E^* \tag{3.2}$$

where the so called Q-value is the energy required for the reaction (see section 2.3), if the residual ^{11}B nucleus is left in ground state, while E^* is the excitation energy of the residual nucleus.

Following estimates are made in the analysis: Q = 15.96 MeV and $E_R \approx 1$ MeV. The recoil energy E_R is not taken into consideration though and the remaining energy of 153 MeV - 16 MeV = 137 MeV is split between the two secondary protons: $E_1 + E_2 = 137 MeV$. This condition is applied to tag those events where the ^{11}B fragment is produced in its ground state, i.e. the proton which was emitted from the target nucleus was in the p-state. Only these events were of interest to the authors of the paper, their objective being the investigation of applicability of quasi-free scattering interpretation at 153 MeV.

A typical spectrum of $(E_1 + E_2)$ for carbon measured with the dE/dx-counters placed at 40° and 30° is shown in figure 4 of reference [GP60]. The p-state data of this spectrum were read off the paper as accurately as possible and are plotted in figures 3.16 and 3.17 together with the simulation results.

GEANT4 simulation

The simple geometrical setup of the simulation is shown in figure 3.15. At this initial stage, the electromagnetic processes were switched off in the Physics List and only elastic and inelastic nuclear processes were registered to protons and neutrons. In fact, this corresponds to the use of thin targets in reality. Since the graphite target was made very thick, nearly all protons underwent a nuclear reaction. At the beginning of such an investigation this procedure helps to save computation time and leads to quick preliminary results. Additionally, the energy spread of 7 MeV FWHM was added to the simulated proton 153 MeV beam, thus emulating the conditions of the experiment.

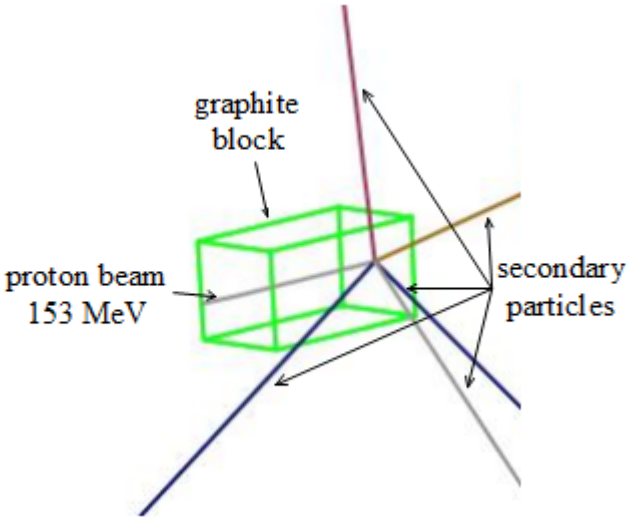

Figure 3.15.: HeppRApp wire frame drawing of the Detector Geometry including the trajectories (tracks) of one nuclear reaction event.

In order to retrieve the necessary data from the simulation, a Stepping Action was added. This user class allows to read out data, such as kinetic energy and momentum direction, at each step during the simulation (see section 2.5.3). Of all inelastic proton events in the simulation only one channel was chosen: ^{12}C(p,2p+γ')^{11}B. At first, unlike the publication [GP60], no according cut was made to exclude all excited states.

Results

Figure 3.16 shows the simulation results along with the p-state data extracted from figure 4 in reference [GP60].

As can be seen in figure 3.16, the simulated spectrum is significantly shifted towards lower energies. This discrepancy appears because the ground state cut has not been applied yet. Thus, a part of the 137 MeV is carried away by secondary particles, mainly deexcitation photons. Table 3.5 shows the energies of the primary proton and secondary particles in one such event.

In an attempt to emulate the ground state cut while keeping all simulated events for the sake of statistics, the simulated spectrum was corrected to include the joint kinetic energy of all secondary particles. This is shown in figure 3.17.

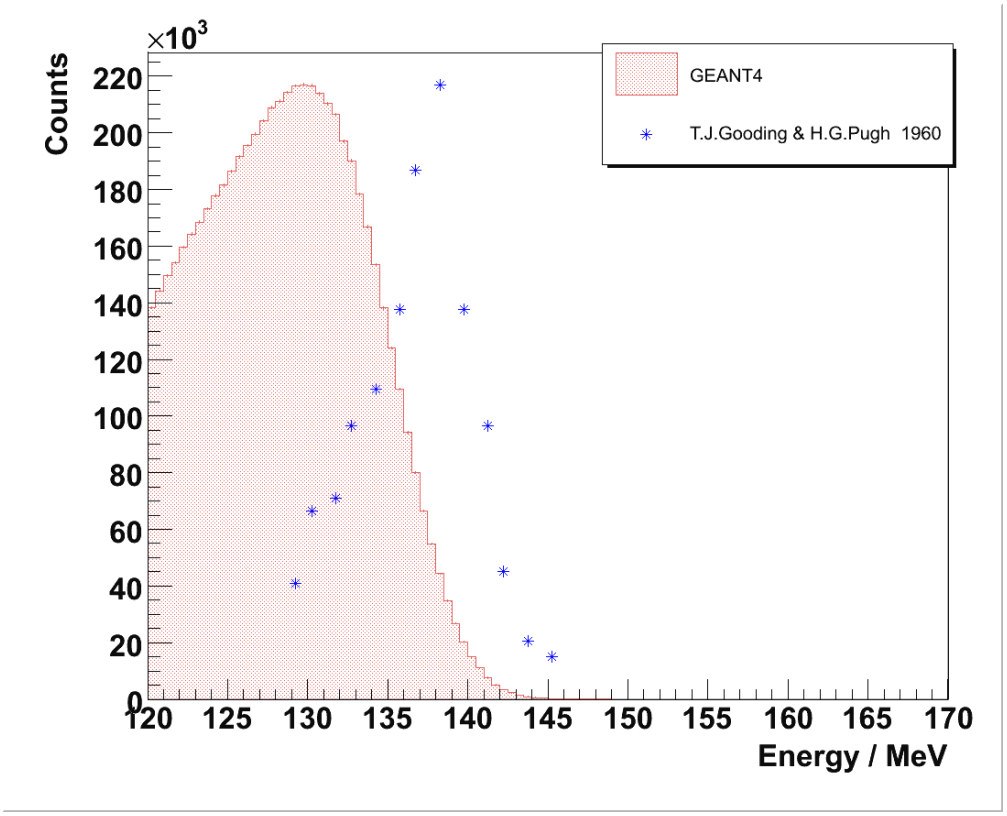

Figure 3.16.: Joint energy of the two secondary protons from ^{12}C(p,2p+γ')^{11}B as simulated in GEANT4 and measured by T. J. Gooding and H. G. Pugh. The cross section measurements are scaled with the maximum value of the GEANT4 simulation. This scaling is for representational purposes only. In order to scale the data properly, the luminosity of the experiment must be known, which has not been stated in the publication.

In the second interpretation of the simulation results (figure 3.17), the maxima are located closer to each other than the 7 MeV energy resolution mentioned above. Considering the simplifications applied to the Detector Geometry and Physics List of the Monte Carlo simulation, the results agree fairly well with each other. However, several aspects of the comparison, such as the higher spread of the simulated spectrum, remain unclear.

In order to yield more significant and to the point conclusions, the simulation has to be more detailed. For one, the electromagnetic processes must be switched on and the target thickness must be set to the originally published value of 0.143 g/cm^2. These settings drastically increase the computation time making an exact simulation difficult at the current stage.

The primary proton rate for the real experiment was 2×10^7 per second allowing for a reasonable event rate in the data acquisition. In the Monte Carlo "computer experiment" biasing techniques need to be applied in future in order to simulate such experiments.

Due to the limited time-frame of this task, no further in depth investigations could be carried out. A more recent paper [CBC$^+$99] based on a PhD thesis [Car95] had been taken into consideration but the investigation had to be aborted for the same reasons as the first one.

Table 3.5.: Kinetic energies of the primary proton and secondary particles in a ^{12}C(p,2p+γ')^{11}B reaction.

particle name	[energy] = MeV
primary proton	154.68334
secondaries:	
proton$_1$	116.33653
proton$_2$	5.2794638
gamma$_1$	2.444171
gamma$_2$	8.1862196
gamma$_3$	2.0851734
gamma$_4$	0.00022606522
^{11}B	4.3934595

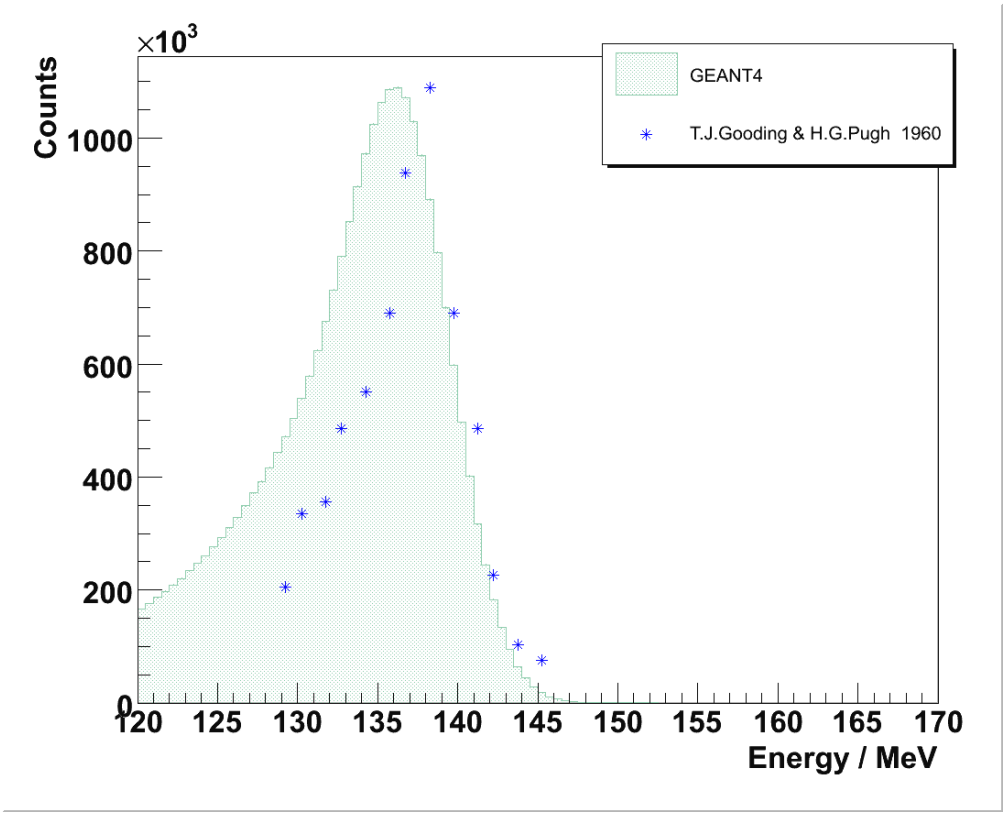

Figure 3.17.: The joint energy of secondary protons, photons and ^{11}B-ions from ^{12}C(p,2p+γ')^{11}B as simulated in GEANT4 and measured by T. J. Gooding and H. G. Pugh. Scaling is achieved in the same way as in figure 3.16.

4. GEANT4 simulation of the tof spectrometer

This chapter describes the GEANT4 simulation of the time-of-flight spectrometer as it has been designed for nuclear cross section measurements by the medical physics group of the 3rd Physics Institute (RWTH Aachen).

At first, an introduction of the spectrometer design and its main parts is given in section 4.1. It was designed and engineered in the context of a diploma thesis by Luc Schlömer [Sch09]. The description of the hardware adds to the general project framework of which the Monte Carlo simulation is an integral part.

Section 4.2 illustrates the geometry of the simulation and gives an idea of its level of detail. An account on the primary beam parameters is provided in section 4.3. The physics processes and models are covered in detail in section 4.4. Since the Physics List of the simulation is the outcome of a rather extensive decision making process, the main corner stones of associated precursory investigations will be included in section 4.4. Such a digression also serves the purpose of motivating and clarifying the resulting configuration. Finally, section 4.5 gives an account on how the necessary data were captured during the simulation. It also introduces the format in which the simulated data were then stored.

4.1. Detector concept and hardware design

In the energy range typical for proton therapy the velocity of target fragments is relatively low compared to the speed of light. Thus, time-of-flight techniques can be used for their identification. In order to distinguish between all charged isotopes without ambiguity their energy loss per unit path length, dE/dx, must be measured as well.

Here, the conceptual design of the time-of-flight spectrometer is presented first. In addition, most relevant features of the hardware are outlined providing the rationale for their use. Further information and detailed illustrations can be found in the diploma thesis by Luc Schlömer [Sch09].

A schematic outline of the detector setup is shown in figure 4.1. The time-of-flight measurement is initiated by the primary protons hitting the Start scintillator. The latter is placed in front of the target along the beam because it would otherwise have a high impact on the momentum of the target fragments. Since the Start is a plastic scintillator mainly composed of carbon and hydrogen, the primary protons will induce a substantial amount of nuclear reactions in it.

As a consequence of simulation results presented further in section 5.5.1, the Start detector was placed even further "upstream" - in front of the two Veto detectors with

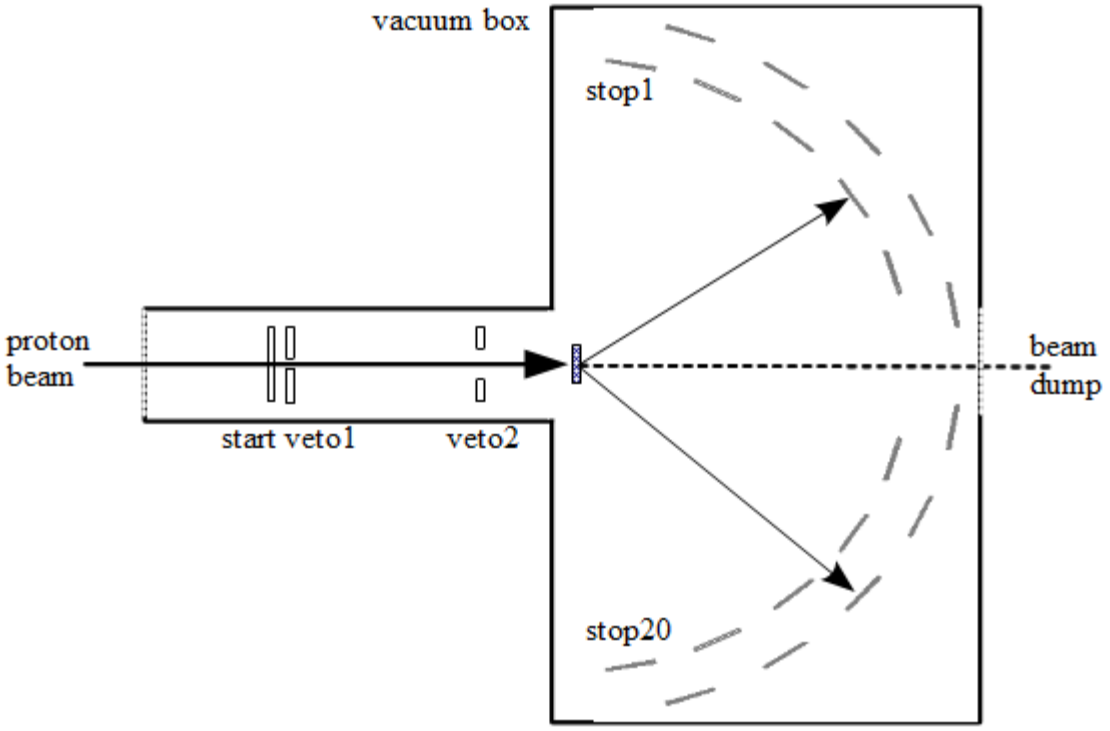

Figure 4.1.: New concept for the time-of-flight spectrometer. The beam enters from the left and hits the Start detector which triggers the time-of-flight measurement. After the beam hits the target, the secondary particles from nuclear reactions travel towards the Stop detectors. The latter stop the time-of-flight measurement and accumulate the energy deposited by the particles.

their size and position matched to eliminate the associated background.

The time-of-flight measurement can be stopped by a secondary particle hitting one of the 20 Stop scintillators. The in-plane angle covered by these detectors spans approximately 160° to facilitate the detection of heavier target fragments with their wide scattering characteristics. In principle, the optimal coverage is achieved by a 2π solid angle detector allowing for the detection of all charged particles in the output channel. A more cost efficient way is the coverage of the scattering angle in one chosen plane followed by an extrapolation assuming that the scattering characteristic is symmetrical with respect to the beam axis.

The use of 20 Stop scintillators implies that there can be 20 concurrent time-of-flight recordings which receive the same gate from the Start while their Stop signals are generated individually by impinging particles. The simultaneous use of several Stop detectors offers the additional potential of identifying coincidences of secondary particles from nuclear reactions. With an effective size of 100 mm × 212 mm × 5 mm, each, the Stop detectors cover approximately 12% of the 2π solid angle. In addition, as a consequence of mechanical constraints of the CNC machine used for manufacturing, the flight distances in the spectrometer can span a maximum of 800 mm. This way, the flanges of the 100 mm wide Stop scintillators cannot be aligned side by side and have to be staggered at two consecutive distances: 700 mm and 800 mm.

All scintillation detectors, i.e. Start, Stops, and Vetos were machined from the same

Bicron® BC420 plastic scintillator material. The Start and Veto detectors are machined to fit into the vacuum tube which precedes the detector chamber in figure 4.1.

In fact, all detector parts are placed into two consecutive vacuum chambers separated only by a vacuum gate valve. The tube which holds the Start and Veto detectors is attached to the beam extraction pipe with only a thin metal foil separating the vacuum volumes. The vacuum is necessary in order to minimise the impact on the momentum of the target fragments. The latter are very slow and would otherwise deposit all their energy along the first few cm in air at normal pressure.

The use of vacuum is another reason why 20 Stop scintillators are employed instead of one rotating arm. Double differential cross sections need to be measured, so that a wide angular range has to be covered by the detector in one plane. Rotating one Stop scintillator inside the vacuum chamber would involve the use of complex and cost ineffective vacuum parts. The simultaneous coverage of 20 angle intervals also allows to save valuable beam time.

Since, at a vacuum of less than 1 mbar, significant deformations of the chamber can be expected, counteractive measures have been applied: the chamber is made of 10 mm thick aluminium panels, and an inner grid of item® rails has been added for support. Special care was taken to avoid the deformation of the top panel of the chamber, since the Stop detectors are rigidly connected to it. It was assembled from two smaller panels of 20 mm thickness with their outer edges supported by item® rails. Figure 4.2 shows a view of the detector assembled at the Jessica beam site of the COSY synchrotron in Jülich.

The light produced inside the scintillators is detected by silicon photomultipliers (SiPM), which are novel semiconductor photodetectors. Up to several thousands of small (≈20-30 μm) avalanche photo diodes (SAPD) are arranged on a common substrate and operated in so-called limited Geiger mode. The latter is an avalanche process with negative feedback, i.e. the discharge is quenched by limiting the current to about 10 μA with a small polysilicon resistor in each pixel. Although the pixels operate independently from each other, they are connected to the same readout line and form one combined output signal which is a measure of the light flux [BDI+01], [DBB+06], [BDF+06] and [CCCR07].

In comparison to conventional photomultiplier tubes SiPMs offer a number of advantages:

- Silicon photomultipliers are especially suited for time-of-flight measurements due to their fast response which, in turn, is possible because of the very thin depletion layer and the extremely short duration of the Geiger discharge development.
- Like other silicon-based photodetectors, SiPMs have a quantum efficiency of almost 100%. Degraded by some additional contributions like the geometrical efficiency, the probability of a photoelectron to initiate a Geiger discharge and the recovery time of the pixel, the overall photon detection efficiency (PDE) is better than that of a traditional PMT.
- There is no need for high voltage supply since SiPMs are operated with a relatively low bias voltage (25-75 V).

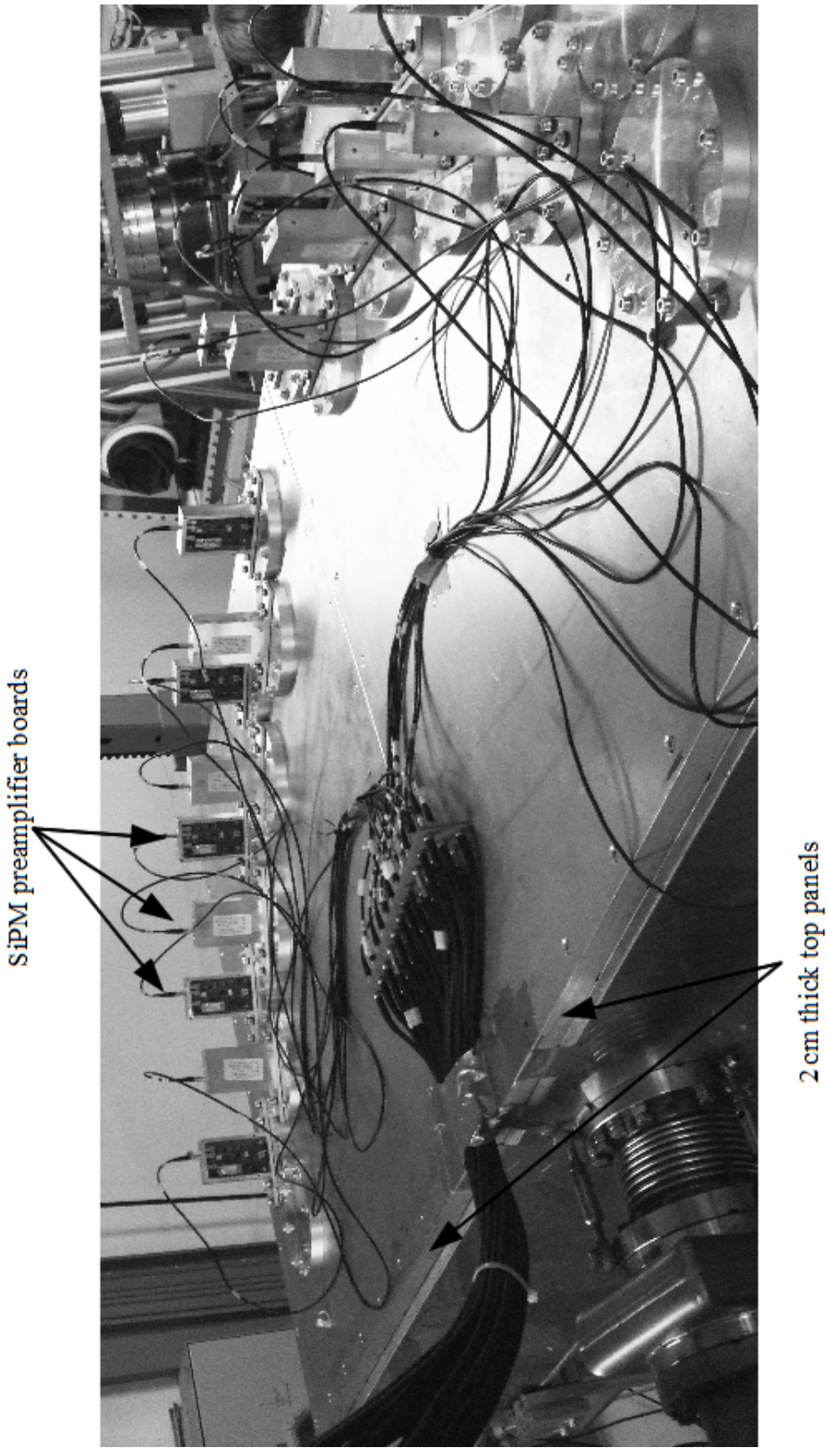

Figure 4.2.: View of the assembled time-of-flight spectrometer. The photograph was taken standing next to the beam pipe. The beam extraction as well as the Start and the Veto detectors are on the left and out of view on this picture. The SiPM preamplifiers indicated by arrows are mounted on top of the flanges of the Stop scintillators which are inside the chamber.

- SiPMs can be acquired at a lower price.
- Since the signal parameters of silicon photomultipliers are not influenced by magnetic fields, they will be preferred to traditional photomultiplier tubes in proximity to accelerator beam optics.

The detection behaviour and time and energy resolution of the Stop scintillators in combination with 3 mm × 3 mm Hamamatsu SiPMs have been investigated by Luc Schlömer [Sch09], Christian Salmagne [Sal09] and Paul Fiedler [Fie09]. Although the time resolution of the system proved to be acceptable, the energy resolution has shown a strong dependence of the SiPM signal with respect to the position of excitation of the scintillator. Therefore, the Stop scintillators, as well as the Start detector, have each been equipped with two additional fibre-optic light guides. The latter are glued into grooves milled into the side surfaces of the scintillators and their light is detected by 1 mm × 1 mm SiPMs.

The initial measurements were carried out with graphite targets supplied by GOODFELLOW with a 99.8% purity and in varying thickness: 1 mm, 0.35 mm, and 0.075 mm.

4.2. Detector Construction

As indicated in section 2.5.3, the Detector Construction completely describes the geometry and other properties of space in which the particles will be propagated. In this section, the properties are divided into two groups: materials and volumes. While the first paragraph describes the element composition of particular objects in the simulation, the paragraph on volumes deals with geometrical shapes and their positioning. Figure 4.3 shows a wire frame plot of the geometry.

Materials

The material of the detector chamber was simulated by using the exact composition values of an aluminium alloy, its main constituents being Al:91%, Cu:3.95%, and Mg:1.1%. The graphite target consisted mainly of ^{12}C with a small (1.11%) incorporation of ^{13}C and the density was set to 1.7 g/cm^3, accodring to NIST PSTAR.

The scintillator material is based on polyvinyl toluene with a density of 1.032 g/cm^3. It was implemented according to the data sheet provided by Saint-Gobain [Sai05] and comprises hydrogen and carbon atoms in a ratio of 11/10.

The vacuum inside and outside the chamber was mimicked by simulating the material composition of air [1] with its density reduced by a given factor. For example, a factor of 1/1000 approximates a pressure of 1 mbar.

[1] Air, dry (near sea level), NIST PSTAR

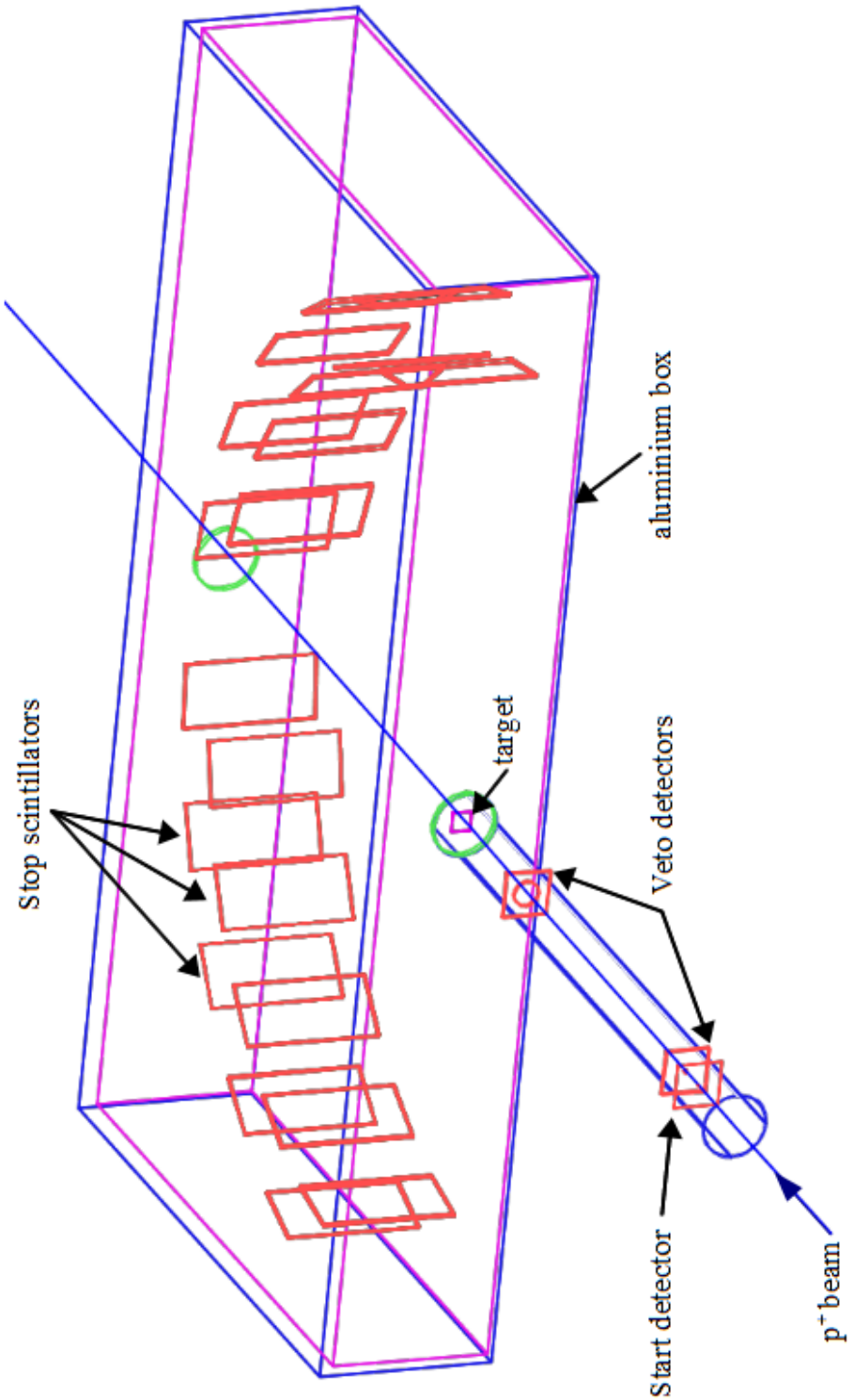

Figure 4.3.: Wireframe drawing of the simulation created with HepRApp browser. The world volume is invisible. One single primary proton trajectory runs through the detector and leaves towards the beam dump on its opposite side.

Volumes

In principle, the Detector Construction of this simulation is a grouping of different solids, such as boxes and tubes, which are inserted either directly into the world volume or other existing volumes.

Since the primary focus of this thesis is on the feasibility of inelastic cross section measurements with the time-of-flight spectrometer, noncritical geometrical parts and details, e.g. vacuum flanges, have not been included in the simulation.

Care was taken to account for the unequal thicknesses of the top (2 cm) and bottom (1 cm) vacuum chamber panels: first, an aluminium filled box was constructed and afterwards an air filled box was placed inside the first one, with a relative downward shift of 1 cm. The asymmetrical vertical position of the Stop detectors is implemented in a similar way.

4.3. Primary Generator Action

The primary proton beam is generated about 0.5 m before the entrance to the tube which holds the Start and Veto detectors. According to the operators of the COSY accelerator, the beam delivered by the synchrotron is monoenergetic. Thus, all primary protons are created with an initial kinetic energy of 200 MeV in the simulation, as well.

The lateral resolution of the beam is simplistically modelled by a symmetric gaussian shape with an FWHM of 2 mm which is in the same order of magnitude as the published beam profile [KD03] measured inside the accelerator. Although the first detector commissioning tests were carried out with a much wider beam (FWHM≈6 cm) for the lack of additional quadrupoles, the beam will be focused to this scale for the actual data acquisition.

4.4. Physics List

When protons of 50-250 MeV energy interact with a carbon target, there is a multitude of secondary particles created through electromagnetic and nuclear interactions. The Physics List of the detector simulation must not only define all of these particles, but also assign proper electromagnetic, nuclear and weak processes to each particle. In addition, appropriate models have to be chosen carefully and registered to each process. Where necessary, several models have to be combined to cover the energy range of the simulation. The right choice of models depends heavily on the physics studied. The user must also define certain production cuts for the particles which represent a tradeoff between the precision of the simulation and its computation time.

In order to determine the optimal physics configuration for this study, some preliminary investigations have been carried out. The results have been compared with those found in literature, all of which are summarised in section 4.4.1. The resulting Physics List configuration and its main parts are then described in section 4.4.2.

4.4.1. Search for the optimal configuration

The approach chosen in this study is to adapt the physics list from an application supplied with the GEANT4 package. The implementation is contained in the advanced example "hadrontherapy" developed by Pablo Cirrone and colleagues at the CATANA proton treatment centre in Italy [CCG+05], [CCL+04]. They implemented a beam line used for treatment of choroidal and iris melanomas with 62 MeV protons. The great advantage of this Physics List is that it is modular, i.e. a choice of models is implemented for different processes and the user can switch between these within a macro file. Thus, there is no need to make frequent changes to the C++ code and to recompile it each time the physics configuration has been changed. The physics options can easily be compared with each other and an appropriate choice can be made which fits existing experimental data the most.

Simple test simulation

In its initial stage, the simulation had a very simple geometry consisting of a world volume, a 20 mm thick graphite target, and an air filled detector with a sensitive surface, as shown in figure 4.4. Particle Filters were assigned to a so-called Multifunctional Detector which in turn was assigned to the detector volume so that detector hits effected by different particles could be accumulated separately at the end of a Run (see section2.5.3). After the Physics List was imported from the hadrontherapy example into the detector simulation, a comparison was made between the inelastic hadronic process options implemented in it. At this stage, the GEANT4 version 4.9.0 patch 01 was used.

Diagrams 4.5(a) and 4.5(b) show the rates of target fragments for three inelastic nucleon-nucleus interaction models for protons and neutrons: binary cascade, Bertini cascade, and the precompound model. Since the precompound model is only valid up to 170 MeV, it has been teamed with the binary cascade to account for particles of higher energies. All electromagnetic and weak processes have been switched off in these simulations in order to obtain a high rate in the detector and to speed up the computation. For each model, 10^8 primary proton events[2] have been simulated with ten different seeds and the mean value for the number of detected particles has been chosen for each seed.

Figures 4.5(a) and 4.5(b) show very high discrepancies between the Bertini model and the other two models, especially in the production of isotopes ^{11}C, ^{10}C and ^{9}B. Incidentally, the latter isotope is highly unstable and should not appear in the simulation at all. The difference in rate between the models might be due to the fact that the Bertini model is based on the necessary condition

$$\lambda_B / v << \tau_c << \Delta t \tag{4.1}$$

where λ_B is the de Broglie wavelength of the nucleons, v is the average relative velocity between two nucleons and Δt is the time interval between collisions. According to the Physics Reference Manual [Phy08], "this condition is no longer strictly valid be-

[2]Here, the meaning of "primary proton event" is the same one inherent in the class G4Event (see section 2.5.3).

low 200 MeV" whereas in the above simulations the primary protons had an energy of 180 MeV.

In contrast, for the binary cascade model data plots are provided for 113 MeV protons in the Physics Reference Manual where the model compares well with experimental data at low energies. The precompound model is actually a low energy extension of the hadron kinetic model and can be expected to perform well at 170 MeV and below. In conclusion, the Bertini cascade should rather not be embedded into a physics list with energies of 250 MeV and lower.

Overall, the lack of a concrete recommendation for a physics list in ion therapy represents the main obstacle for a high dissemination of GEANT4 in the medical field. The scope of duties of a medical physicist is usually far away from the computing tools and users are left confused by the manifold of possible model solutions, not knowing which one will most precisely meet their needs.

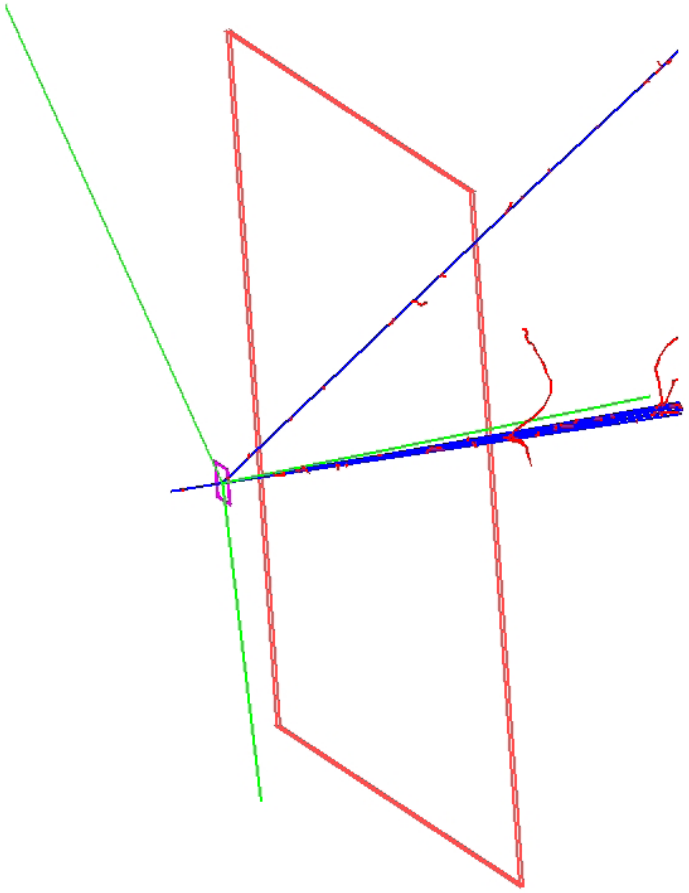

Figure 4.4.: From left to right: 10 primary protons hit the 20 mm graphite foil target depicted in magenta and pass through the air filled sensitive detector surface (red). Different trajectory colors denominate different signs of charge: trajectories of positively charged particles are drawn in blue color, negatively charged in red and neutral particle trajectories are plotted in green.

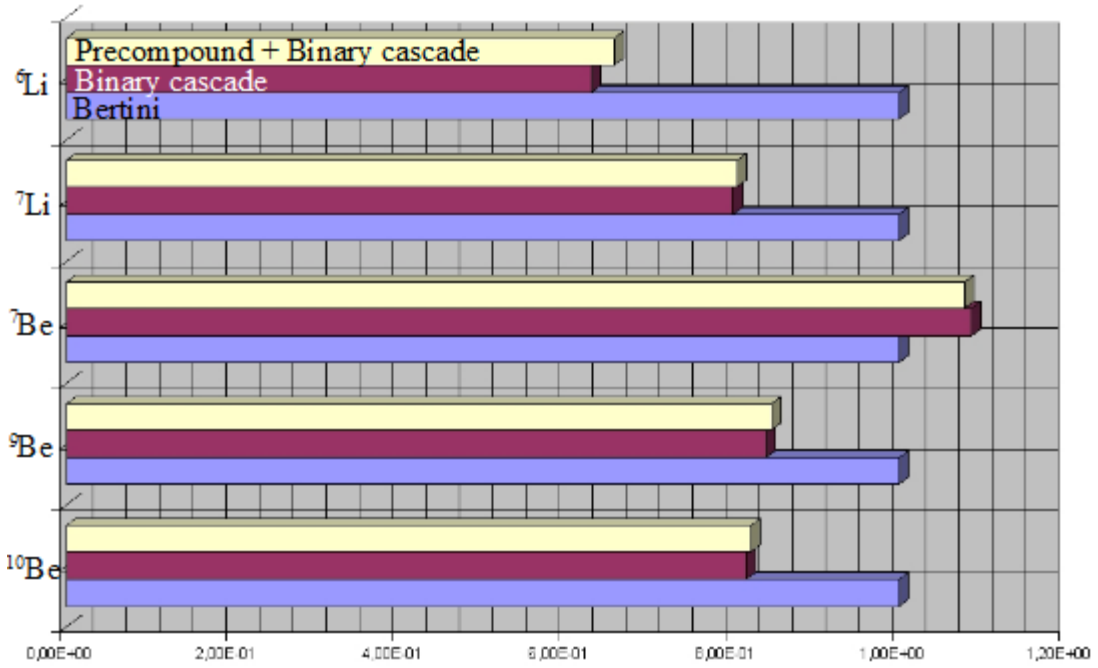

(a)

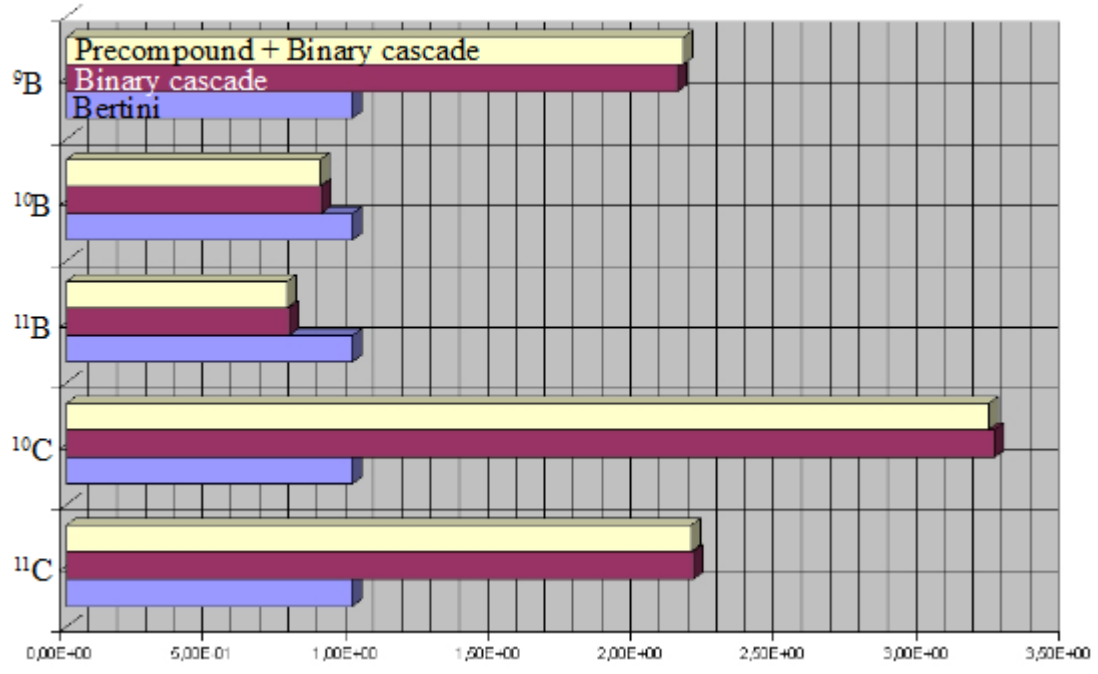

(b)

Figure 4.5.: Rates of ions impinging on the detector in figure 4.4. The fragments were produced in inelastic nuclear interactions of 180 MeV protons with the graphite target by the Bertini model [blue], the binary cascade [red] and the precompound model with default evaporation mechanism [yellow]. All values are normalised relative to the corresponding Bertini model result.

Recommendations found in literature

In the past, the only attempts to provide a recommendation have been presented by Harald Paganetti and colleagues [PG03], [JP08]. Using a multilayer Faraday cup they measured the projected range distribution of charged nuclear secondaries from 160 MeV protons stopping in polyethylene. Since the signal in the build up region of the Bragg curve is primarily due to nuclear reactions and the signal within the peak is due to electromagnetic processes, the influence of the corresponding models can easily be distinguished in such a multilayer measurement. With reference to inelastic nuclear scattering, the authors found that the binary cascade provides the highest accuracy in modelling the empirical data. The low energy parametrised models G4LEProtonInelastic and G4LENeutronInelastic strongly overpredict the charge in the build up region and the Bertini cascade slightly underpredicts the charge at the beginning of the build up and overpredicts it shortly before the Bragg peak. Electromagnetic processes seem to be modelled best by the standard electromagnetic model (SEM) [JP08].

The elastic models were tested by simulating neutron energy distributions at varying depths of a homogeneous water phantom which was irradiated by a 10 cm $\times$ 10 cm field of 100 MeV protons. The combination of the G4UHadronElasticProcess with the G4HadronElastic model yielded most accurate results, while the other models showed a discontinuity at 32 MeV. The relatively small trade-off here is the inability of the G4UHadronElasticProcess and G4HadronElastic model to reproduce the measured charge tail behind the Bragg peak. Based on these published results the recommended models and processes have been included in the detector simulation in this study.

Having taken care of the intra-nuclear cascade and preequilibrium deexcitation mechanisms, the equilibrium de-excitation model remains a matter of discussion. While Pshenichnov et al. [PLMG07] and Quesada [Que09] recommend to use the Fermi breakup (FBU) for light systems like $p^+ \rightarrow {}^{12}C$, Jarlskog and Paganetti employed the Weisskopf-Ewin evaporation model (WEEM) [JP08]. These models allow the compound nucleus to further de-excite making sure that unstable fragments, like ^{8}Be can breakup into stable secondaries, like $2\times\alpha$. The Fermi breakup model can predict the final states in the output channel as a result of an excited nucleus with atomic number $A < 17$. The WEEM is an evaporation model which can account for the ejection of light fragments with $Z_{ejectile} < 3$ and $A_{ejectile} < 29$.

Comparison of deexcitation models in detector simulation

In order to assert the impact of the choice of equilibrium model on the detector simulation, the count rates of secondary fragments have been compared using the binary cascade and precompound model in connection with, in turn, the Fermi breakup, the default evaporation model, and the generalized evaporation model (GEM). The latter aids the evaporation of particles with $2 < Z_{ejectile} < 13$ and $4 < A_{ejectile} < 29$.

The count rates produced on the 20 Stop scintillators have been recorded and evaluated in two groups: stable ions with half lives > 1 ns and unstable ions with very short life times ($\ll 1$ ns). The latter should not be able to travel a distance of 700 mm or more within their life time and should therefore not be registered by the detector. The half lives of isotopes considered stable can be read from figure 4.6. Figures 4.7 and

4.8 show the results for stable and unstable isotopes, respectively. As an additional check, the Fermi breakup has been combined in turn with the default evaporation and the generalised evaporation model. The results can be found in figure 4.9.

There seems to be a considerable occurrence of the ^{8}Be and ^{9}B isotopes with all models and combinations thereof. This aberration is currently not understood. Other than that, the count of unstable particles on the Stop detectors is fairly small and can be neglected. The combination of the binary cascade along with the precompound model and Fermi breakup will be used throughout all of the following simulation processes.

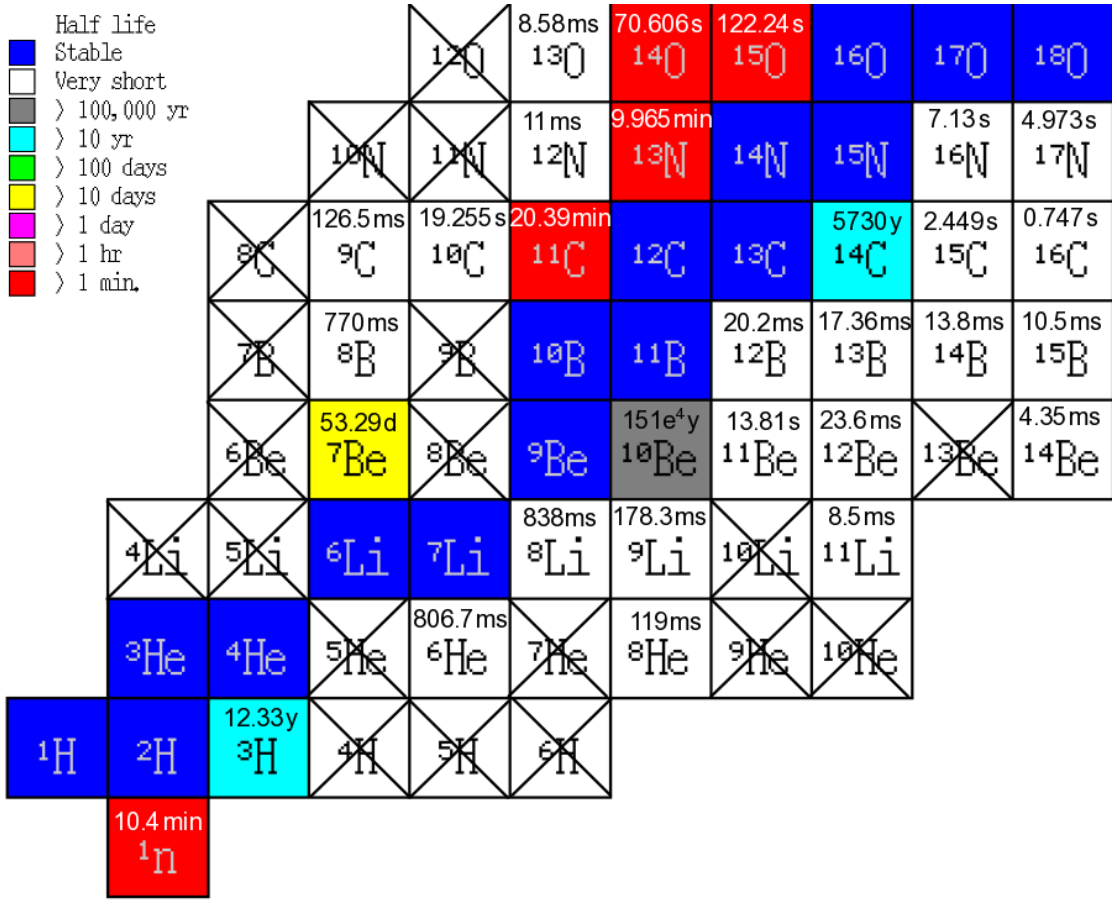

Figure 4.6.: Excerpt from the table of nuclides [Nuc]: the isotopes with half lives several orders of magnitude less than a nanosecond are crossed and the half lives for all other unstable isotopes are supplemented.

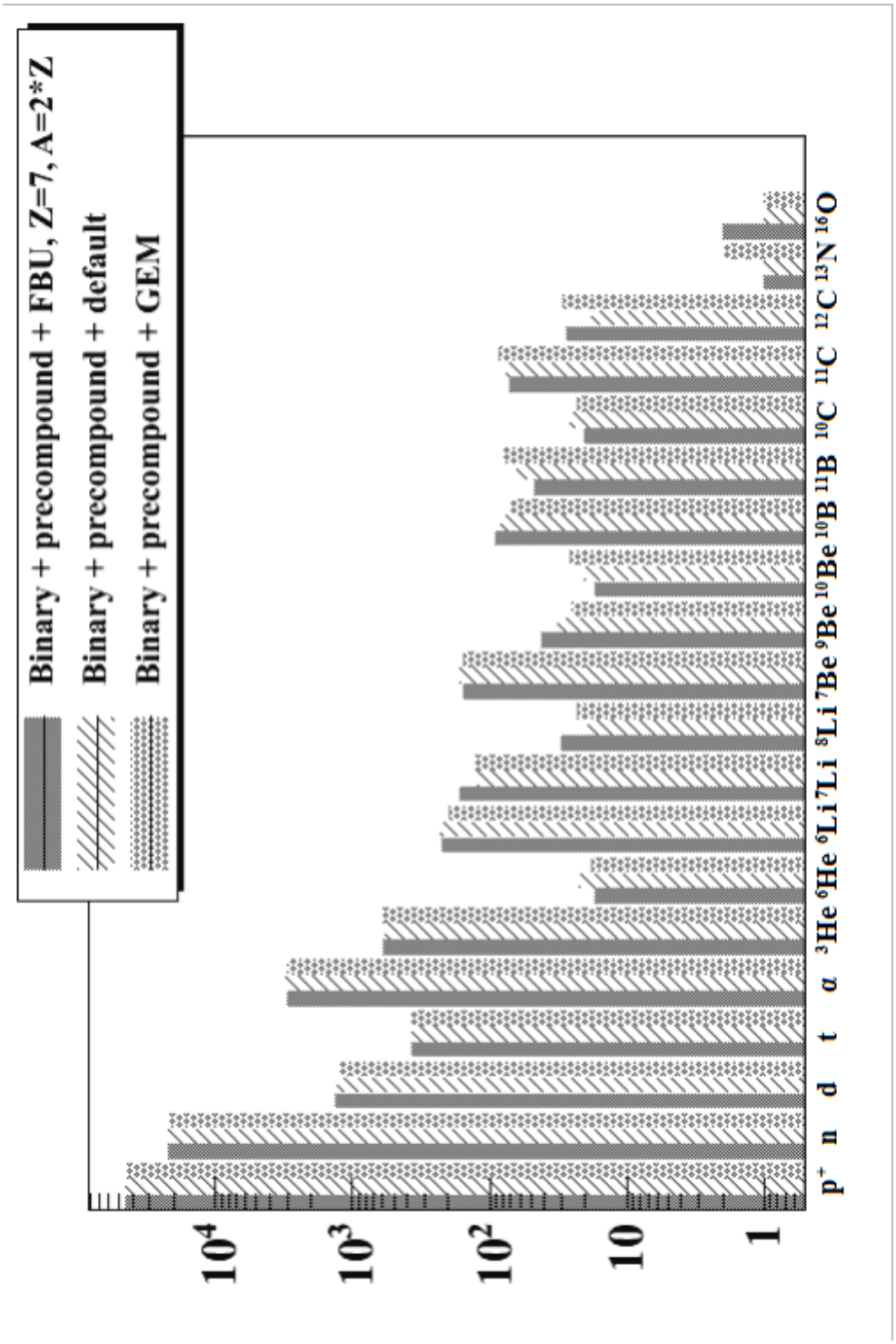

Figure 4.7.: Stable isotopes from figure 4.6. The different bar fill styles correspond to simulations with the binary cascade and the precompound model combined in turn with the Fermi breakup (FBU), with the default evaporation model, and with the generalized evaporation model (GEM). Provided a pressure of 0.1 mbar in the detector chamber, ^{16}O and ^{13}N are (by orders of magnitude) the most frequent isotopes produced from the rest gas.

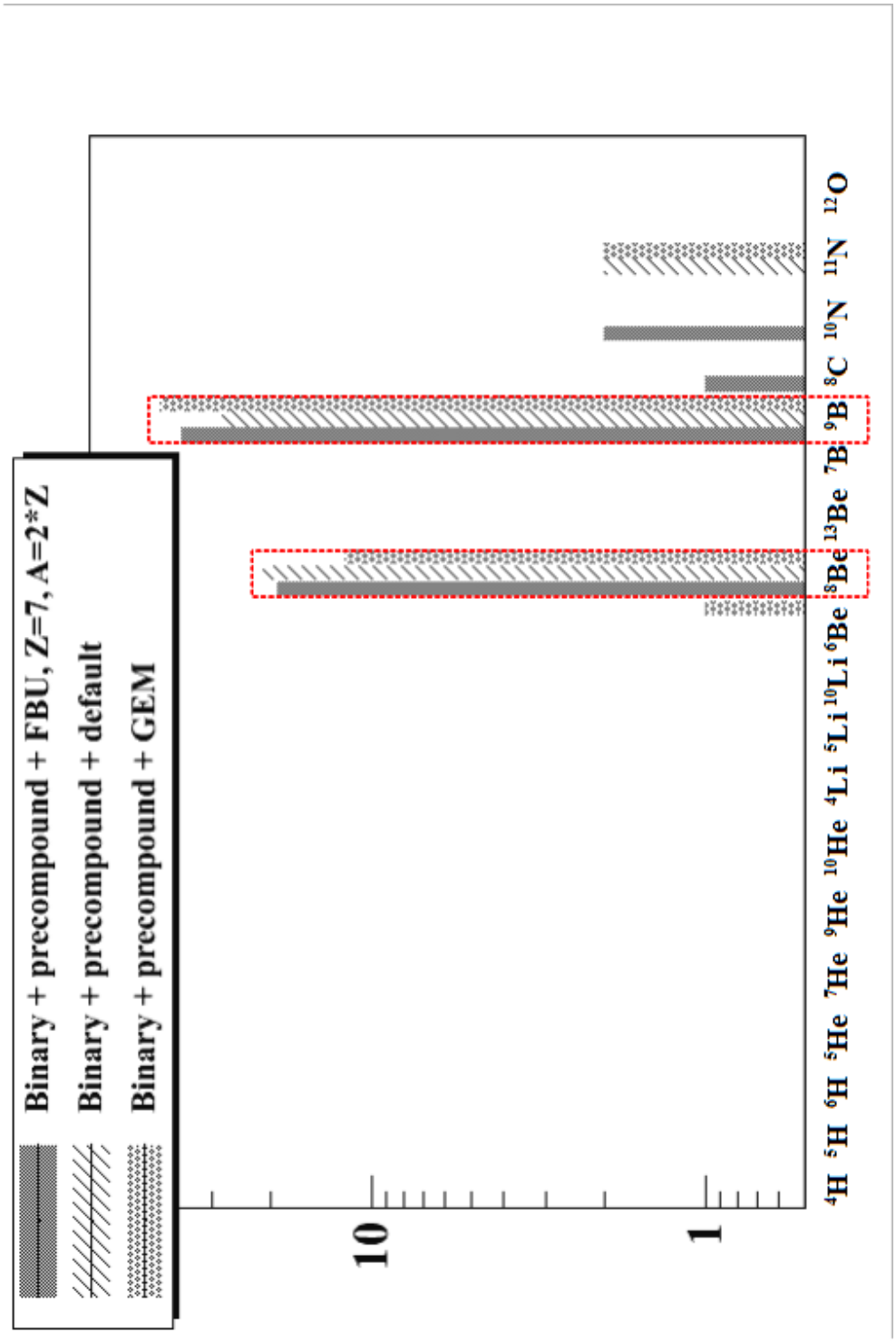

Figure 4.8.: Production rates of highly unstable isotopes from figure 4.6 (crossed). In contrast to figure 4.7 these results were obtained from a ten times as large a number of primary protons.

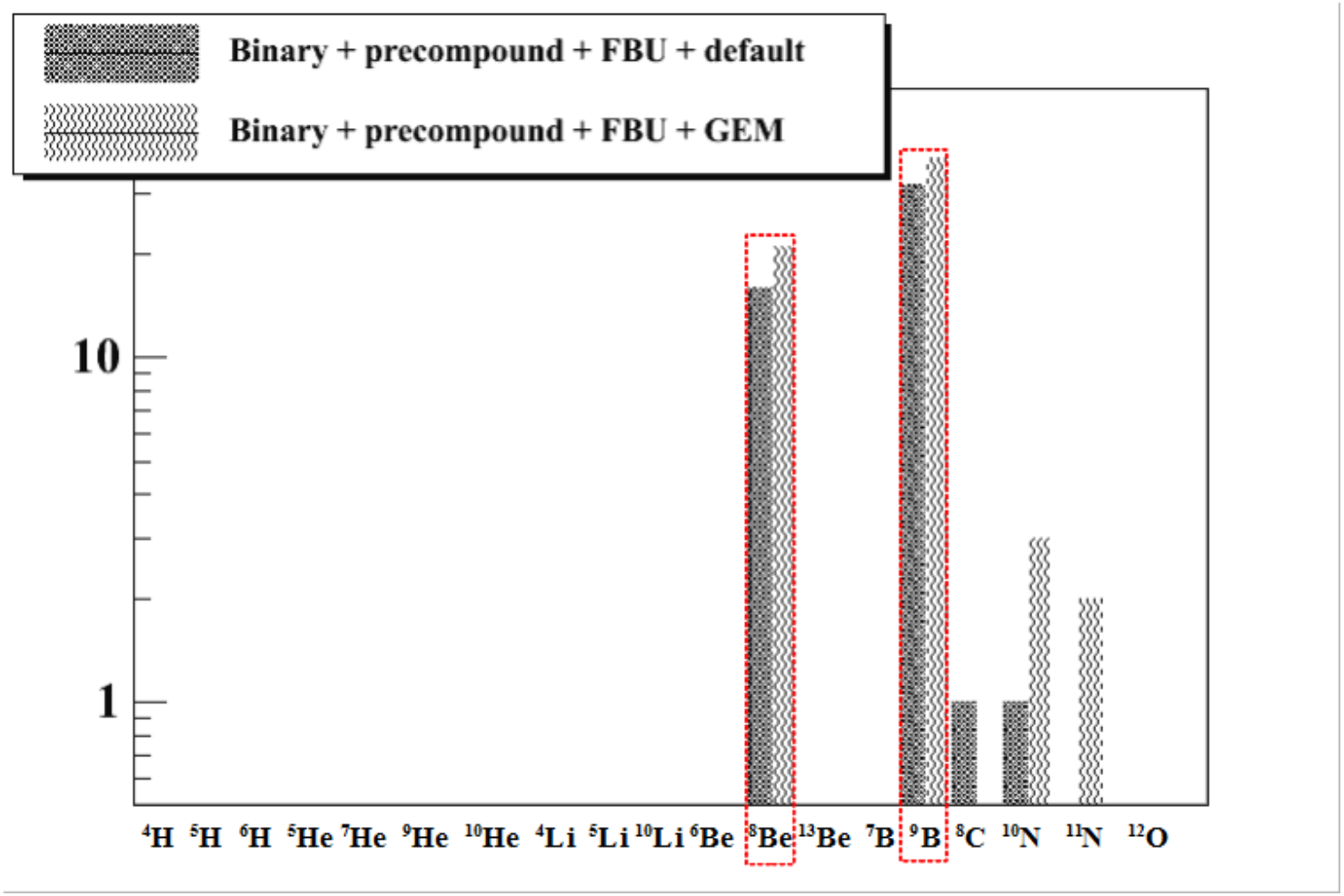

Figure 4.9.: Comparison of the default evaporation model and the generalised evaporation model, each used in combination with the binary cascade, the precompound model and the Fermi breakup. As in figure 4.8, the models are compared with respect to the production of highly unstable isotopes with half lives $\ll 1$ ns. The number of primary protons here is the same as in figure 4.8.

4.4.2. Models of the selected configuration

The complete final physics list used to simulate the spectrometer is schematically shown in figure 4.10. In the following, main parts of this physics list are described.

One particular model is of special interest, because while making an attempt to validate nuclear processes in GEANT4 a thorough understanding of the underlying algorithms is necessary. The model called "binary cascade" is therefore described in more detail than the other mechanisms as it will be invoked most of the time in the spectrometer simulation under study, i.e. when nuclear reactions are induced by protons of 200 MeV energy.

The Standard Electromagnetic Model (SEM)

The SEM is an analytical model and defines electromagnetic processes for all charged particles down to 1 keV [BGG+04]. Since the energy loss processes of electrons, positrons and charged hadrons are very similar, they are enclosed in one solution. Up to a given energy cut-off or production threshold the energy loss of the incident particle is treated as continuous. The mean rates of energy loss are precalculated during the initialisation phase and used to create tables for dE/dx and inverse particle ranges in given materials. During run time these tables serve to determine the continuous energy loss and range of the particle. Above the production threshold the secondary particles - gammas, electrons, and positrons - are explicitly created by sampling over the cross-sections of concrete energy loss processes.

The energy loss of hadrons is computed according to the Bethe-Bloch formula down to 2 MeV. For slower ions their effective charge q_{eff} does not equal the charge of the nucleus anymore, which is due to electron exchange between transporting ion and the media. It is accordingly corrected by the Barkas formula [ARB72]. Since nuclear fragments and recoil nuclei have to be created during run time of the simulation, they are derived from the G4GenericIon ($Z > 2$) and ionisation processes are assigned to this base class during initialisation, i.e. before the simulation starts running. A scaling relation can then be used to define the energy loss [Phy08]:

$$\frac{dE}{dx}(T) = q_{eff}^2[(F_1(T)\frac{dE}{dx}_{base}(T_{scaled} + F_2(T, q_{eff})))] \tag{4.2}$$

where F_1 and F_2 are correction functions taking into account the Barkas ($\propto z^3$) and Bloch ($\propto z^4$) corrections and low energy corrections based on data from ICRU report 73. dE/dx_{base} is the energy loss of the base particle and T_{scaled} is the scaled kinetic energy defined by:

$$T_{scaled} = T\frac{M_{base}}{M_{genericion}} \tag{4.3}$$

The proton is used as a base particle for all positively charged hadrons with non-zero spin and the antiproton for the negatively charged ones. The recoil momentum of the nucleus is neglected in the calculations. Also, apart from the photoelectric effect, the standard electromagnetic model does not account for the binding energy of atomic electrons.

Straggling (energy loss fluctuation) is partially taken into account through the emission of δ-electrons with energies above the energy cut-off. The fluctuations of continuous energy loss are taken into account by the G4UniversalFluctuation model which is rather fast and combines solutions for thin and thick absorbers [Phy08].

Multiple scattering plays an important part in the simulation of electromagnetic interactions and strongly influences its accuracy, especially at low energies when the elastic cross section is large. This is primarily because a detailed simulation of all collisions tends to explode the computation time and so called "condensed history" algorithms have to be used. With such algorithms global effects of the collisions are computed at the end of a track segment (G4Step). The accuracy of the mechanism is then directly limited by the approximations of the multiple scattering theory which has been applied. The angular and spatial momenta provided by the distribution functions used by *G4VMultipleScattering* derivates reproduce those from the Lewis theory [Lew50]. The GEANT4 multiple scattering algorithm has been developed and improved over the last few years by L. Urban and further details can be found in [Urb02] and [Urb06].

The low-energy limit is not well defined for the electromagnetic models. The SEM package can provide tracking down to zero energy. The precision of the simulation in space has to be set via "range cuts". In this study, the default cuts provided by the GEANT4 toolkit are used. This is mainly due to the lack of according recommendations in the field of particle therapy. Also, the issue is rather uncritical since relatively precise estimates of the rates suffice for a prediction of detector performance.

G4Decay

This class simulates the decay of particles in flight and at rest by selecting a decay mode according to branching ratios defined in another class. The secondaries and the kinematics of the decay are generated according to a decay mode which is implemented in a class derived from G4VDecayChannel. Here, the models of α and $\beta^{\pm}$ decay as well e^{-} capture are implemented. These data are derived from the Evaluated Nuclear Structure Data File (ENSDF) which is a data base that "contains evaluated nuclear structure and decay information for over 3000 nuclides. The file is updated on a continuous basis. New evaluations are published in Nuclear Data Sheets" [ENS].

Elastic scattering

The class G4UHadronElasticProcess has been first mentioned by Wright et al [WKF+06] and is included in the coherent elastic package of hadronic models in the GEANT4 distribution. In comparison to its predecessor which had been derived from the GHEISHA code of GEANT3 this model more accurately reproduces the scattered distributions at angles higher than 15°.

The documentation of GEANT4 elastic scattering models in literature is scarce thus making it hard for the application developers to comprehend their characteristics. It is also not clear which cross section data sets were used for parametrisation.

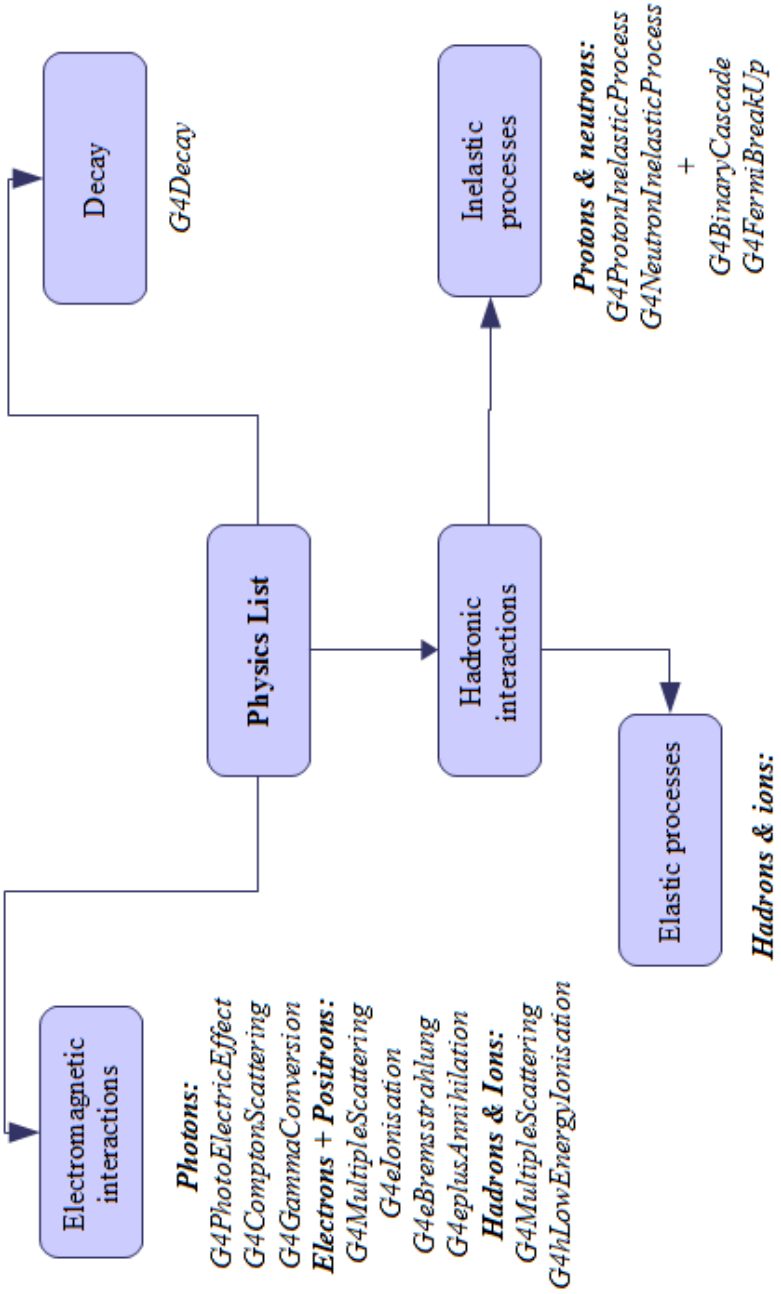

Figure 4.10.: Physics processes and models employed in the detector simulation.

However, in [WKF+06] it is stated, that the new process is relativistically correct, includes coherence effects such as diffraction minima as a result of the nuclear radius, and removes charge exchange as a separate reaction. It also includes improved proton and neutron scattering from proton, deuterium, and helium targets, as well as high precision neutron elastic scattering from isotopes.

Binary cascade

The binary cascade is a new approach to cascade calculation in the sense that it represents a hybrid between a classical cascade model and a quantum molecular dynamics (QMD) model. The binary cascade is based on a three-dimensional description of the nucleus which takes the nuclear density, Pauli's exclusion principle, and total nuclear mass into account. Nucleons are assigned space coordinates and momenta so that cascading can be carried out via binary scattering between individual particles. The connection to QMD lies in the treatment of each participating nucleon as a Gaussian wave packet. The latter is propagated in time and space, meanwhile undergoing collisions in the nuclear medium [FIW04].

Unlike in QMD the Hamiltonian is calculated from simple time-independent optical potentials. The nucleons in the nuclear model that are not participating in binary reactions are simply viewed as a representative nucleon configuration.

The cascade starts with a primary particle of which the type and energy are known and a three-dimensional model of the nucleus. The latter consists of A nucleons with coordinates $\vec{r}_i$ and momenta $\vec{p}_i$. The radii $|\vec{r}_i|$ are chosen randomly from the nuclear density distribution $\rho(|\vec{r}_i|)$ and the particles are placed isotropically within the spherical nucleus model. For nucleons with $A > 16$ the density function has the form of the Woods-Saxon potential as in equation 2.24. For lighter nuclei the function is calculated according to the harmonic oscillator of the shell model (see section 2.3). Mathematical expressions implemented in the model can be found in [FIW04] along with corresponding parameter values. The momenta of the nucleons are picked randomly from the interval between 0 and $p_f^{\vec{max}}(\vec{r}_i)$ with the upper limit directly determined by the nuclear density $\rho(|\vec{r}_i|)$. Finally care is taken that the vector sum of all momenta equals 0, i. e. the nucleus is constructed at rest.

The transportation mechanism employs the geometrical cross section mentioned in section 2.3. First, an impact parameter is chosen randomly on a disk outside the nucleus as shown in figure 4.11. The scattering angle is then a function of the impact parameter and the energy of the primary particle.

In the next step, the distance of closest approach, d_i, (see fig. 4.11) is calculated yielding a corresponding time-of-flight t_i. Then the cross section σ_i is calculated using the momenta of the nucleons in the target and the momentum of the primary particle. Nucleons which fulfill the condition

$$d_i < \sqrt{\frac{\sigma_i}{\pi}} \tag{4.4}$$

become collision candidates. They are ordered by increasing time-of-flight and the projectile is then transported by the time step corresponding to the earliest collision

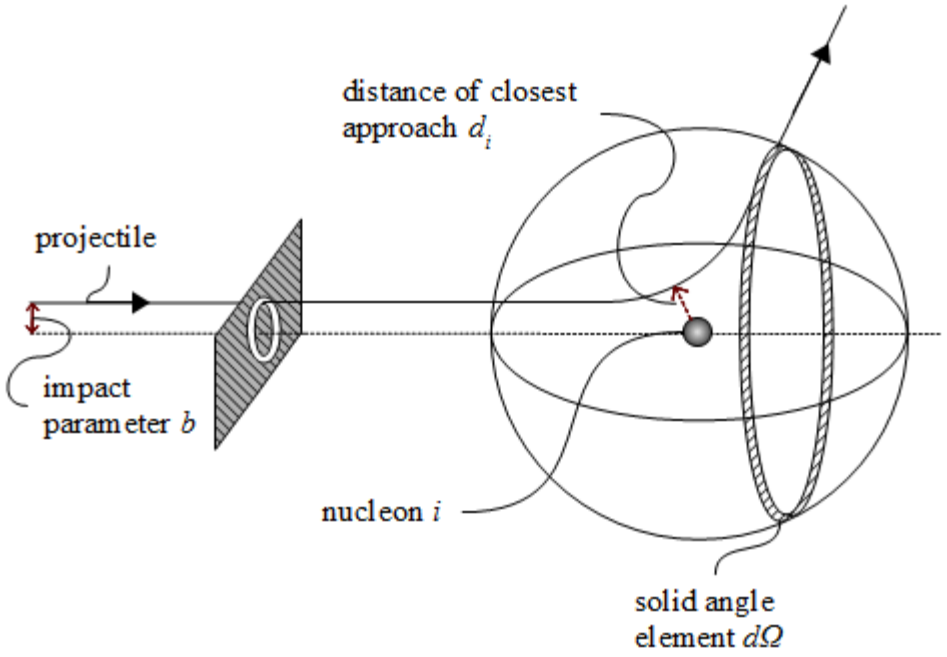

Figure 4.11.: Geometrical view on the binary collision process. For the sake of clarity, this visualisation assumes the simple case of elastic nuclear scattering on a hydrogen atom.

candidate. During propagation within the nuclear field the equation of motion of the particles is solved using one of the Runge-Kutta integration methods for the iterative approximation of solutions to ordinary differential equations [PTVF88]. Corrections for Coulomb effects are applied as well. The cumulative effect of the nucleons not participating in the cascading process is approximated by a scalar optical potential defined by the local Fermi momentum:

$$V(|\vec{r}_i|) = \frac{p_F^2(|\vec{r}_i|)}{2m} \tag{4.5}$$

where m can be the mass of a neutron or a proton. Since the reaction is viewed as a series of binary collisions between individual nucleons, free particle cross sections and parametrisations thereof are employed to determine σ_i in equation 4.4. These cross sections are corrected to take Pauli constraints into account. The experimental data and parametrisations for elastic and inelastic nucleon-proton and nucleon-neutron collisions are acquired from the Particle Data Group [NG10]. During simulation a tabulation of the data for centre of mass energy $\sqrt{s} < 3\ GeV$ is applied. Above this limit quark and gluon degrees of freedom have to be treated explicitly.

At the end of a reaction step a set of secondary particles is obtained which represent candidates for further collisions. However, these particles can only be propagated further as new primary particles if the final state configuration is Pauli allowed and none of the particles have a momentum smaller than the Fermi momentum. If not, the inter-

action is discarded and the original primary particle is transported to its next collision candidate within the nucleus.

Angular distributions for elastic scattering are obtained from differential cross section data in the SAID data base [SAI]. For all other processes angular distributions are calculated in analogy to the ultrarelativistic quantum molecular dynamics model (UrQMD). This is a microscopic transport approach where all hadrons are propagated on classical trajectories and reactions are modelled by way of stochastic binary scatterings of two Fermi gases diffusing into each other, according to the collision term of the Boltzmann-Uehling-Uhlenbeck equation. Phenomenological potentials like Yukawa, Coulomb, and Pauli potentials are used for the calculations at lower energies, which represent the range relevant to particle therapy. At energies higher than $\sqrt{s} > 6\ GeV$ the quark degrees of freedom are taken into account. In contrast to the UrQMD model, collisions between participants are not taken into account by the binary cascade so that the algorithm can only be applied for small particle densities. This implies that the nucleus is treated like a gas rather than a dense fluid, the latter more commonly being treated in molecular dynamics.

As soon as the kinetic energy of the cascade participants falls below 70 MeV they have to be treated by a precompound model. If the kinetic energy of a primary particle is lower than 45 MeV cascading is not invoked in the first place and the process is treated directly by the precompound mechanism. At the end of the cascading process a residual prefragment is formed and its characteristics like the number of nucleons, charge, number of holes, number of all excitons, number of charged excitons and the four-momentum are passed to the precompound and nuclear de-excitation models. Here, the number of holes is the difference of the number of nucleons in the initial and prefragment states. Accordingly, the number of excitons is the number of nucleons captured by the prefragment.

Precompound model

This model represents a transition between the cascade and the equilibrium deexcitation models. Accordingly, the underlying mechanism of neutron, proton, deuteron, tritium, and helium emission is applied until the system reaches equilibrium. The latter is characterised by the equilibrium number of excitons n_{eq}:

$$n_{eq} = \sqrt{dgE^*} \tag{4.6}$$

where g is the single particle level density and E^* is the excitation energy of the nucleus. The non-equilibrium evaporation produces isotropic angular distributions.

Fermi Breakup

The Fermi statistical break up model can be applied to light systems with atomic number $A < 17$ [Phy08], [BIM+87]. Almost all relevant fragments appearing in the detector simulation described here fall into this range. In such light systems the excitation energy is comparable to the binding energy of the nucleus. Therefore, after reaching its equilibrium state the nuclear fragment will most likely disassemble into two or more

smaller clusters and individual nucleons. This process can be characterised as a type of explosive decay.

The probability of an excited nucleus to decay into a number of clusters with certain atomic numbers is calculated based on the spin factor (i. e. number of states with different spin orientations), the permutation factor (considers the identity of components in final state), and the volume of the decaying system normalised by $(2\pi\hbar)^3$.

This approach has at first been introduced by Enrico Fermi in 1950 where he describes the multiple production of nucleons and pions in proton collisions [Fer50].

Evaporation

The evaporation models are commonly employed for deexcitation of heavy compound nuclei. Here, the excitation energy is assumed to be small compared to the binding energy of the nucleus.

The successive evaporation of particles is often described using the Weisskopf-Ewing expression (see section 2.3, eq. 2.15). Its implementation inside the GEANT4 toolkit is mainly based on the approach suggested by Dostrovsky and Fraenkel [DF59] which allows for an analytical integration thus saving computation time. They start with a differential form of the Weisskopf-Ewing expression, where the probability that a nucleus with excitation energy E^* emits a particle in its ground state with kinetic energy ϵ:

$$P(\epsilon)d\epsilon = g\sigma_{inv}(\epsilon)\frac{\rho_d(E_{max}-\epsilon)}{\rho_p(E^*)}\epsilon d\epsilon \tag{4.7}$$

where $\rho_p(E^*)$ and $\rho_d(E_{max}-\epsilon)$ are the level densities of the evaporating (parent) and the residual (daughter) nuclei, respectively. The factor g includes the spin and mass of the emitted particle and $\sigma_{inv}(\epsilon)$ is the inverse (capture) cross section.

In order to determine the total emission probability, the inverse cross section as well as the level density for the final state and the integration limits have to be calculated. The former is defined by use of the geometrical cross section σ_g:

$$\sigma_{inv}(\epsilon) = \sigma_g\alpha(1+\frac{\beta}{\epsilon}) \tag{4.8}$$

where the parameters α and β are adjusted for neutrons and protons separately. For the latter, the Coulomb potential is calculated from electrostatics and then corrected for the quantum mechanical phenomenon of barrier penetration by use of a coefficient designed to fit the results of continuum theory. The level density as a function of excitation energy is based on the Fermi gas model and was initially proposed by Weisskopf:

$$\rho(E) = Ce^{2\sqrt{a(E-\delta)}} \tag{4.9}$$

where δ is the pairing energy correction and a is the level density parameter. The δ-correction becomes necessary because of the dependence of the level density on whether the number of protons and neutrons in the nucleus is odd or even. $\delta = 0$ is chosen as a type of ground state for odd-odd nuclei and $\delta \geq 0$ is applied in all other cases.

The maximum evaporation energy of the particle is computed from the excitation energy of the compound by subtracting the separation energy of the emitted secondary

and its pairing energy. In addition, a correction is applied to take the recoil energy of the residual nucleus into consideration.

The generalised evaporation model (GEM) suggested by Furihata [Fur00] is an extension of the Weisskopf-Ewing model. It also treats heavier secondaries than alpha particles and considers 66 nuclides altogether (up to ^{28}Mg) including their excited states. The GEM model uses a more accurate definition of the level density compared to the Dostrovsky approach in equation 4.9 by taking the nuclear temperature into account.

In the case of 200 MeV protons inducing nuclear reactions within a graphite target the system can be considered as a light one so that the excitation energy of the residual fragment is comparable to its binding energy. Thus, the use of Fermi break up is recommended for the simulation of deexcitation processes in this study.

4.5. Data retrieval and storage

Having set up the geometry and physics of the simulation the remaining questions are how the necessary data should be recorded during simulation, and what would be a convenient format for further analysis. While evaluating the performance of the detector, whether its a real or computer experiment, great quantities of data need to be recorded and analysed. This and other conditions lead to the following set of demands on the format:

- The storage should be implemented on an event-by-event basis, in order to make reconstruction of individual events possible. Here, "event" includes all trajectories and detector hits caused by a single primary proton, i. e. one primary particle is created per event (see section 2.5.3).

- Which events will be saved should be specified by a preset condition.

- In each event there is also a set of different types of data that need saving, including time-of-flight and energy deposition as well as particle incidents on the Veto system. The data types of the simulation also include the so called Monte Carlo "truth", e.g. the time-of-flight is recorded along with the particle name and Stop scintillator number. This is achieved through use of nested data types from the standard template library (STL).

- The chosen format should allow for easy access via object-oriented C++ programming thus aiding the development of well structured analysis code.

- The results of detector evaluation will in most cases be depicted and further analysed by way of onedimensional and twodimensional histograms, which an optimal storage and analysis tool should support.

- The same storage format should be applicable to experimental data acquisition so that analysis programs can be applied to experimental data after having been trained and optimised using simulation results.

ROOT is an object-oriented C++ toolkit developed by CERN. It provides a set of object-oriented frameworks with comprehensive functionality allowing to handle and analyse large amounts of data in an efficient way. The ROOT "Tree" container has been designed to store large quantities of same-class objects, using compression of the object header to optimise storage. Thus, the simulation output can be analysed and binned into histograms very conveniently after the simulation is finished.

ROOT Trees will also be employed during data acquisition with the actual detector. The customised class for data acquisition is a slimmer version of the simulation data class. In addition to time-of-flight and energy deposition the simulation data class provides the Monte Carlo truth such as particle species for each time-of-flight and energy deposition, whether an inelastic process occurred in the START scintillator or graphite target and so on. Thus, the analysis and identification of nuclear reactions from measured data can be trained and tested on Monte Carlo samples prior to the actual experiments.

During simulation all relevant data are accumulated on a step-by-step basis within a user class derived from G4UserSteppingAction. After the primary particle and all of its secondaries are tracked the event is complete and can be stored within the ROOT Tree by a G4UserEventAction derivate.

5. Simulation: results

In the following sections the most critical characteristics of the detector are analysed using the GEANT4 simulation described in chapter 4. The count rates in each Stop scintillator as well as the correlation of time-of-flight and energy deposition are generated and the influence of several background sources is investigated.

5.1. Count rates in each Stop scintillator

While the total count rates shown in figure reffigStableCountRateComparison establish the fact that light and heavy target fragments reach the Stop scintillators and are thus available for detection additionally serving for estimations of beam time requirements, the count rates in each Stop scintillator help to assess the coverage of the scattering angle. This is especially crucial for the detection of heavier target fragments as they are mostly scattered at large angles.

For each Stop hit, the particle name and scintillator number have been recorded using the Stepping Action user class. Figure 5.1 shows the counts in each scintillator for one light and one heavy particle created by 10^{10} primary protons within the 0.75 mm graphite target.

Both histograms in figure 5.1 show fluctuations between neighbouring Stops. This is due to the staggered alignment of the Stop scintillators implicating varying coverage of the solid angle (see figure 4.3).

While there is a high rate of protons in the two Stop scintillators closest to the beam, there is also a significant amount registered at higher angles. The high rate in the centre of the histogram is mainly caused by elastically scattered primary particles. With increasing scattering angles the protons are more likely to originate from nuclear reactions. Direct processes produce forward directed secondaries and will contribute significantly to the rates in Stops 9 to 12. In contrast, the compound nucleus deexcitation plays an increasing role towards higher angles. The count rate fluctuations between neighbouring scintillators are still present for protons at higher scattering angles - they are simply not resolved well in figure 5.1.

The boron isotope ^{11}B shows a much wider scattering characteristic than the protons. However, the local count rate maxima are within the angle range covered by the Stop scintillators. The actual presence of local maxima indicates a forward directed process thus implying a direct reaction mechanism.

However, the Stop scintillators of the detector which is subject to evaluation here cover only about 12% of the 2π solid angle. Thus, the events where two or more hadrons

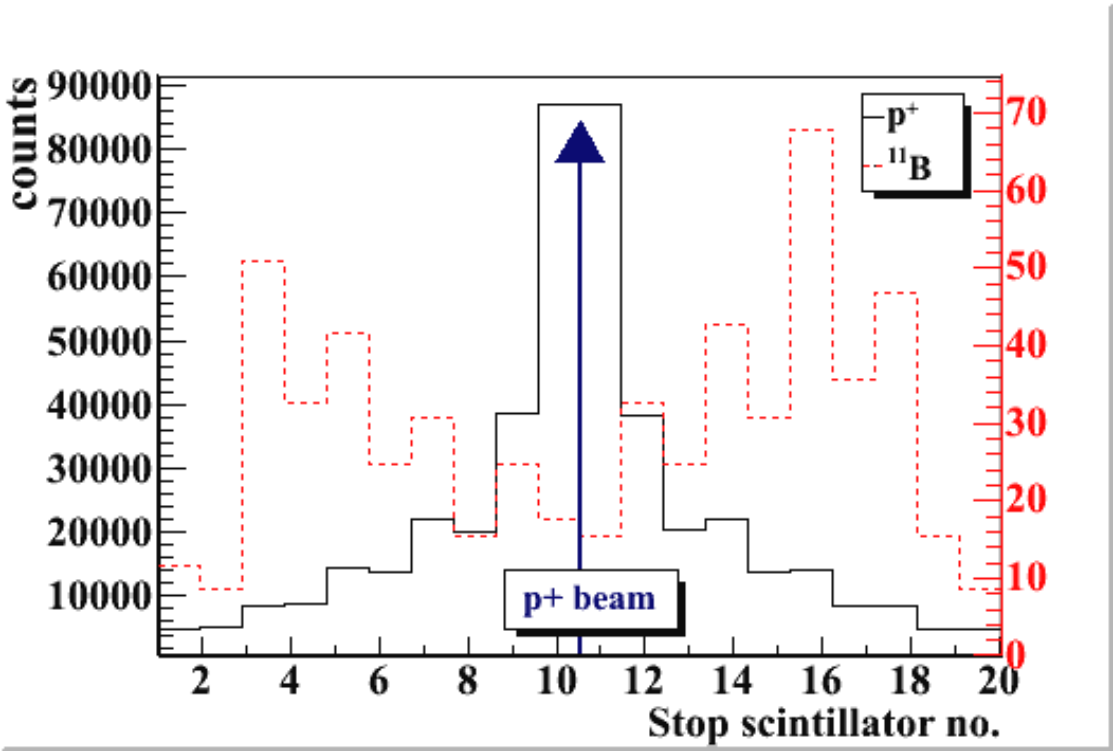

Figure 5.1.: Absolute counts in each of the 20 Stop scintillators for protons (black, left axis) and the ^{11}B fragments (red, right axis). The outermost Stop scintillators 1 and 20 are at 80.11° with respect to the beam. The inter-Stop angle is 7.67° and slightly higher only between scintillators 10 and 11.

hit a Stop become relatively rare. In 26% of all nuclear reactions with Stop hits there is a coincidence of two or more particles on the scintillators. And only in 6% of all nuclear reaction events we get a coincidence of two or more hadrons (i.e. 20% of the mentioned 26%).

5.2. Energy spectrum of scintillator 8

During the measurement, the energy deposition and the time-of-flight will be recorded separately for each of the 20 Stop scintillators. The simulated energy spectrum within one single Stop detector provides the basis for an estimation of the expected light signal and can also indicate useful energy cuts for the analysis of experimental data. The distribution of energy deposited by different particle groups inside Stop scintillator no. 8 is shown exemplarily in figure 5.2.

Basically, there are two parts of the spectrum, each originated by one of the two particle groups: electrons, neutrons and gamma photons with a small energy deposition mostly lower than 1 MeV on one side and ions on the other side (red and green in figure 5.2). Since neutrons show almost no interaction with the plastic scintillator material their energy contribution will almost always be found in the 0 MeV bin. They are included in the evaluation for the sake of completeness.

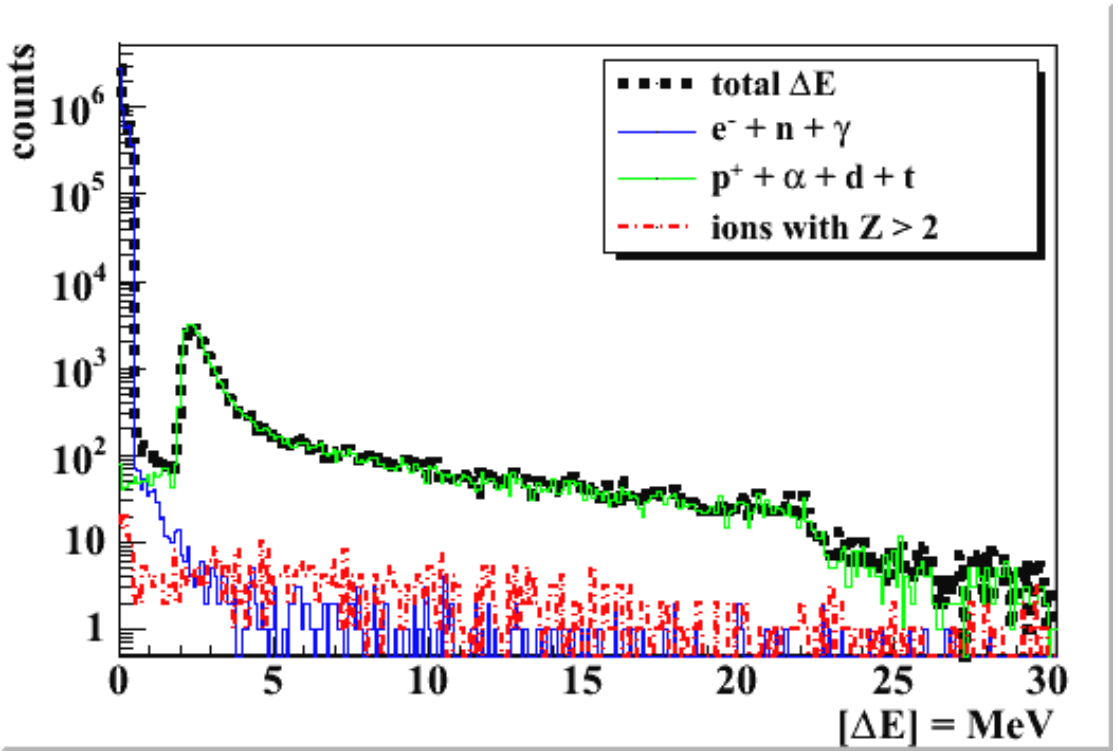

Figure 5.2.: The energy spectrum of all particles and certain particle groups deposited inside Stop scintillator 8 (cf. figure 5.1). Number of primary protons: 10^{10}.

5.3. Correlation of time-of-flight and energy deposition

The fundamental requirement for the identification of particles hitting the Stop scintillators is the correlation of their time-of-flight to the energy they deposit. Figure 5.3 shows a typical correlation histogram for protons. Originally, the simulated data contains two correlation curves - one for each of the two flight ranges between the Target and the Stop detectors caused by the staggered alignment of the latter. In figure 5.3 the times-of-flight have been normalised to 70 cm so that the curves are merged.

The correlation curve can be divided into two main parts along the time-of-flight axis: a lower and an upper part. The lower part of the curve is effected by protons which pass through the Stop detectors without stopping. This is plausible because smaller times-of-flight fit higher momenta and higher penetration depths. As the protons slow down they deposit more energy in accordance with the Bragg relationship described in section 2.1.

At a time-of-flight of just below 20 ns the protons have not enough kinetic energy left to travel the entire distance within the plastic scintillator and to escape on the "other side". They rather stop and deposit their entire kinetic energy within the plastic scintillator. This circumstance causes the transit from the lower part of the correlation curve to its upper part. Here, the momentum of the particles decreases with larger times-of-flight and they stop at decreasing depths within the Stop detectors.

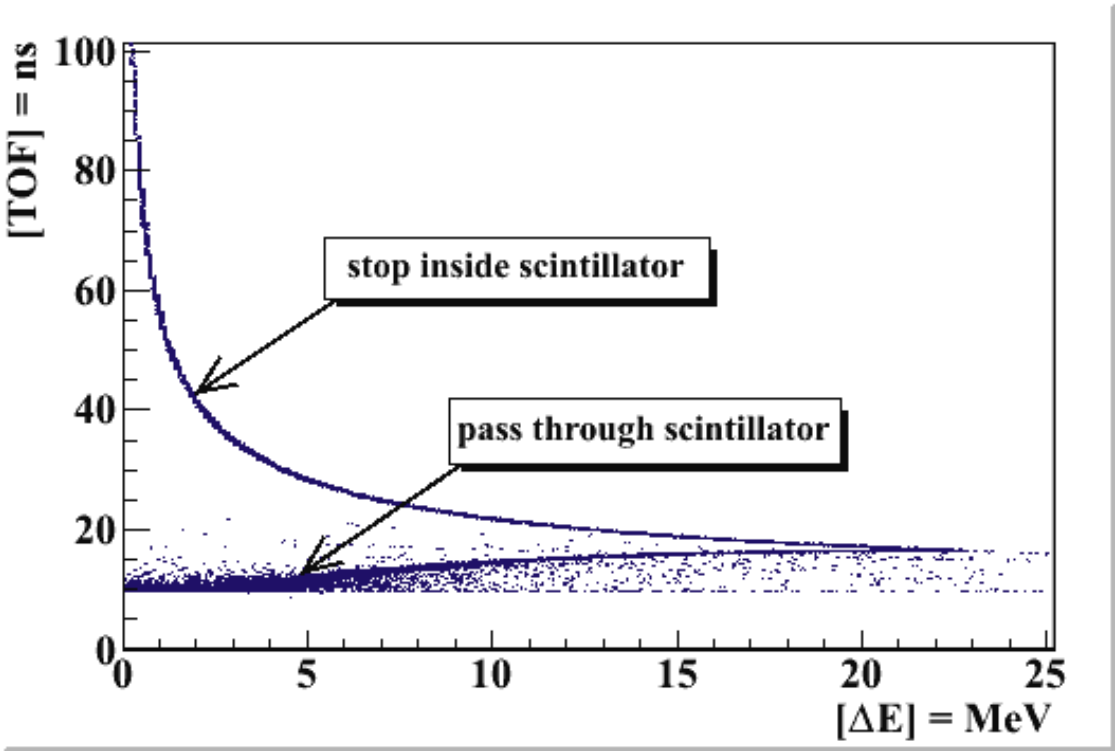

Figure 5.3.: Simulated correlation of time-of-flight and energy deposition of protons. For a better illustration, only a portion of the original histogram is displayed.

Since the time-of-flight measurement is initiated by the Start scintillator, there is a cut-off just below 10 ns in figure 5.3 which corresponds to the time-of-flight of a primary proton between the Start detector and one of the Stop scintillators. In the simulation, the time-of-flight values reach over 400 ns when the vacuum inside the chamber is kept at 0.1 mbar. However, these high times-of-flight correspond to very low energy depositions (<1 MeV) and will not be detected in the real experiment.

With the lower part of the curve in figure 5.3 there is also a fair amount of multiple scattering background. Without detailed investigation this background can be attributed to scattering events in the Start scintillator which were not picked up by the Veto system and to scattering in the equipment.

Figure 5.4 shows a combined plot of the correlation histograms of particles with significant count rates. While electrons, gamma photons and neutrons are found in the lower left corner, protons and other ions exhibit the typical correlation curve. With increasing mass the correlation curves shift towards the upper right corner of the histogram.

An additional deduction which can be made from figure 5.4 is that most ions with $Z > 2$ stop inside the scintillator, i.e. they lack the lower part of the correlation curve which can only be observed for protons and deuterium. There is one distinct problem which arises when the fragments get stuck inside the scintillators - only their mass can be distinguished but not their charge. It means, the upper part of the correlation curve superposes for ions with equal mass number. This is shown exemplarily for the mass of 11 u in figure 5.5.

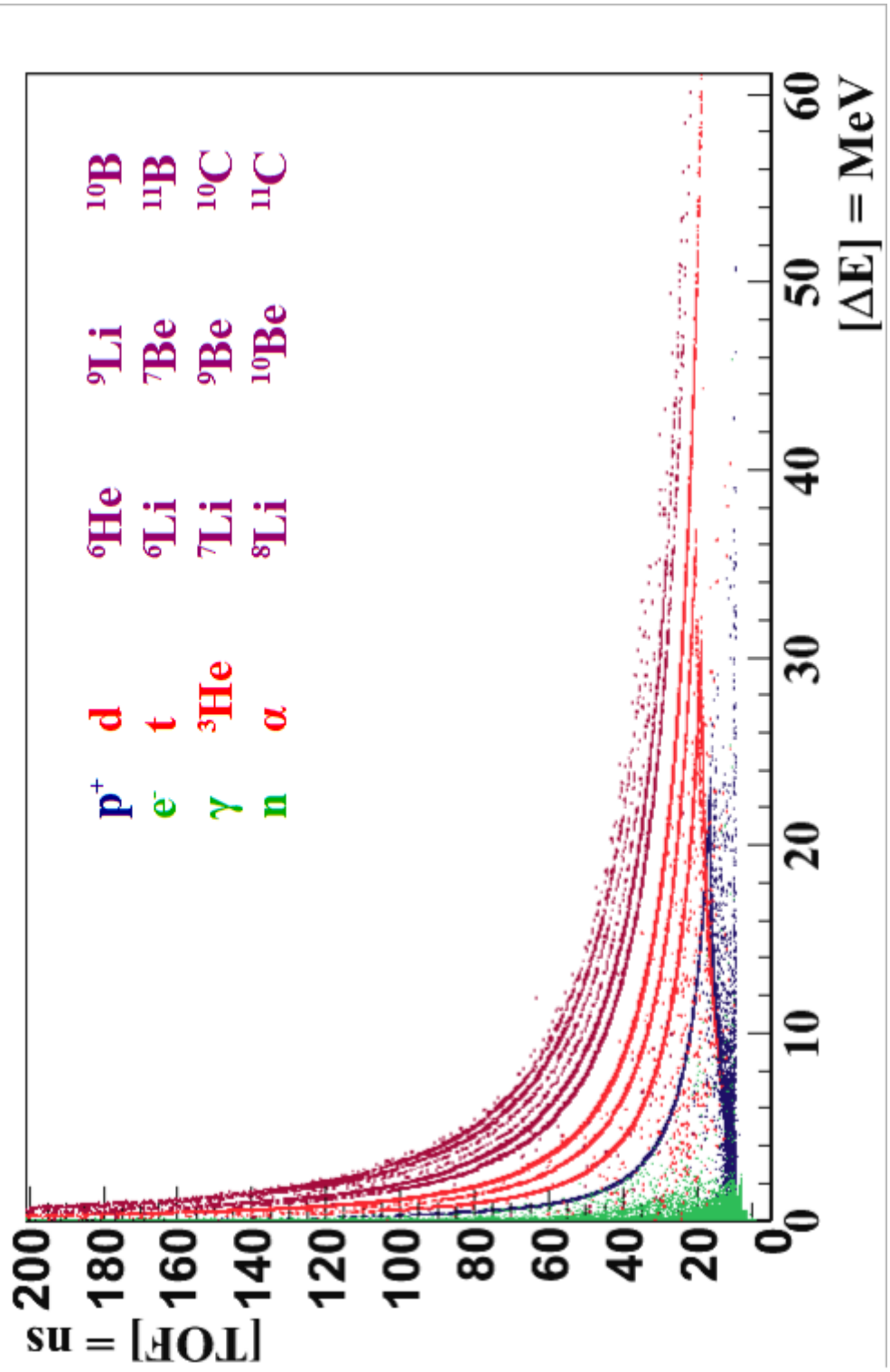

Figure 5.4.: Correlation of time-of-flight and energy deposition. Different groups of particles like γ, e^-, and neutrons, like the light ions p^+, deuterium, tritium, ^{3}He, and α, and like the heavier target fragments (Z>2) occupy different parts of the histogram.

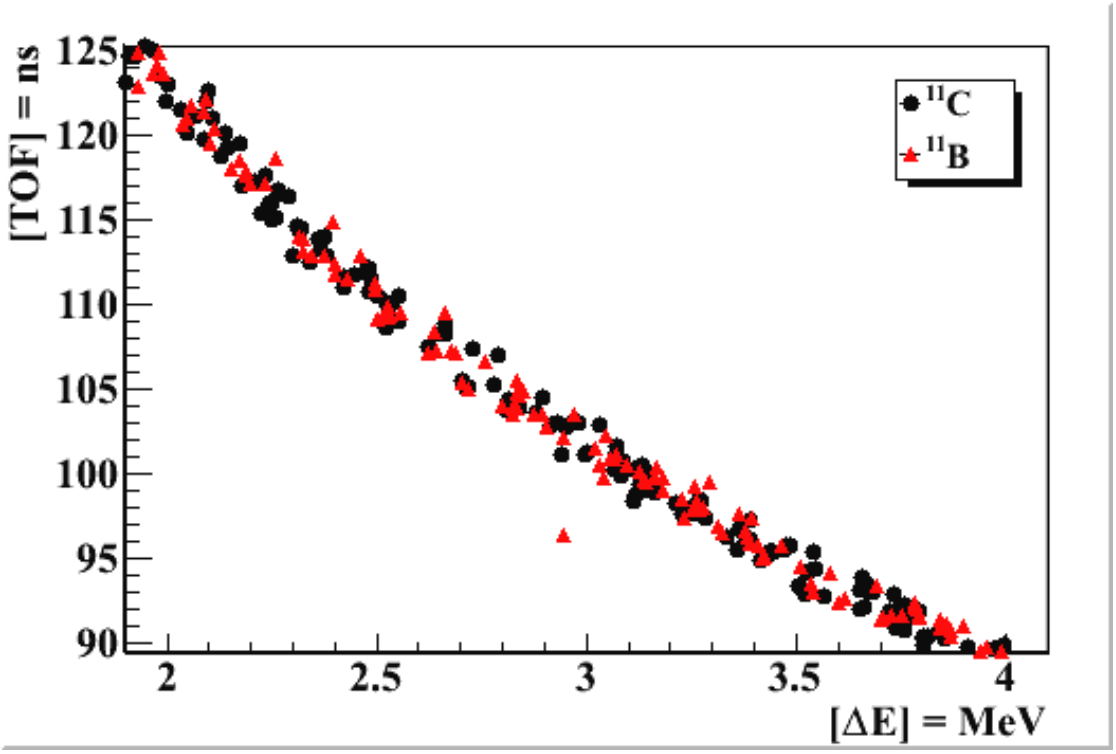

Figure 5.5.: Correlation of ions with mass = 11 u. For illustration purposes only a small part of the correlation is shown. The superposition occurs throughout the correlation curve.

5.4. Mass spectra from simulated correlation

As stated in section 5.3, only the mass but not the charge of the target fragments can be reconstructed from the correlation histograms. In principle, two formula suffice for the calculation of a particle's mass from its energy deposition and time-of-flight, provided that said particle stops in the scintillator:

$$\gamma = \frac{1}{\sqrt{1 - \frac{v^2}{c^2}}} \tag{5.1}$$

and

$$E_{kin} = (\gamma - 1) \cdot m \cdot c^2 \tag{5.2}$$

Here, γ is the Lorentz factor, E_{kin} is the energy deposited in the scintillator and $v = \frac{tof}{radius}$ is the velocity of the particle. There is also a time-of-flight offset of 5.68 ns taken into consideration which corresponds to the time a 200 MeV proton would need to cover the distance between the Start scintillator and the graphite target. Figure 5.6 shows the resulting reconstructed mass spectrum.

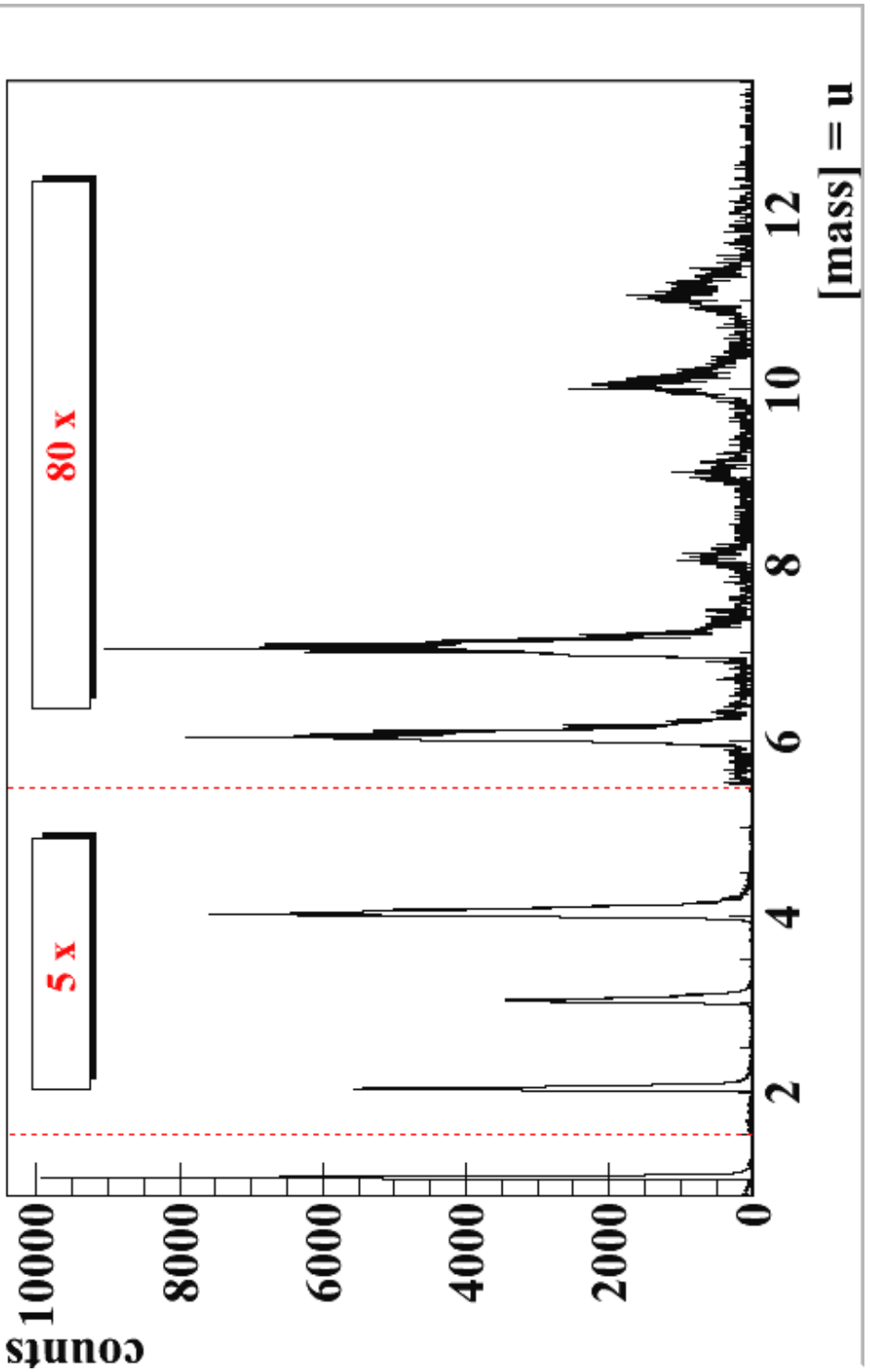

Figure 5.6.: Mass spectrum reconstructed from simulated correlation of tof and ΔE. Due to their relatively low rates counts of ions with A > 1 and A > 5 have been scaled by factors of 5 and 80, respectively.

The lower branch of the proton correlation curve has been excluded from the reconstruction in figure 5.6 only taking mass values above 0.8 u into consideration. The remaining width of the mass peaks is caused by energy loss straggling in the Start scintillator and the 0.075 mm Graphite target. The time and energy resolution of the detector system are not considered in the simulation at this stage.

5.5. Sources of impairment of detector performance

This section addresses the influence of several sources of background radiation and other issues which can diminish the detector performance. Section 5.5.1 deals with the high energy background from the START plastic scintillator which often passes the aluminium walls of the detector chamber and creates hits on the STOP scintillators. In section 5.5.2 the influence of the residual pressure inside the detector chamber on the reconstructed mass spectra is evaluated. Sections 5.5.3 and 5.5.4 investigate the energy loss and the alteration of momentum direction of fragments inside the graphite target, respectively. The range of the target fragments within the Stop scintillators is evaluated in section 5.5.5.

5.5.1. Background from START scintillator

After the aluminium vacuum chamber had been added to the simulation geometry, the efficiency of the Veto system was evaluated. At first, only one Veto detector had been envisaged for the setup. Its main role was the detection of forward directed secondary particles from nuclear interactions in the Start detector, which consists of carbon and hydrogen itself. This way, nuclear scattering events in the Start could be discriminated from the actual data.

Initially, the assumption was made that secondary particles, scattered at higher angles would not pass the aluminium barriers of the box. However, as earlier simulations have shown, many higher energy protons emitted from the Start detector pass the box walls and hit the Stop scintillators. The rate of these events is considerable due to the thickness of the Start scintillator. The latter needs to be a compromise between background elimination and the light signal received by the SiPM. Even with a 1 mm thick Start scintillator and an 0.075 mm graphite target the number of elastic and inelastic proton processes in the START amounts to about 18% of the number of reactions in the target.

As a consequence, a second Veto detector was placed 5 cm behind the Start detector along the beam axis (see fig. 4.3). An initial aperture of 4 mm was chosen for this second Veto, and the pencil beam was broadened to represent a Gaussian with a 2 mm FWHM according to an earlier COSY publication [KD03]. Subsequent simulations exhibit substantial improvement in background rejection, as shown in figure 5.7. The experimental setup has been modified accordingly.

Particularly the lower left corner of the correlation histogram appears more clearly in figure 5.7 after the events with a Veto hit have been eliminated from the data set. While in the upper picture several proton curves can be distinguished the adjusted plot shows only one distinctive proton correlation.

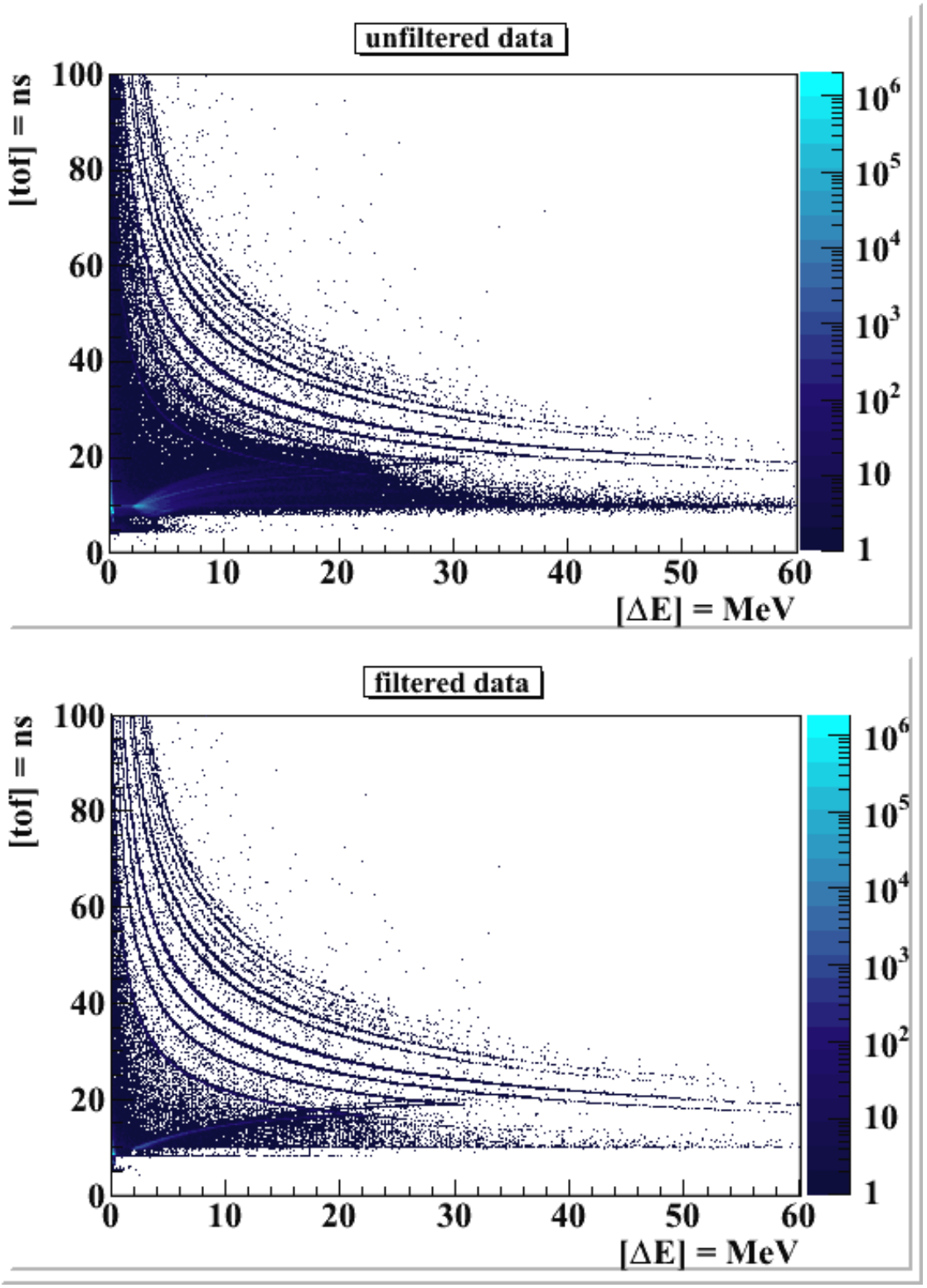

Figure 5.7.: Background elimination by the Veto system (both Veto detectors): correlation of original data (top) and correlation of events without a hit on the Veto (bottom).

5.5.2. Residual pressure in the detector chamber

While evaluating the individual ion mass spectra reconstructed from earlier simulations, an unexpectedly high width of the mass peaks has been observed along with a dispersion towards lower mass values. These observations can be inferred from the topmost plot in figure 5.8.

Presuming that this could be due to the residual pressure inside the detector chamber (1 mbar at that point), a simulation with 10^{-6} mbar has been carried out. The resulting spectrum can be seen in the bottom plot of figure 5.8. The strong improvement in the separation of the mass peaks leads to the conclusion that the above assumption is valid and that the vacuum inside the detector chamber should be improved.

Since a vacuum of 10^{-6} mbar is technically not feasible, a simulation at 0.1 mbar has been carried out. The resulting mass spectrum is shown in the centre of figure 5.8. Obviously, keeping the residual pressure below this threshold is sufficient for an accurate reconstruction.

5.5.3. Target thickness: energy loss

The GEANT4 simulation of the detector has shown, that most of the target fragments possess kinetic energies lower than 20 MeV (figure 5.4), placing them in (or near) the Bragg peak region of the depth dose relationship. Under these circumstances, the target thickness becomes a crucial parameter and its influence on the kinetic energy of the fragments must be investigated. In a thick target, the fragments will deposit too much of their energy and their initial momentum will be strongly altered, thus distorting the kinematics and, accordingly, the reconstruction process. Figure 5.9 shows the energy lost by some of the most frequent fragments created within an 0.075 mm graphite target.

Considering that a maximum of 20-25 MeV are deposited in the Stop scintillators and some energy is lost due to residual gas inside the detector chamber, the conclusion can be made that many ions lose between one third and one half of their initial kinetic energy. This loss is considerable and calls for use of much thinner targets in future. Since, at creation of the secondaries, the ion energy often falls within the Bragg peak condition or close to it, the relationship between target thickness and energy loss is not linear and future estimations have to be verified by Monte Carlo simulations.

5.5.4. Target thickness: momentum direction

Considering the strong influence of the target thickness on the kinetic energy of the fragments, the influence on their momentum direction must be analysed as well. Figure 5.10 shows how the angle between the ion trajectory and the primary beam changes between reaction vertex and the point where the ion exits the target. From this we can conclude that the change in momentum direction is small.

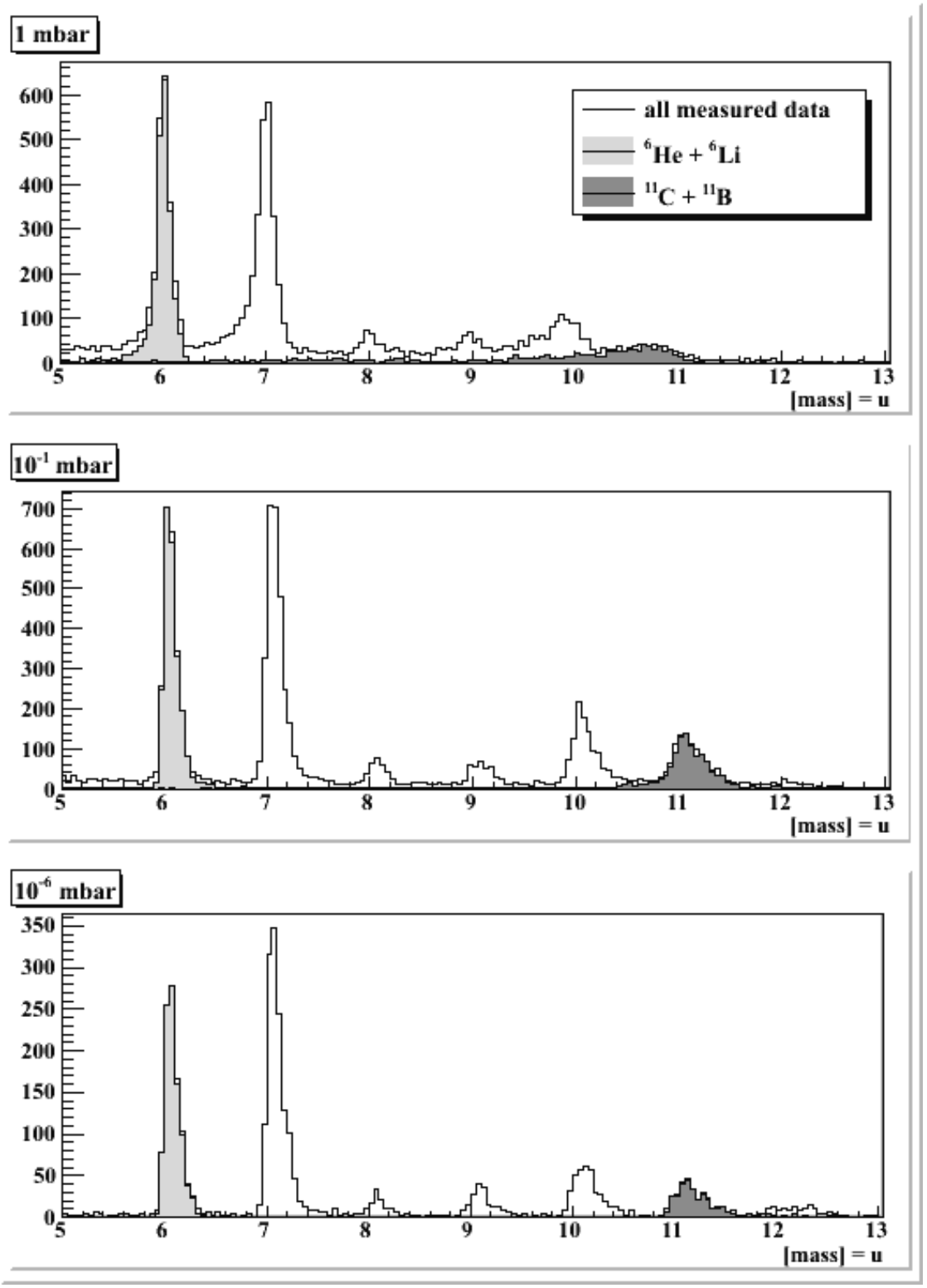

Figure 5.8.: Mass spectra from correlations simulated with varying pressure inside the detector chamber.

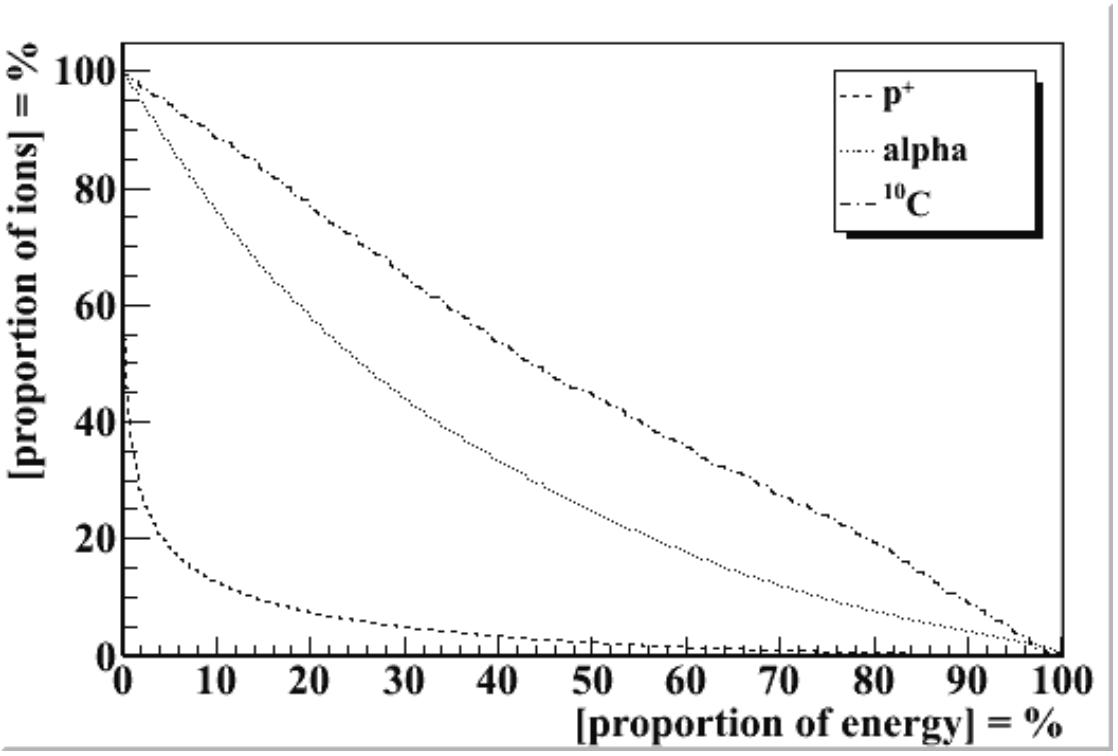

Figure 5.9.: Cumulative plot of energy loss of light and heavy ions inside the graphite target. For example, 80% of all ^{10}C-ions loose 20% of their initial kinetic energy inside the target.

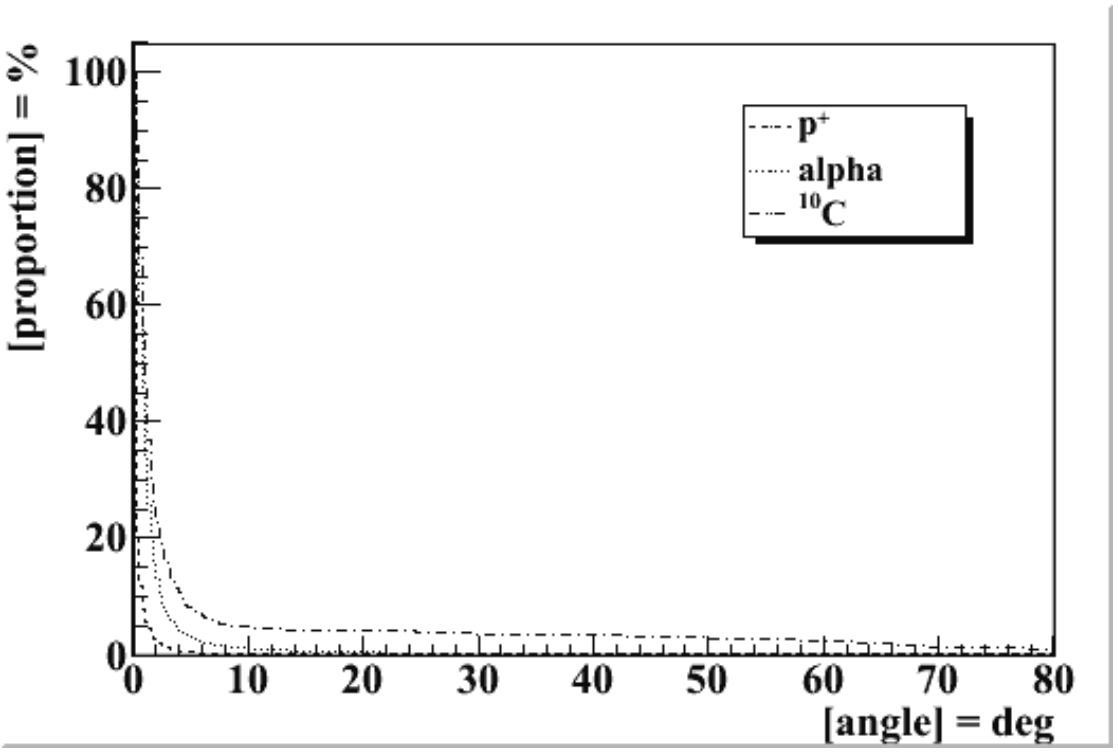

Figure 5.10.: Change of ion momentum direction with respect to the beam while travelling through the target. For example, only 20% of all ^{10}C-ions deviate by as much as $4°$.

A change of 4° which is reached by about 20% of all ^{10}C-ions in figure 5.10, corresponds to a shift of approximately 5.6 cm on the Stop scintillator surface (after a flight of 80 cm in vacuum). This is about half of the width of a Stop scintillator, which is 10 cm. Considering an inter-Stop spacing of 7.67°, the alteration of 4° falls well below the angle resolution of the experiment.

5.5.5. Range within Stop scintillators

Figure 5.4 has shown that most of the target fragments with $A \geq 2$ stop inside the scintillator. However, in order to distinguish isotopes with equal mass number and different charge, the correlation event should come to lie on the lower part of the curve. Thus, the question arises as to how thin the STOP scintillators would have to be in order for the heavy target fragments to pass through them.

Figure 5.11 shows the ion range inside the plastic scintillator material. Almost 80% of the protons traverse the stop scintillators depositing only part of their energy. A high contribution to this value is probably originated by the two scintillators closest to the beam (see figure 5.1) and most likely to be hit by primary protons which are only slightly deflected from their initial direction of flight by elastic scattering.

Taking a look at heavier particles, like α and ^{10}C almost all particles stop inside the first tenth of a millimetre. So, in order to get an actual dE/dx measurement the Stop scintillators would have to be less than 100 μ thick.

5.5.6. Stop scintillator wrapping

Previous tests of the Stop scintillator resolution conducted in the laboratory by the medical physics group of the RWTH Physics department using an Am^{241} α-source have shown that the light signal produced within the plastic scintillator is very small. Motivated by this circumstance and the conclusions from section 5.5.5, measures were taken to amplify the light signal which reaches the SiPMs mounted on the Stop detectors. In addition to the wavelength shifting fibres mounted on both sides of the Stop detectors and read out by 1×1 mm SiPMs, each, the scintillators were covered with Mylar® foil.

As most ions show small kinetic energies in the simulation (see sections 5.2 and 5.3), the influence of the Mylar® wrapping must be analysed within the simulation. A standard Mylar® foil was used to cover the scintillators and its thickness was estimated at 6±0.15 μm using a micrometer calliper.

In the GEANT4 implementation of the spectrometer setup the geometry has been adjusted by putting the Stop scintillators into boxes of polyethylene (PET) which exceeded the thickness of the scintillators by 12 μm. In turn, these boxes were inserted into boxes of aluminium with their thickness exceeding that of the PET boxes by $8e^{-10}$ m which is a rough estimate of the few atomic layers of aluminium in the Mylar® foil. Figure 5.12 shows the resulting correlation of time-of-flight vs. energy deposition.

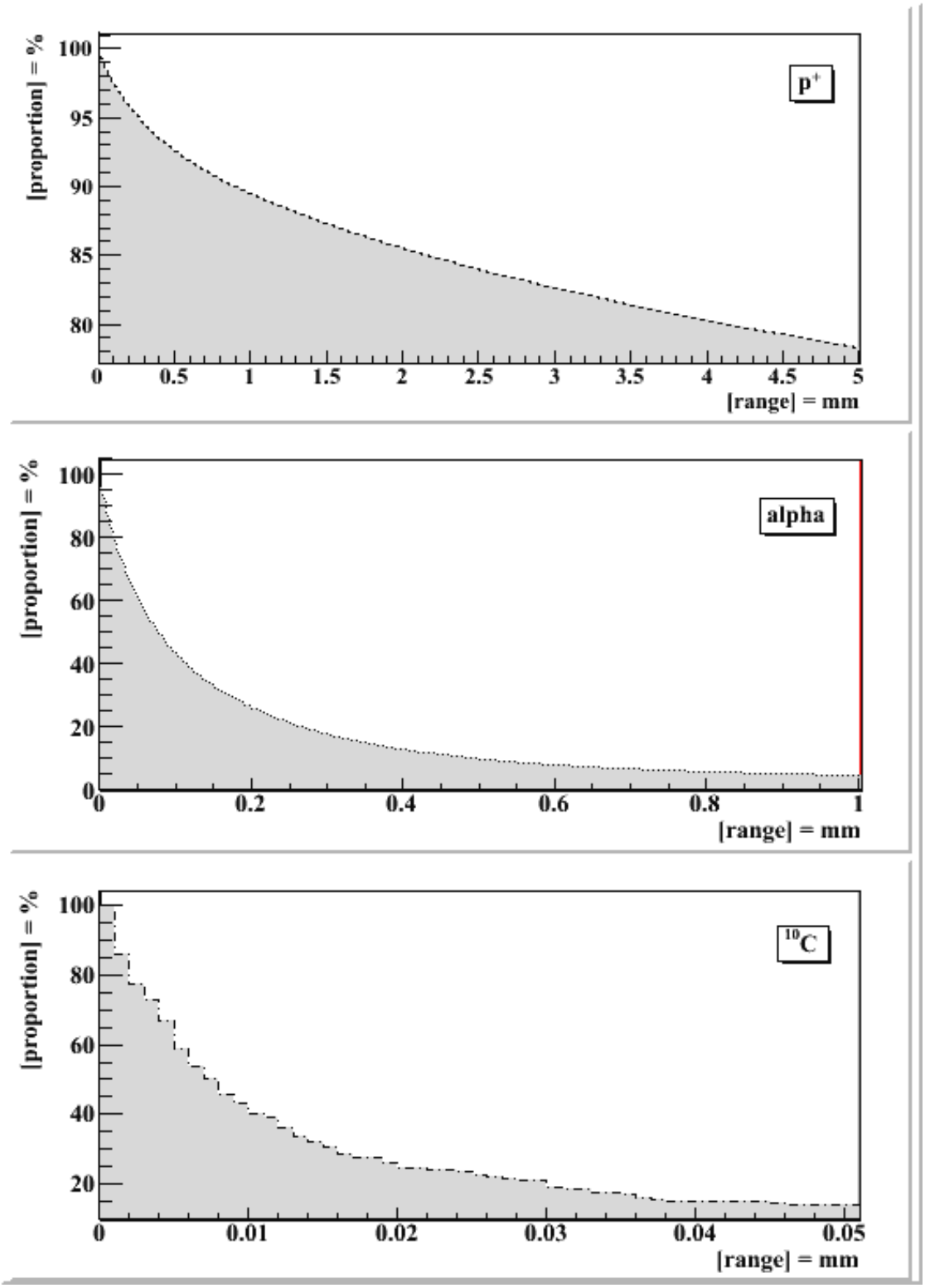

Figure 5.11.: Range of ions of varying mass inside the STOP scintillators. For Example, about 40% of all ^{10}C ions travel as far as 0.01 mm inside the 5 mm thick Stop scintillator. Note: the top and bottom plots are zoomed for better clarity.

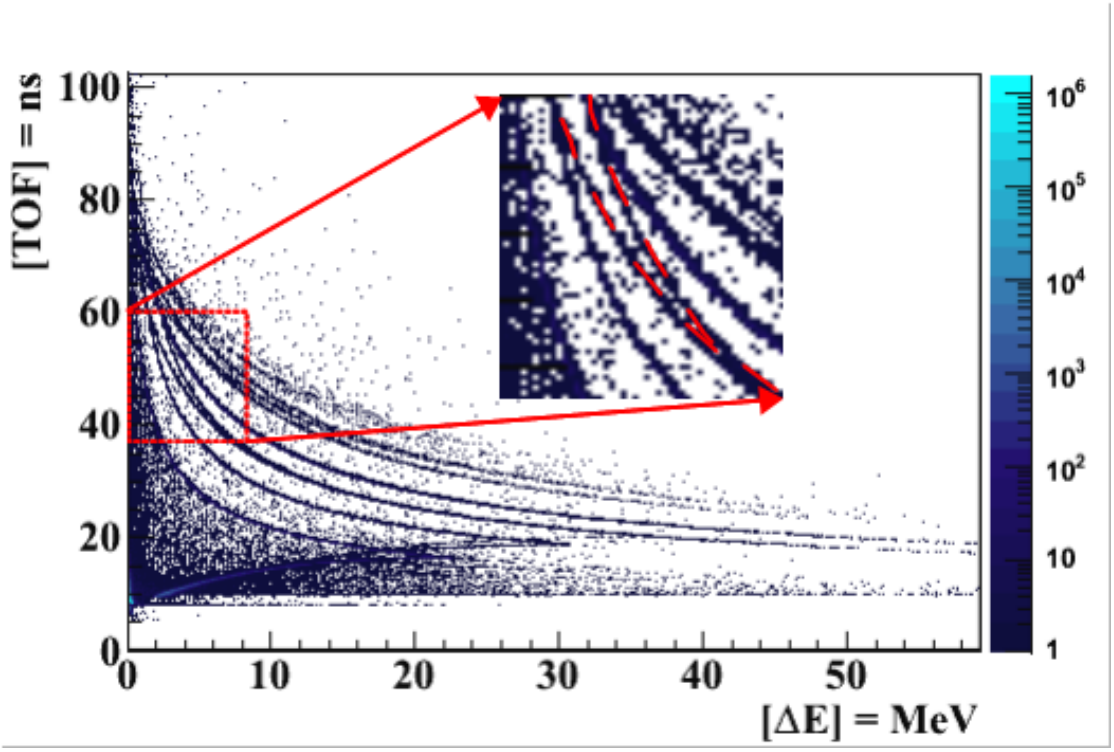

Figure 5.12.: Correlation of time-of-flight vs. energy deposition with the Stop scintillators wrapped in 6 μm thick Mylar® foil.

Several conclusions can be drawn from figure 5.12. First of all, the correlation curves of heavier ions are less pronounced compared to figure 5.4. This means, they loose a considerable amount of their energy within the wrapping which also explains why the correlation curves appear to be compressed towards higher times-of-flight. Some of the slower heavy particles stop within the Mylar® foil so that the corresponding correlations show a cut-off at a certain time-of-flight instead of the usual asymptotic tail. Also, some of the curves seem to split into two diverging parts towards lower energies. This phenomenon is magnified within a box for ions with A = 3 in figure 5.12. Obviously, the correlation curves of He^3 and tritium do not superpose any longer and can be distinguished from each other below a certain energy threshold. Here, the wrapping acts as a thin absorber and since ions of different charge deposit a different amount of energy within it they also deposit different amounts of energy in the Stop scintillator, despite of their equal initial momentum and time-of-flight.

Figure 5.13 shows the corresponding mass spectrum simulated with the Stop detectors wrapped in Mylar®. Compared to figure 5.6, the masses above 4 u are suppressed. This means, the setup with wrapped scintillators can still be used for the purpose of detector commissioning while alternative methods of light signal amplification need to be devised for the actual cross section measurements.

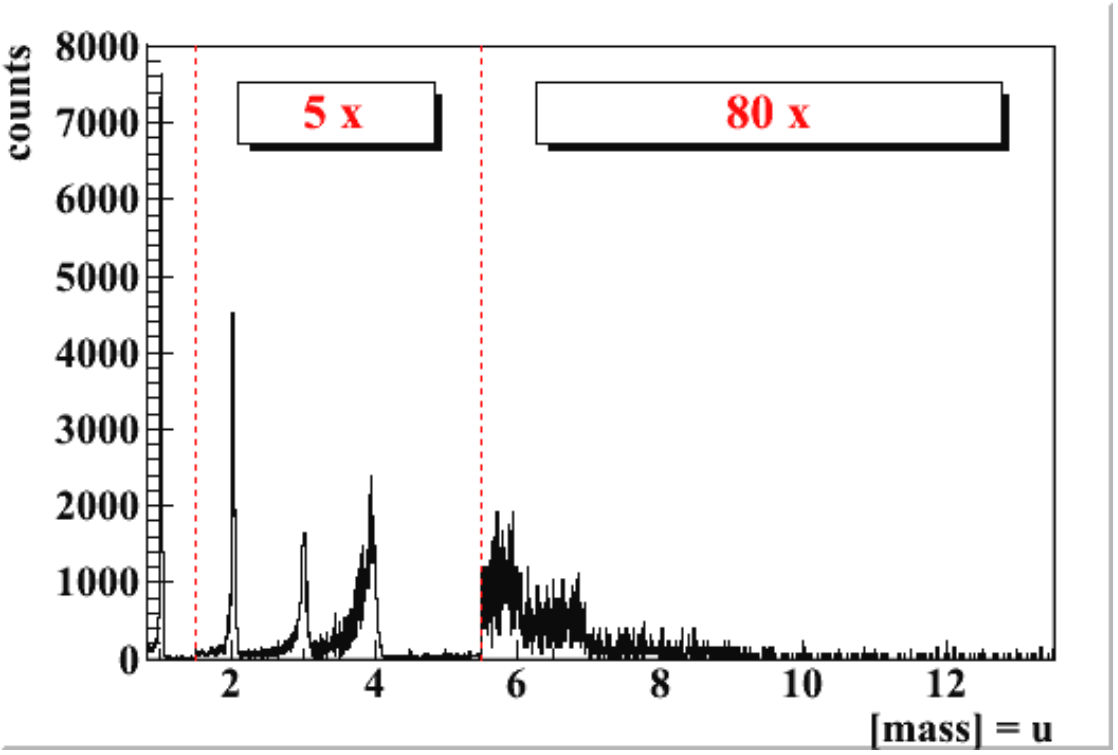

Figure 5.13.: Mass spectrum reconstructed from the correlation in figure 5.12.

6. Experimental data acquisition

This chapter mainly deals with the structure and development of the data acquisition software for the cross section measurements with the time-of-flight spectrometer. As the data acquisition aims to use the same or very similar data structure and format as the GEANT4 simulation, these project parts are closely related. As a foundation for the software concept, section 6.1 offers a brief outline of the electronics and trigger logic developed by the medical physics group of the 3rd Physics Institute. The description of the data acquisition software (DAC) which is part of this dissertation follows in section 6.2.

6.1. Electronics and trigger

During the experiment, the necessary information of time-of-flight and energy deposition are acquired with the help of a Time-to-Digital converter (TDC) and a Charge-to-digital converter (QDC), respectively. Generally speaking, TDC and QDC are very precise analog-to-digital converters (ADCs) with respective Time-to-Amplitude converter sections (TAC) and Charge-to-Amplitude converter sections (QAC) providing the voltage levels. Both of these VME modules are produced by CAEN (TDC V775 and QDC V 965), and can communicate with the readout software via the Wiener VM-USB interface which is part of the crate controller unit.

The Stop scintillators as well as the Start and Veto detectors (see section 4.1) are each equipped with a 3×3 mm SiPM. Connected to the scintillator top face via optical coupling gel they provide a time-of-flight signal for the TDC. In addition, wavelength shifting fibres are glued into grooves machined in the side surfaces of the Stop scintillators and the Start detector. These supply two separate energy deposition signals for the QDC, to be combined offline.

When a primary proton hits the Start scintillator, it produces a scintillation light signal from which the SiPMs generate a corresponding signal for the TDC. The latter opens a gate of 200 ns where the electronics awaits a signal from the Stops with their corresponding TDCs operating in COMMON START mode. If no such signal comes, the gate is closed and the next primary proton creates a new gate. The Veto signal is directed to the FAST CLEAR inputs of the TDC and QDC allowing for the background from the Start detector to be eliminated online. Thus, if no signal is generated by the Veto system and a sufficient light signal is created within at least one of the Stop scintillators, the corresponding TDC records the time-of-flight as a difference between the Start gate and the Stop signal. The QDC integrates the signal it receives from the SiPM preamplifier boards along the entire gate creating so called pedestals when no actual signal occurs.

The preamplifier boards for the SiPMs were manufactured at the RWTH Aachen and were each equipped with a 1wire interface enabling continuous temperature recordings

during data acquisition. These values can be used to correct the temperature sensitive SiPM signals offline. A more detailed description of the trigger logic and electronics can be found in the diploma thesis of Luc Schlömer [Sch09].

6.2. Readout software

The first three parts of this section give an account on the data acquisition software. Section 6.2.3 shows the results of a correlation test with a pulser and the results of a test during a COSY synchrotron run.

6.2.1. Requirements on the DAC

Once the detector is fully equipped with all 20 Stop scintillators, the readout software will have to handle reading more than 40 QDC channels and more than 20 TDC channels while also providing a correlation of corresponding QDC and TDC data. It also has to take care of the initialisation and setup of the VME modules. The user must be equipped with a means to change this configuration and the data must be stored in a format convenient for both, fast data acquisition and versatile data analysis.

Another requirement on the software is that it has a modular structure allowing it to be easily understood by others and partially or entirely modified for further purposes. A group inside the 3rd Physics Institute of the RWTH Aachen has developed a C++ library, called LibLAB, which encapsulates all interactions with the hardware into easily accessible C++ code. It is object oriented, open source, and allows raw data access while wrapping all register access into a user friendly interface/module structure [Lib]. In principle, LibLAB constitutes the link between the DAC and the hardware. The readout software for each individual experiment can thus be developed as a kind of top layer over the LibLAB.

6.2.2. Components of the DAC

Figure 6.1 shows an outline of the solution developed for the experimental data acquisition with the time-of-flight spectrometer. There are several classes involved in the procedure of data taking, each one with its own set of responsibilities and range of functions:

- The Configfile Reader parses the text files which contain the configuration settings for the VME modules. These files contain hardware specific flags and values as described in the according user manuals and can be edited by the user without recompiling the entire code. The Configfile Reader stores the data in the necessary format (i.e. string, double, uint or similar), usually indicated in the configfile, and passes a vector of Configfile Data objects back to main.

- The VME Initialiser takes the vector of Configfile Data objects and calls the corresponding initialiser constructor for each module: VM USB, CAEN V775 TDC, CAEN V965 QDC, and 1wire DS18B20 temperature sensors.

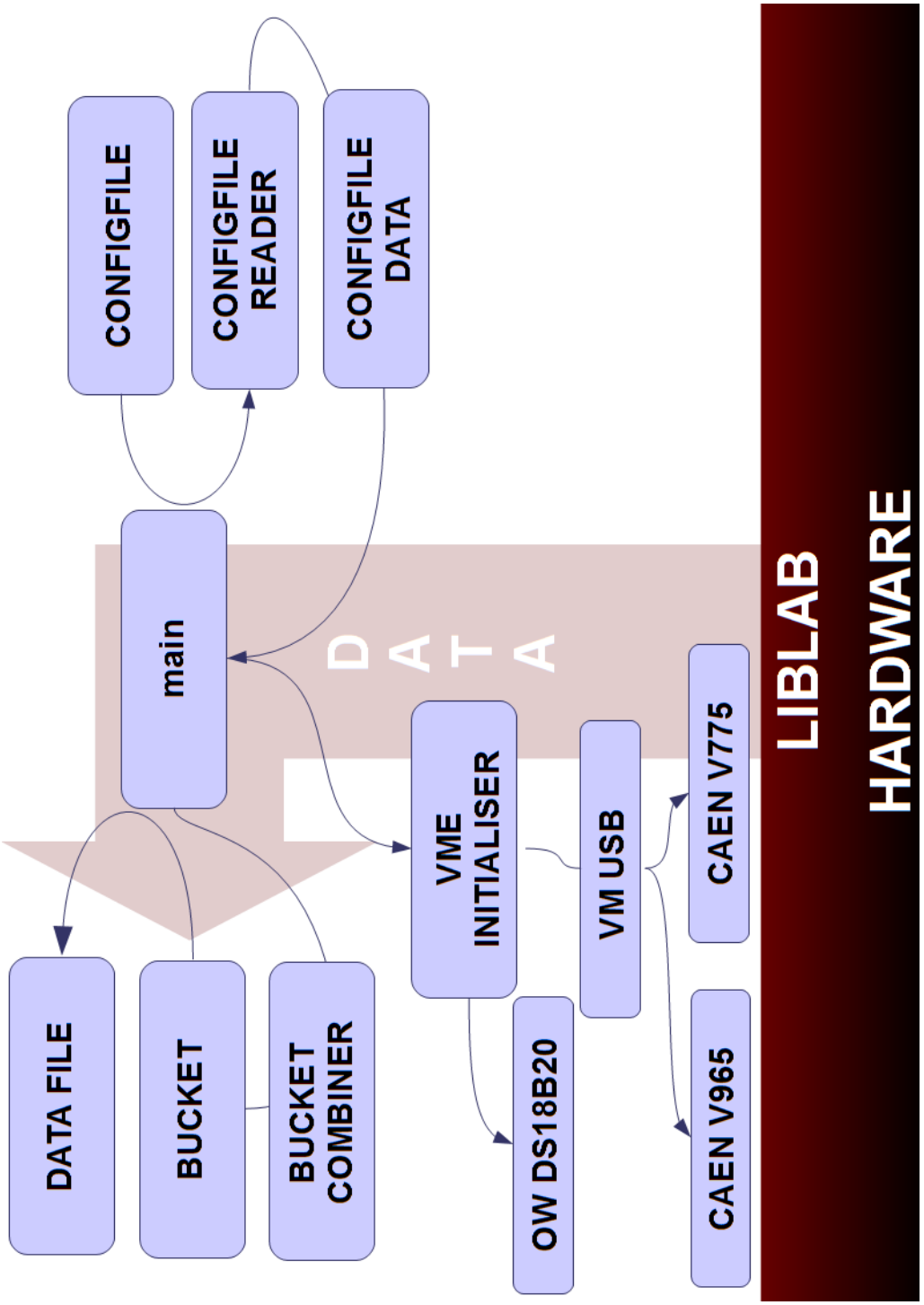

Figure 6.1.: Schematic outline of the readout software project. The wide arrow shows the data flow from the hardware to the data file using LibLAB as an intermediate layer.

These initialisers check the user provided data for validity and, accordingly, either exit with an error message or initialise the modules by making calls to LibLAB objects.

- The class Bucket contains project specific data like the time-of-flight (TDC values), charge acquired from the QDC, event number, as well as a set of Get() and Set() functions. One Bucket object resembles and object of the G4MeasuredData class used in the GEANT4 simulation. Just as an event stored in a G4MEasuredData object is created within a G4Event, a Bucket object is created from signals within a gate, both being generated by a primary proton. Bucket objects are continuously filled and written to a ROOT Tree during data acquisition.

- The Bucket Combiner holds an index of devices which contribute to a Bucket object and maintains a queue in which it fills and sorts buckets according to their event number. This sorting mechanism primarily allows for the blockwise reading of multiple events from the VME modules (Block transfer mode). When a Bucket object is full or too old it is passed back to main, which passes it to a Data File object.

- The Data File holds the ROOT Tree object and takes care of filling this tree and writing it to an output file. A new output file is created every minute to avoid large files and allow the user to access new data while the acquisition is still running.

- An additional thread takes care of continuous temperature readings and the Data File object writes one set of up-to-date temperatures into each output file.

6.2.3. Tests of the DAC

Pulser experiment

The pulser experiment represents a test of the DAC in several ways. It not only serves to test the initialisation of the TDC and QDC modules, but also the readout of data from the buffers of the VME modules, and, ultimately, the correlation of TDC and QDC data.

Two identical pulses were generated with the four channel digital delay/pulse generator (model DG535 Stanford Research Systems Inc.). One of these pulses was used as a gate signal for both, the CAEN V775 TDC and the CAEN V965 QDC and the other signal was used to generate a stop signal for the TDC and a signal for the QDC which started the integration process.

During data acquisition, the second signal was shifted manually with respect to the gate, thus increasing the time measured by the TDC and decreasing the signal over which the QDC integrated. This way, a linear correlation of the two signals with a negative slope was obtained and is shown in figure 6.2. The pulses were generated with a frequency of 1 kHz.

The regularly distributed additional values on both sides of the correlation line stem from pulses created by the DG535 during manual delay switching. Altogether, this test shows a good performance of the data acquisition.

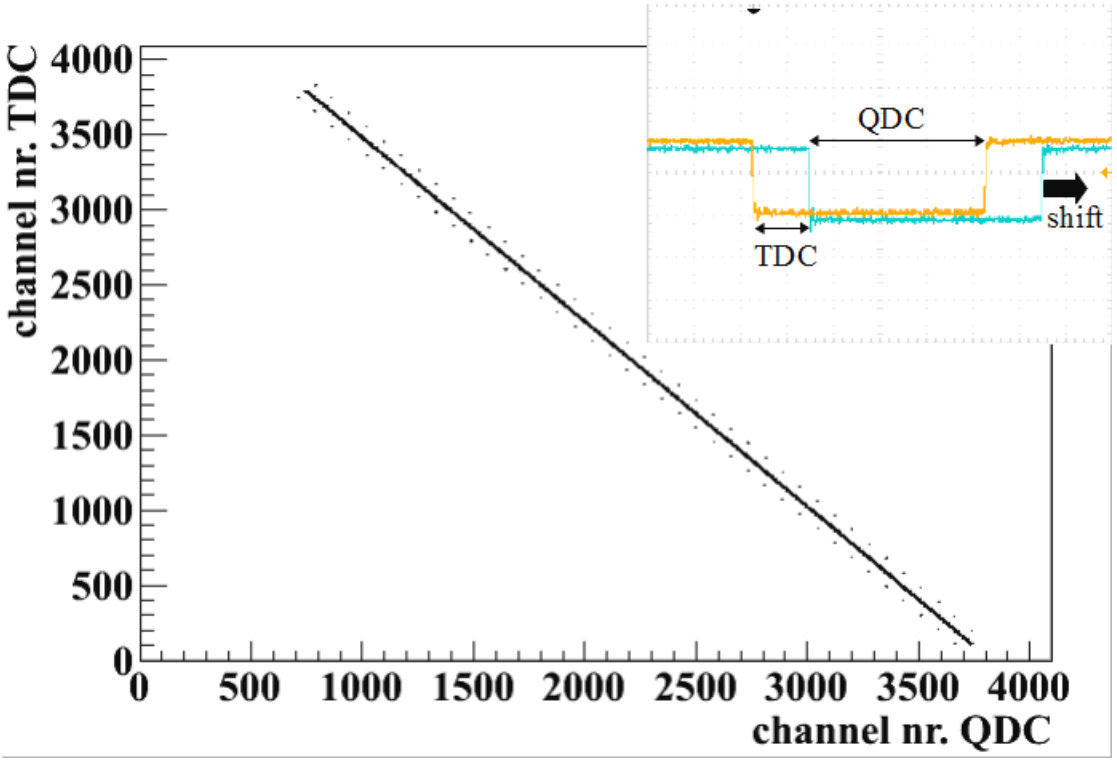

Figure 6.2.: Correlation of pulser signals sent to the QDC and TDC modules. The scope screenshot of the two pulses is shown in the top right corner.

COSY detector tests

In the first week of June 2010 three nights and one weekend of beam time were allotted for detector commissioning at the COSY synchrotron at the Forschungszentrum Jülich. After testing the trigger scheme and different hardware settings (CFD[1] thresholds, FCLR[2] inputs of the VME modules) several measurements of a few hours duration each, and one long measurement over the weekend were acquired.

The hardware configuration employed during this experimental run was a preliminary subset of the planned final setup. The main focus was on the performance of the scintillation detectors and the data acquisition software rather than actual cross section measurements. Only six STOP scintillators were employed and the remaining fourteen slots were sealed by blind flanges. Also, only one of the VETO scintillators was used - the second when counting along the beam direction.

Since the Jessica experiment site of COSY lacks the necessary quadrupoles and none were installed for these initial detector tests, the lateral width of the proton beam hitting the START detector amounted to several centimetres FWHM. Protons with an energy of 200 MeV were supplied continuously within an extraction cycle of 12 s.

One of the main aims of the data acquisition software has been the proper merging and correlation of TDC and QDC events. A first evaluation of the data has shown no visible

[1] Constant Fraction Discriminator
[2] Fast Clear

correlation of time-of-flight versus energy deposition, even for elastically scattered fast protons which form the lower left part of the correlation curve in figure 5.3. A successive evaluation of the rate of full Buckets containing TDC and QDC data compared to half full Buckets holding either QDC or TDC has indeed shown, that most acquired events are of the second type, i.e. they are not complete. Figure 6.3 shows two histograms which illustrate this observation.

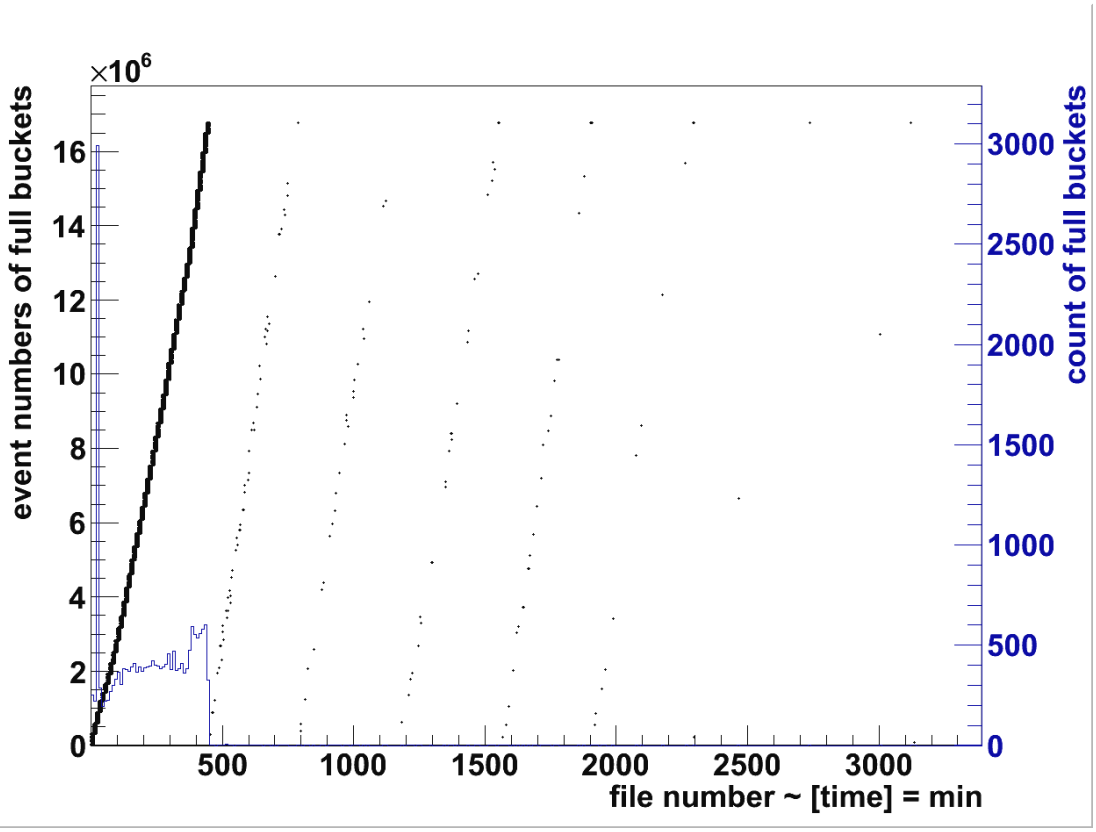

Figure 6.3.: Event numbers of complete events (left axis) are plotted in black against file numbers. Since approximately one file per minute has been acquired, the x-axis also represents a time scale. The blue diagram depicts the number of full events in each file thus representing a projection of the 2D black diagram onto the x-axis.

It is remarkable, how the number of full buckets per file drops down to zero at the same point when the event number of full Buckets reaches $2^{24} = 16777216$. This event number corresponds to an internal 24 Bit event counter value of the QDC and TDC. For the data acquisition to run properly these event counters need to be synchronized. At the stage of this experimental run, the counters of both VME modules had been set to zero during initialisation and no further measures were taken to synchronise the counters or even check their synchronisation during run time.

Since the event counters are stored within 24 Bits in one of the registers of the VME modules they will overflow after 2^{24} events have been acquired. A certain desynchronisation can be observed from the start, but it drastically increases after each counter overflow as shown in figure 6.3.

So far, this artifact could be reproduced under laboratory conditions using a pulse generator and the same setup as in the pulser experiment. In later tests, the part of the program responsible for temperature recordings had been switched off and even at higher frequencies of several MHz no such strong divergence of event numbers could be observed.

As a matter of fact, since the temperature acquisition via the 1wire bus is relatively slow, the main was halted for 30 s prior to data acquisition to allow for the temperature thread to read a full set of temperatures. This procedure took place after the initialiser classes reset the TDC and QDC modules, thus presumably facilitating the divergence of event counters and loss of events during the initial 30 s of the data acquisition process.

In future, additional measures will be applied to ensure the synchronisation of the event counters. For one, a so called "multi cast" option has been introduced to the LibLAB which allows to reset the counters for all VME modules placed in the same crate simultaneously. Also, new output files will be created according to the spill cycle every 12 s rather than every minute.

7. Conclusions

A comprehensive GEANT4 simulation of the time-of-flight spectrometer including an 0.075 mm graphite target has been implemented in this study. The results have shown that light and heavy target fragments reach the Stop scintillators and are available for detection using the implemented design. Heavier particles deposit up to 40 MeV energy and exhibit time-of-flight values up to 400 ns, although values higher than 200 ns correspond to very slow particles and a rather small energy deposition which is unlikely to produce a sufficient number of photons to be picked up by the SiPMs mounted on the Stop scintillators.

The simulation of scintillation processes and photon yield itself is outside the scope of this thesis. Mainly, it was omitted due to the lack of necessary measurements and ambiguities in the implementation and insufficient documentation of the process inside the GEANT4 toolkit. Since the scintillation yield has to be input in the simulation as a parameter, it has to be measured for at least one particle type beforehand. According to their Birks factors the scintillation yields then need to be adjusted and defined separately for each particle type.

It could also be shown that the background from the Start detector can be effectively separated from detector events created by nuclear reactions in the target with the help of the Veto system.

Due to their low energy, most of the heavy target fragments have a range lower than 50 μm inside the Stop scintillators which is 1% of their thickness. On the one hand, this means that the correlation curves for ions of equal mass number superpose. Thus, by the identification of heavy target fragments alone only inclusive cross sections can be measured. On the other hand, even if the Stop scintillators were made thin enough to allow for the heavier particles to pass through many other particles, e.g. fast protons, would not produce enough light to create a detectable signal.

In principle, the distinction of individual reaction channels might be possible even under such constraints provided that the other particles in the output channel are detected as well. However, these events are relatively rare occurring in only about 6% of all nuclear reaction events with Stop hits.

Provided that the pressure in the detector chamber is kept at 0.1 mbar or less an adequate mass reconstruction can be achieved. The optimisation of the energy resolution might prove challenging due to quenching effects combined with the low range of target fragments inside the scintillators. Currently, pure, undoped Cesium Iodide (CsI) is under investigation as an alternative to plastic scintillator material.

Since the target thickness shows a relatively high impact on the energy of the secondary particles, thinner targets will be employed in future measurements.

The simulation with Mylar® wrapped stop scintillators has shown that the wrapping is obstructive to the detection of heavier target fragments. However, fast protons and ions with $A \leq 4$ are less affected with respect to their mass spectra so that the setup can very effectively be employed for the commissioning of electronics and readout software.

The first tests of the detector with the new data acquisition software have shown an aberration in the process of synchronised correlation of time-of-flight and energy deposition events. The source has been found and recent tests show improved behaviour of the code.

Acknowledgements

Over the last three and a half years I have received considerable professional, financial and moral support from individuals within the phase space (RWTH Department of Physics) and outside in the real world. To these people I would like to express my heartfelt gratitude.

First and foremost I thank my supervisor Prof. Achim Stahl for accepting me into his medical physics group and giving me the opportunity to work on Monte Carlo simulations in particle therapy which, even after all those years and struggles, remains one of my favourite playgrounds. Through all this time he regularly kept in close contact and properly guided me giving many helpful impulses. His confidence, humour and the ability to keep his cool in all circumstances make him one of the best supervisors I ever had.

Many thanks to my second adviser Prof. Michael J. Eble for cooperating with us in validating GEANT4 for particle therapy and for his beautiful contribution to our "Workshop on Nuclear Models for Hadron Therapy" which took place at the Forschungszentrum Jülich in 2009.

Dr. Bernd Schweizer, who has supervised me on behalf of Philips Research Aachen, I thank for his lively interest in my work and for providing new viewpoints on multiple issues during our meetings. At this point I would also like to thank Philips Research Aachen for their financial support which made it possible for me to invest more than 80% of my time into my thesis.

I would like to thank Dr. Sven Lotze for his notorious attention to detail - it was this gift, which you rarely find so pronounced in one person, that helped me in situations like "Damn, I know there is a mistake here somewhere... but I don't see it even after having checked a hundred times!". I also thank him for going the extra step in taking care of the team and our common project instead of just making do with the usual amount of responsibility.

Many thanks to all other players on the G4RT team including Jan Hermes, Nuria Escobar Corral, Felix Bachmair, Carolin Bornemann, Luc Schlömer, Kathrin Gester, Ronja Lewke, Paul Fiedler, Christian Salmagne, Gisela Hürtgen, Eva Kreysing, Alexander Mantz, Raphael Krause and Martin Engels. I very much enjoyed working in this young and dynamic group and am looking forward to future results and to our next barbecue!

Thanks to people at COSY and IKP (FZ Jülich) for giving us beam time and or-

ganising the Nuclear Models in Hadron Therapy workshop in 2009. Thanks to Dennis Terhorst and Lukas Middendorf, main developers of the LibLAB code, for strategic discussions and practical advice.

Next, I would like to say thank you to all people who gave me moral and emotional support in their respective native languages:

Ich kreuze zunächst die Arme auf der Brust und bedanke mich bei Dennis, Jan und Adriana für die vielen Dienstagabende, an denen wir vielen angestaubten Sci-Fi flicks neues Leben eingehaucht haben. Wann kommt denn dieses automatische Zeitalter? Mittwoch!

Danke an Thomas Kress für die zwei Tage Ski-Unterricht 2009 in Saas Grund. Dieses Seminar war eine selten gute Gelegenheit, meine Kollegen in einer anderen Situation kennen und schätzen zu lernen. Ich danke Dr. Harald Grothe für seine schnelle Hilfe in Krisenzeiten und seine Unterstützung bei meiner persönlichen Entwicklung.

Спасибо режиссёру Татьяне Юраковой за то, что дала мне возможность в первый раз поучавствовать в театральной постановке. Спасибо так же за требовательные, интересные и вдохновляющие занятия.

Спасибо Олегу Цыгенову за многочисленные разоблачения моих профессиональных и жизненных анекдотов, замаскировавшихся заботами и огорчениями. Спасибо так же Вовке Черепанову за дискуссии на тему детекторной физики, которые помогли мне на экзамене.

Моих близких подруг, Лену Шмидт и Викторию Шиллер я благодарю за душевную поддержку и за то, что несмотря на все жизненные трудности и расстояние, они остались моими близкими сопутницами.

Больше всего, я благодарю моих родителей за то, что они всегда поддерживают меня и за то, что так высоко ценят моё образование, отдав за него очень многое. Спасибо за ваше доверие и помощь.

Bibliography

[AAA+03] S. Agostinelli, J. Allison, K. Amako *et al.*, "Geant4 - a simulation toolkit," *Nuclear Instruments and Methods in Physics Research A*, vol. 506, pp. 250–303, 2003.

[AKK+07] T. Aso, A. Kimura, S. Kameoka, K. Murakami, T. Sasaki, and T. Yamashita, "GEANT4 based simulation framework for particle therapy system," in *IEEE Nuclear Science Symposium*, 2007, pp. 2564–2567.

[ARB72] J. Ashley, R. Ritchie, and W. Brandt, "Z_1^3 effect in the stopping power of matter for charged particles," *Physical Review B*, vol. 5, no. 7, pp. 2393–2397, 1972.

[BDF+06] P. Buzhan, B. Dolgoshein, L. Filatov, A. Ilyin, V. Kaplin, A. Karakash, S. Klemin, R. Mirzoyan, A. Otte, E. Popova, V. Sosnovtsev, and M. Teshimac, "Large area silicon photomultipliers: Performance and applications," *Nuclear Instruments and Methods in Physics Research A*, vol. 567, pp. 78–82, 2006.

[BDI+01] P. Buzhan, B. Dolgoshein, A. Ilyin, V. Kantserov, V. Kaplin, A. Karakash, A. Pleshko, E. Popova, S. Smirnov, Y. Volkov, L. Filatov, S. Klemin, and F. Kayumov, "An advanced study of silicon photomultiplier," *ICFA Instrumentation Bulletin*, vol. 23, pp. 1–14, 2001.

[BGG+04] H. Burkhardt, V. M. Grichine, P. Gumplinger, V. N. Ivanchenko, R. P. Kokoulin, M. Maire, and L. Urban, "GEANT4 standard electromagnetic package for hep applications," in *IEEE Nuclear Science Symposium Conference Record*, 2004.

[BIM+87] A. S. Botvina, A. S. Iljinov, I. N. Mishustin, J. P. Bondorf, R. Donangelo, and K. Sneppen, "Statistical simulation of the break-up of highly excited nuclei," *Nuclear Physics A*, vol. 475, pp. 663–686, 1987.

[BWW08] K. Bethge, G. Walter, and B. Wiedemann, *Kernphysik*. Springer, 2008.

[Can] [Online]. Available: http://info.cancerresearchuk.org/cancerstats/world/

[Car95] D. S. Carman, "Inclusive and exclusive quasifree (p,Np) reaction studies from ^{2}H and ^{12}C at 200 MeV," Ph.D. dissertation, Indiana Unicersity Cyclotron Facility, 1995.

[CBC+99] D. S. Carman, L. C. Bland, N. S. Chant, T. Gu, G. M. Huber, J. Huffman, A. Klyachko, B. C. Markham, P. G. Roos, P. Schwandt, and K. Solberg, "Quasifree inclusive and exclusive cross sections at 200 MeV," *Physics Letters B*, vol. 452, pp. 8–14, April 1999.

[CCCR07] V. Chmill, M. Caccia, C. Cappellini, and F. Risigo, "Silicon photo multipliers characterisation: recent achievements and latest results. Investigation of SiPM for photon counting applications." in *WSPC - Proceedings*, December 2007.

[CCG+05] G. A. P. Cirrone, G. Cuttone, S. Guatelli, S. L. Nigro, B. Mascialino, M. G. Pia, L. Raffaele, G. Russo, and M. G. Sabini, "Implementation of a new Monte Carlo-GEANT4 simulation tool for the development of a proton therapy beam line and verification of the related dose distributions," *IEEE Transactions on Nuclear Science*, vol. 52, no. 1, pp. 262–265, February 2005.

[CCL+04] G. Cirrone, G. Cuttone, P. Lojacono, S. L. Nigro, V. Mongelli, I. Patti, G. Privitera, L. Raffaele, D. Rifuggiato, M. Sabini, V. Salamone, C. Spatola, and L. Valastro, "A 62 *MeV* proton beam for the treatment of ocular melanoma at laboratori nazionali del Sud-INFN (CATANIA)," *IEEE Transactions on Nuclear Science*, vol. 51, no. 3, pp. 860–865, 2004.

[DBB+06] B. Dolgoshein, V. Balagura, P. Buzhan, M. Danilov, L. Filatov, E. Garutti, M. Groll, A. Ilyin, V. Kantserov, V. Kaplin, A. Karakash, F. Kayumov, S. Klemin, V. Korbel, H. Meyer, R. Mizuk, V. Morgunov, E. Novikov, P. Pakhlov, E. Popova, V. Rusinov, F. Sefkow, E. Tarkovsky, I. Tikhomirov, and C. Collaboration, "Status report on silicon photomultiplier development and its applications," *Nuclear Instruments and Methods in Physics Research A*, vol. 563, pp. 368–376, 2006.

[DBMT09] D. Dauvergne, M. Battaglia, G. Montarou, and E. Testa, "New methods of real-time control imaging for ion therapy," February 2009. [Online]. Available: http://hal.in2p3.fr/docs/00/36/33/82/PDF/NIRS-ETOILE_Dauvergne.pdf

[DF59] I. Dostrovsky and Z. Fraenkel, "Monte carlo calculations of nuclear evaporation processes," *Physical Review*, vol. 116, no. 3, pp. 683–702, November 1959.

[EaRRL06] S. A. Enger, P. M. af Rosenschöld, A. Rezaei, and H. Lundqvist, "Monte Carlo calculations of thermal neutron capture in gadolinium: A comparison of GEANT4 and MCNP with measurements," *Medical Physics*, vol. 33, pp. 337–341, 2006.

[ENS] [Online]. Available: http://www.nndc.bnl.gov/nds/index.html

[FBH08] Y. Feng, J. Baciak, and A. Haghighat, "A design of Compton Cameras for imaging gamma emission in proton therapy," in *50th AAPM Annual Meeting*. Houston, Texas: The American Association of Physicists in Medicine, July 2008.

[Fer50] E. Fermi, "High energy nuclear events," *Progress of theoretical physics*, vol. 5, pp. 570–583, 1950.

[FFR+03] A. Fasso', A. Ferrari, S. Roesler, J. Ranft, P. Sala, G. Battistoni, M. Campanella, F. Cerutti, L. Biaggi, E. Gadioli, M. Garzelli, F. Ballarini, A. Ottolenghi, D. Scannicchio, M. Carboni, M. Pelliccioni, R. Villari, V. Andersen, A. Empl, K. Lee, L. Pinsky, T. Wilson, and N. Zapp, "The FLUKA code: present applications and future developments," 2003, computing in High Energy and Nuclear Physics (CHEP03).

[Fie09] P. Fiedle, "Test von Szintillator-Modulen mit SiPM-Auslese für ein Flugzeitspektrometer: Zeitauflösung," 2009, bachelorthesis, RWTH Aachen.

[FIW04] G. Folger, V. Ivanchenko, and J. Wellisch, "The binary cascade," *European Physics Journal A*, vol. 21, pp. 407–417, September 2004.

[Fur00] S. Furihata, "Statistical analysis of light fragment production from medium energy proton-induced reactions," *Nuclear Instruments and Methods in Physics Research B*, vol. 171, pp. 251–258, 2000.

[GP60] T. Gooding and H. Pugh, "Quasi-elastic scattering of 153MeV protons by p-state protons in ^{12}C," *Nuclear Physics*, vol. 18, pp. 46–64, 1960.

[GSA+04] I. Gudowska, N. Sobolevsky, P. Andreo, D. Belkic, and A. Brahme, "Ion beam transport in tissue-like media using the Monte Carlo code SHIELD-HIT," *Physics in Medicine and Biology*, vol. 49, pp. 1933–1958, 2004.

[Hol05] N. E. Holden, "A short history of CSISRS," December 2005, national Nuclear Data Center, Brookhaven National Laboratory.

[HSJP09] K. Henkner, N. Sobolevsky, O. J"akel, and H. Paganetti, "Test of the nuclear interaction model in SHIELD-HIT and comparison to energy distributions from GEANT4," *Phyics in Medicine and Biology*, vol. 54, pp. 509–517, 2009.

[INN02] H. Iwase, K. Niita, and T. Nakamura, "Development of general-purpose particle and heavy ion transport Monte Carlo code," *Journal of Nuclear Science and Technology*, vol. 39, no. 11, pp. 1142–1151, November 2002.

[JP04] H. Jiang and H. Paganetti, "Adaptation of GEANT4 to Monte Carlo dose calculations based on CT data," *Medical Physics*, vol. 31, pp. 2811–2818, 2004.

[JP08] C. Z. Jarlskog and H. Paganetti, "Physics settings for using the GEANT4 toolkit in proton therapy," *IEEE Transactions on Nuclear Science*, vol. 55, no. 3, June 2008, iEEE Proof (version not yet published).

[JSP07] H. Jiang, J. Seco, and H. Paganetti, "Effects of Houndsfield number conversion on CT based Monte Carlo dose calculations," *Medical Physics*, vol. 34, no. 4, pp. 1439–1449, April 2007.

[Kac07] A. Kacperek, "Dose verification by activation in vivo following proton beam eye radiotherapy," *Journal of Radioanalytical and Nuclear Chemistry*, vol. 271, no. 3, pp. 731–740, 2007.

[KD03] V. Kamerdzhiev and J. Dietrich, "Ionisation beam profile monitor at the Cooler Synchrotron COSY-Juelich." Mainz, Germany: DIPAC, 2003.

[KMR02] B. Kozlovsky, R. J. Murphy, and R. Ramaty, "Nuclear deexcitation gamma-ray lines from accelerated particle interactions," *The Astrophysical Journal Supplement Series*, vol. 141, pp. 523–541, August 2002.

[Koi06] T. Koi, "Thermal neutron scattering from nuclei within chemically bound atoms in GEANT4," in *IEEE Nuclear Science Symposium and Medical Imaging Conference*, 2006.

[KPT08] S. Karkar, N. Pauna, and E. Testa, "State of the art and next challenges in instrumentation for quality control in hadrontherapy centres," May 2008, INNOTEP collaboration.

[Lab] L. A. N. Laboratory, "Code comparison chart for all-particle Monte Carlo transport codes," lA-UR-06-6637.

[LB09] D. P. Landau and K. Binder, *A guide to Monte Carlo simulations in statistical physics*. Cambridge University Press, 2009.

[Lew50] H. W. Lewis, "Multiple scattering in an infinite medium," *Physical Review*, vol. 78, no. 5, pp. 526–529, June 1950.

[Lib] As of 2011 restricted to internal access by members of the RWTH Aachen Physics Department. [Online]. Available: liblab.physik.rwth-aachen.de

[McK09] G. W. McKinney, "Physics and algorithm enhancements for a validated MCNPX Monte Carlo simulation tool," 2009.

[MK79] T. Mayer-Kuckuk, *Kernphysik*. Teubner Studienbücher, 1979.

[MKYK06] C.-H. Min, C. H. Kim, M.-Y. Youn, and J.-W. Kim, "Prompt gamma measurements for locating the dose falloff region in the proton therapy," *Applied Physics Letters*, vol. 89, November 2006.

[NG10] K. Nakamura and P. D. Group, "Review of particle physics," *Journal of Physics G: Nuclear and Particle Physics*, vol. 37, pp. 1–3, 2010. [Online]. Available: http://iopscience.iop.org/0954-3899/37/7A/075021

[NNH+05] H. Nose, K. Niita, M. Hara, K. Uematsu, O. Azuma, Y. Miyauchi, M. Komori, and T. Kanai, "Improvement of three-dimensional Monte Carlo code PHITS for heavy ion therapy," *Journal of Nuclear Science and Technology*, vol. 42, no. 2, pp. 250–255, February 2005.

[Nuc] [Online]. Available: http://atom.kaeri.re.kr/

[Par04] K. Parodi, "On the feasibility of dose quantification with in-beam PET data in radiotherapy with ^{12}C and proton beams," Ph.D. dissertation, Dresden University, 2004.

[PBl+10] M. G. Pia, M. Begalli, A. lechner, L. Quintieri, and P. Saracco, "Physics-related epistemic uncertainties in proton depth does simulation," 2010, to be published in IEEE Trans. Nucl. Sci.

[PG03] H. Paganetti and B. Gottschalk, "Test of GEANT3 and GEANT4 nuclear models for 160 MeV protons stopping in CH_2," *Medical Physics*, vol. 30, pp. 1926–1931, 2003.

[Phy08] *GEANT4 Physics Reference Manual*, December 2008, version geant4 9.2.

[PJLK04] H. Paganetti, H. Jiang, S.-Y. Lee, and H. Kooy, "Accurate Monte Carlo simulations for nozzle design, commisioning, and quality assurance in proton radiation therapy," *Medical Physics*, vol. 31, pp. 2107–2118, 2004.

[PLMG07] I. Pshenichnov, A. Larionov, I. Mishustin, and W. Greiner, "PET monitoring of cancer therapy with ^{3}He and ^{12}C beams: a study with the GEANT4 tootlkit," *Physics in Medicine and Biology*, vol. 52, no. 24, pp. 7295–7312, December 2007.

[PMG05] I. Pshenichnov, I. Mishustin, and W. Greiner, "Neutrons from fragmentation of light nuclei in tissue-like media: a study with GEANT4 toolkit," *Physics in Medicine and Biology*, vol. 50, no. 23, pp. 5493–5507, December 2005.

[PMG06] ——, "Distributions of positron-emitting nuclei in proton and carbon-ion therapy studied with GEANT4," *Physics in Medicine and Biology*, vol. 51, no. 23, pp. 6099–6112, December 2006.

[PMG07] ——, "MCHIT - Monte Carlo model for proton and heavy-ion therapy," in *International Conference on Nuclear Data for Science and Technology*, April 2007.

[PMG08] ——, "Comparative study of depth-dose distributions for beams of light and heavy nuclei in tissue-like media," *Nuclear Instruments and Methods in Physics Research Section B: Beam Interactions with Materials and Atoms*, vol. 266, no. 7, pp. 1094–1098, April 2008.

[PPC+09] J. Polf, S. Peterson, G. Ciangaru, M. Gillin, and S. Beddar, "Prompt gamma-ray emission from biological tissues during proton irradiation: a preliminary study," *Physics in Medicine and Biology*, vol. 54, pp. 731–743, January 2009.

[PTVF88] W. H. Press, S. A. Teukolsky, W. T. Vetterling, and B. P. Flannery, *Numerical Recipes in C*, 2nd ed. Cambridge University Press, 1988.

[PV05] E. Poon and F. Verhaegen, "Accuracy of the photon and electron physics in GEANT4 for radiotherapy applications," *Medical Physics*, vol. 32, no. 6, pp. 1696–1711, June 2005.

[Que09] J. M. Quesada, "Nuclear Models in GEANT4," October 2009, talk at the Workshop on Nuclear Models for use in Hadron Therapy, Jülich.

[SAI] [Online]. Available: http://gwdac.phys.gwu.edu/

[Sai05] *BC-418, BC-420, BC-422 premium plastic scintillators*, Saint-Gobain Ceramics & Plastics, Inc., August 2005, data sheet. [Online]. Available: http://www.detectors.saint-gobain.com/uploadedFiles/SGdetectors/Documents/Product_Data_Sheets/BC418-420-422-Data-Sheet.pdf

[Sal09] C. Salmagne, "Test von Szintillator-Modulen mit SiPM-Auslese für ein Flugzeitspektrometer: Energiemessung," 2009, bachelorthesis, RWTH Aachen.

[SBG06] W. Schlegel, T. Bortfeld, and A.-L. Grosu, Eds., *New Technologies in Radiation Oncology*. Springer, 2006.

[Sch09] L. L. A. Schlömer, "Planung und Aufbau eines Flugzeitspektrometers zur Messung von inelastischen Kernreaktionen für die Teilchentherapie," Master's thesis, RWTH Aachen, 2009.

[SST+07] G. Santin, S. Staelens, R. Taschereau, P. Descourt, C. Schmidtlein, L. Simon, D. Visvikis, S. Jan, and I. Buvat, "Evolution of the GATE project: new results and developments," *Nuclear Physics B*, vol. 172, pp. 101–103, 2007.

[Urb02] L. Urban, "Multiple scattering model in GEANT4," *CERN-OPEN*, vol. 70, pp. 1–14, 2002.

[Urb06] ——, "A model for multiple scattering in GEANT4," *CERN-OPEN*, vol. 77, pp. 1–18, December 2006.

[WDW06] M. Wannenmacher, J. Debus, and F. Wenz, Eds., *Strahlentherapie*. Springer, 2006.

[WKF+06] D. H. Wright, T. Koi, G. Folger, V. Ivantchenko, M. Kossov, N. Starkov, A. Heikkinen, and H.-P. Wellisch, "Recent developments and validations in GEANT4 hadronic physics," in *12th International Conference on Calorimetry in High Energy Physics (CALOR 06)*, Chicago, June 2006.

A. Energy deposition from nuclear fragments: example simulation

In this chapter, a simple example simulation is presented which allows to illustrate the role of nuclear reactions in the energy deposition of a proton beam in water.

The same water phantom geometry has been employed as described in chapter 2. A beam of 9×10^5 150 MeV protons has been shot at the target volume. The absolute energy deposition and the energy deposited by secondary particles created in nuclear reactions have been acquired from the Stepping Action and stored in two separate histograms. Figure A.1 hows the Bragg curve (as the absolute energy deposition) and the nuclear energy contribution.

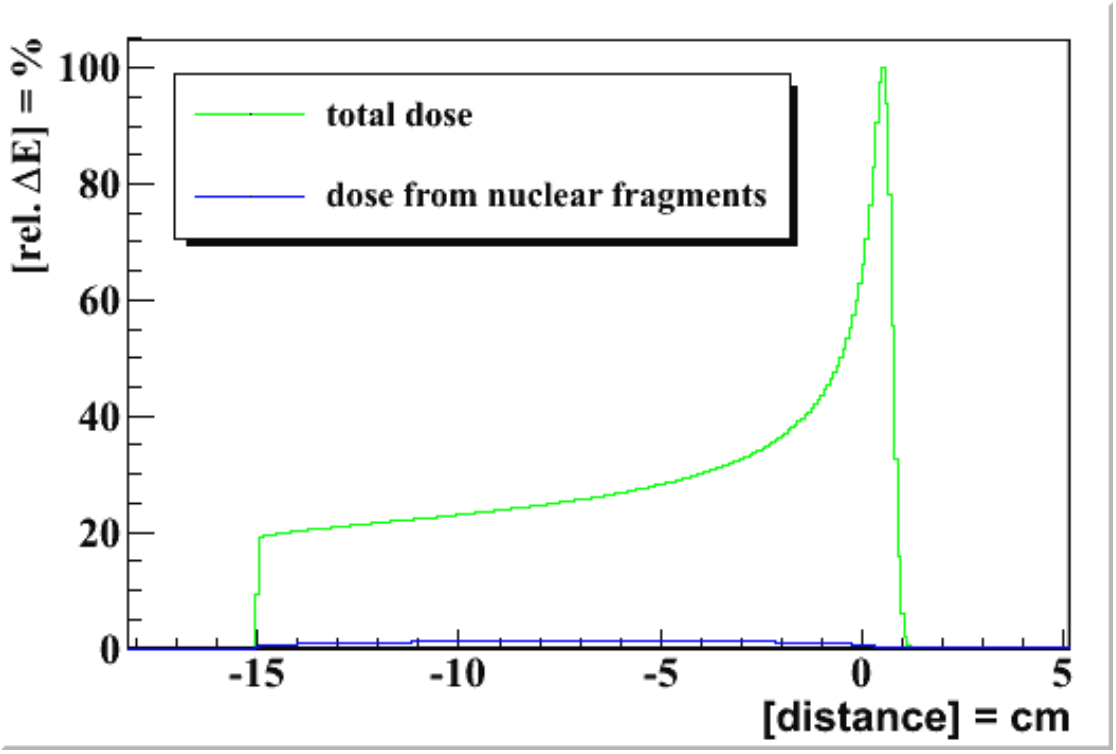

Figure A.1.: Energy deposited by secondary particles from nuclear reactions and absolute energy deposition inside the water phantom. The energy deposition values have been normalised with respect to the Bragg peak.

Figure A.2 shows the ratio between the nuclear energy deposition and the absolute energy deposition. Apparently, the energy deposition contributed by secondaries from nuclear reactions reaches up to ≈5 % of the absolute energy deposition in the entry

region of the Bragg curve. The higher contributions behind the Bragg peak do not play any significant role because the absolute energy deposition is practically zero.

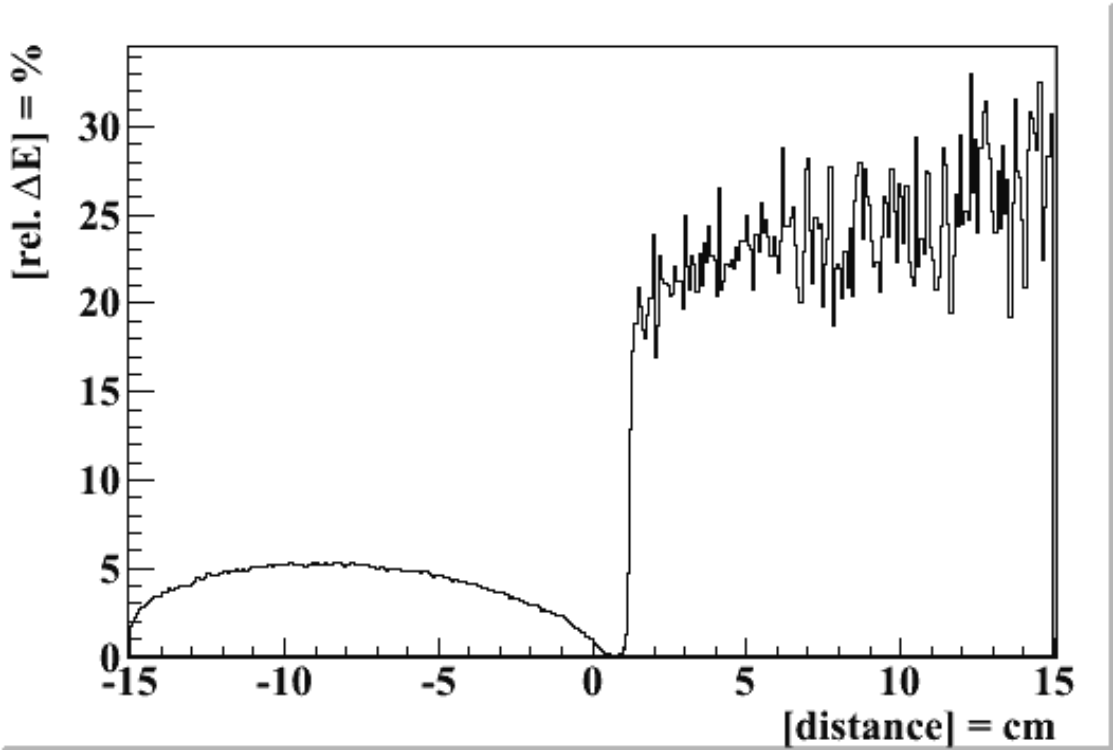

Figure A.2.: Ratio of nuclear energy deposition to absolute energy deposition from figure A.1.

Oxana Grünwald

Email: oxana.gruenwald@googlemail.com

Personal information:

Date of birth:	31st of January 1980
Place of birth:	Fabrichniy / Kazakhstan
Nationality:	German

Research experience

Sept. 2002 - Feb. 2003 Computational Imaging Sciences Group, King's College, London
Calibration of freehand 3d ultrasound using a volumetric registration approach (practical term), Supervisor: David J. Hawkes
→ Improvement of the calibration method for a 3d freehand ultrasound system composed of a conventional ultrasound machine and an optical tracking device; developed a new tissue-mimicking phantom and tested method for accuracy, repeatability and precision
→ sponsored by the InWent Organisation

Apr. 2004 - Sept. 2004 RheinAhrCampus Remagen and Medizin-Center Bonn
Development of an open source system for radiotherapy planning (diploma thesis)
→ Conception of a radiotherapy planning system as well as development of a registration algorithm for the optimisation of the matching of PET-CT-scans
→ Poster presentation at „2. Remagener Physiktage" conference
→ Paper: „Development of a Radiation Therapy Open-Source Platform" in the „Proceedings of the 2005 IEEE Engineering in Medicine and Biology 27th Annual Conference", Shanghai, 2005

Aug. 2006 - Mar. 2007 Fraunhofer Institute for Integrated Circuits (IIS), Erlangen
Geometrical calibration of rigid endoscopes (MSc thesis)
→ Further development of an existing mathematical camera model for the geometrical calibration as well as the implementation and evaluation of the new idea embedded in a state-of-the-art algorithm

Since Aug. 2007 Physics Institute IIIB, RWTH Aachen University
GEANT4 simulation and evaluation of a time-of-flight spectrometer for nuclear cross section mesaurements for use in particle therapy (PhD thesis)
→ Development of a detector simulation with the GEANT4 toolkit
→ Evaluation of simulation results
→ Development of data acquisition software for detector tests at the COler SYnchrotron COSY, Research Center Jülich
→ Participation in detector assembly and test runs at COSY
→ Co-organiser of the workshop "Nuclear Models in Hadron Therapy" 2009

Computing and programming skills

Languages and toolkits:	**C++, GEANT4, Matlab, ROOT, dcmtk, Qt**
Other:	Windows, Linux, MS Office, Open Office, LaTeX

Oxana Grünwald

Email: oxana.gruenwald@googlemail.com

Education:

Sept. 1987 - May 1993	High school nr. 18, Ust-Kamenogorsk / Kazakhstan
Dec. 1993 - Jun. 2000	High school Max-von-Laue-Gymnasium, Koblenz A-levels in mathematics, chemistry and history
Oct. 2000 - Nov. 2004	School of Applied Sciences Koblenz, RheinAhrCampus Remagen **Medical engineering and sportsmedical engineering** Elective modules: physics and technology of ultrasound, MRI, radiology since Jan. 2003: sponsored by German National Academic Foundation
Nov. 2004 - Jun. 2007	School of Applied Sciences Koblenz, RheinAhrCampus Remagen **Master of Science in Applied Physics** Main modules: theoretical physics, experimental physics, MRI, ultrasound, radiology, x-ray optics, laser physics

Practical experience in industry

Jun. 2000 - Aug. 2000 and Feb. 2001 - Mar. 2001	13 weeks internship at Corus Aluminium Walzprodukte GmbH, Koblenz practical training in the fields of metal construction, electrical, quality assurance

Extracurricular activities

2001 - 2007	Participation in common school events of the RheinAhrCampus
2002 - 2006	Tutoring in mathematics, supervision of lab exams
2005 - 2007	Mentoring inside the Ada Lovelace Project: supervision and guidance of interested school girls during practical physics experiments at the RheinAhrCampus Presentation of the project at the Physikerinnentagung 2005
Since Dec. 2005:	Member of the Ada Lovelace Project Development Association
2008 - 2010	Supervision of several physics lab experiments at the RWTH Aachen

Languages

German and Russian: fluent, English: very good (almost fluent)

Interests

Reading, dancing, theatre (2010: debut in a mutual production of amateurs and professionals „Sie und Shakespeare“, Theater 99)

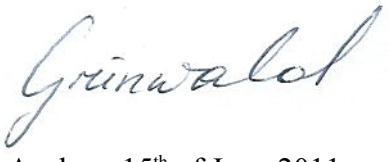

Aachen, 15th of June 2011